THE UNIVERSITY OF CHICAGO

PERIODIC BEHAVIOR OF FINITE-AMPLITUDE WAVE ACTIVITY IN THE SOUTHERN HEMISPHERE STORM TRACK

A DISSERTATION SUBMITTED TO
THE FACULTY OF THE DIVISION OF THE PHYSICAL SCIENCES
IN CANDIDACY FOR THE DEGREE OF
DOCTOR OF PHILOSOPHY

DEPARTMENT OF THE GEOPHYSICAL SCIENCES

BY

LEI WANG

CHICAGO, ILLINOIS

DECEMBER 2016

I would like to dedicate my work to my parents and my wife.

”Study nature, not books.”

- Swiss naturalist and educator Louis Agassiz

TABLE OF CONTENTS

LIST OF FIGURES

ACKNOWLEDGMENTS

Foremost, I would like to thank my thesis advisor Noboru Nakamura for patiently advising me throughout my graduate studies. It is a great privilege for me to closely follow and learn Noboru's deep thinking on fundamental problems of atmospheric dynamics.

I acknowledge my thesis committee Douglas MacAyeal, Malte Jansen, Tiffany Shaw, and Edwin Gerber for providing me with many feedbacks and constructive criticisms on my research, which was crucial leading to this thesis. I acknowledge Edwin Gerber for his time and efforts on helping me to improve my research and hosting my several visits to NYU, and for teaching me the gray radiation model. Thanks also go to Raymond Pierrehumbert, Dorian Abbot, and Fred Ciesla who served as my pre-candidacy committee.

I acknowledge Sukyoung Lee for her time spending on my education. When I was writing my prospectus three years ago, I put one figure from one of her earlier paper on my front page as the main motivation. I am very pleased that three years later I am fortunate enough to collaborate with Sukyoung and to relate our theoretical storm track framework to climate change problems. I also acknowledge Steven Feldstein for important advices on using theory to motive and to steer data analysis.

I acknowledge Malte Jansen and Ryan Abernathey for their time spending on my education. I am very fortunate to have the great opportunity to collaborate with both them for the past two years. Learning ocean dynamics has equipped me tremendously to build a big picture of atmospheric and oceanic fluid dynamics.

I acknowledge Jian Lu for the many hours spending with me discussing science over the phone and skype in our free times. Jian's enthusiasms on adopting wave activity to tackle big questions in climate dynamics have greatly shaped my thinking.

I acknowledge Isaac Held who was the first person that suggested me to adopt a two-layer quasi-geostrophic model in a meeting during the 2012 GFDL summer school. I am very happy that four years later this *E .coli* climate model has became a cornerstone of my thesis, which has equipped me with a handy tool as a solid starting point to tackle

comprehensive and challenging climate dynamics problems.

Thanks also go to Abraham Solomon for his many constructive and insightful advices for me, and to the Climate Dynamics group (you know who you are) for our invaluable weekly skype meetings to share each's expertise and to challenge each other scientifically.

I acknowledge the Univ. of Chicago English Language Institute for offering me many individual oral-languague tutoring sessions, the Univ. of Chicago Writing Program for teaching me how to build strong arguments in writing, the Graduate Writing Consultations for providing me with numerous feedbacks on my writing samples, and the Univ. of Chicago Center for Teaching for training me to be an effective instructor.

I acknowledge the Jet Propulsion Laboratory of Caltech, National Center for Atmospheric Research, and Geophysical Fluid Dynamics Laboratory for selecting me to participate their climate summer schools and giving me the opportunities to interact with their leading climate scientists and to learn how to use remote sensing and climate models.

I acknowledge my undergraduate advisor Lixin Wu for introducing me to the climate science and for encouraging me to pursue a graduate study on the atmospheric dynamics of the climate system. Thanks also go to Gang Fu for teaching me the dynamical meteorology and Qinyu Liu for teaching me the air-sea interaction. I also acknowledge Ruixin Huang for always reminding me to think about the relevance of a theory to nature.

I acknowledge my fellow students in the department who create such a stimulating environment: Andrew Malone, Daniel Koll, Feng Ding, Hailu Kong, Jonah Bloch-Johnson, Clare Huang, Nanxi Bian, Bo He, Haolan Tang, Dawei Li.

I acknowledge my family members for giving me strong supports to help me overcoming the challenging periods during my Ph.D. studies.

I acknowledge my home department for funding my graduate studies and providing many crucial resources. I acknowledge the computational resources provided by my department, by the Research Computing Center of Univ. of Chicago, and by the Yellowstone of NCAR. This research has been supported by NSF grant AGS-1151790.

ABSTRACT

This thesis concerns an intraseasonal periodic behavior of the Southern Hemisphere storm track, which is particularly conspicuous during the summer months.

It is shown that surface eddy kinetic energy (EKE) and rain rates inferred from remote sensing data exhibit remarkable periodicity around 25 days in the austral summer. This is consistent with subseasonal climate variability, *baroclinic annular mode* (BAM), a subseasonal oscillation in the storm track activity, discovered recently in the meteorological reanalysis products. With the assumption that the interaction between eddies and the mean flow plays an important role in this periodic behavior, the thesis begins by developing a new theoretical framework of the eddy - mean flow interaction. It consists of three coupled equations for the interior and surface finite-amplitude wave activity (FAWA) and the barotropic zonal-mean zonal flow. The theory provides an accurate latitude-by-latitude description of atmospheric angular momentum - wave activity budget that captures the storm track dynamics.

In the mid-latitude austral summer, the wave activity budget reveals a largely adiabatic, antiphase covariation of FAWA and the mean flow. A marked periodicity is found for FAWA around 20-30 days, but not for the mean flow. The former is primarily driven by the low-level meridional eddy heat flux, which also exhibits a sharp spectral peak around 25 days, whereas the latter is primarily driven by the meridional eddy momentum flux. The difference in the spectra of FAWA and the mean flow arises from (i) distinct spectra of low-level meridional eddy heat flux and the barotropic eddy momentum flux convergence and (ii) a strong thermal damping of surface wave activity.

The thesis demonstrates that the 25-day periodicity in FAWA and the eddy heat flux is particularly robust during the warm season. It is shown that the essence of the periodicity is reproduced in a hierarchy of numerical models, including the state-of-the-art climate models, and that the results are largely insensitive to the representation of the oceans. A dry GCM reproduces qualitatively BAM-like eddy heat flux spectra if the zonal-mean

state resembles that of the austral summer and if the surface thermal damping is sufficiently strong. The two-layer quasi-geostrophic model captures the gist of oscillation when baroclinicity is weak and the bottom layer is chosen sufficiently thinner than the top layer.

The observed eddy heat flux cospectra in summer contain a few dominant frequencies for each of the energy-containing zonal wavenumbers (4-6). As these modes travel at different phase speeds they interfere with each other and produce an amplitude modulation to the eddy heat flux with a periodicity consistent with the BAM. The meridionally confined baroclinic zone in the mean state of the austral summer provides a waveguide that directs the mode propagation and interference along the latitude circle. Somewhat surprisingly, the emerging picture champions the linear wave dynamics as a driving mechanism of the 25-day periodicity. This stands in a stark contrast to the prevailing interpretation of the BAM based on the nonlinear oscillator model, in which the feedback between the eddy heat flux and background baroclinicity is deemed essential for the observed periodicity. This thesis demonstrates that such feedback is not corroborated by data for the austral storm track.

CHAPTER 1

MOTIVATION

Generations of scientists have been fascinated by the large-scale weather systems in the mid-latitudes where most of the world population resides. The mid-latitude atmosphere exhibits endlessly changing weather patterns touching our lives. A better understanding of the weather systems' variability will lead to a better weather and climate predictions. By developing a relevant and suitable theoretical framework, this thesis conducts a comprehensive investigation of the periodic behavior in the circulation patterns of the Southern Hemisphere (SH) mid-latitude troposphere. Periodic behaviors refer to repeating patterns of the circulation on a certain timescale and this thesis considers those associated with internal dynamics, e.g. not directly driven by diurnal or seasonal cycle.

In the climate dynamics of the Earth system, the most well-known periodic behaviors are found in the tropics: the El Niño - Southern Oscillation drives the atmosphere and oceans with a rhythm of three to seven years; the Madden-Julian Oscillation sends a large-scale convective system eastward every month or two, and the Quasi-Biennial Oscillation switches stratospheric winds around the Earth's equator back and forth between westerlies and easterlies roughly every 28 months. These periodic behaviors are valuable pacemakers for deepening our mechanistic understanding of the climate system and for improving our ability to simulate and forecast climate. One of the reasons that major oscillations are visible in the tropics is that the background state is nearly steady and large-scale geostrophic turbulence is relatively weak with the vanishing Coriolis parameter (when compared to that in the mid-latitudes).

Is there any robust periodic behavior in the mid-latitudes? The main feature of the mid-latitude flow pattern is a meandering jet stream [1], which dominates the variability on synoptic timescales and affects the weather pattern significantly. The variability of the

1. An atmospheric flow can be characterized by a zonal velocity u and a meridional velocity v, and the strength of jet stream is quantified by the zonal-mean of the zonal velocity, denoted by $\overline{u}$. Throughout the thesis, overbar and prime denote zonal mean and deviation from it, respectively.

jet stream has been a central theme of dynamic meteorology. Indeed, meteorologists have long speculated that a periodic behavior may exist in the mid-latitude atmosphere [e.g. *Rossby*, 1939; *Namias*, 1950] [2]. A detailed historical review will be provided in Section 1.2.

This thesis investigates the dynamics of the periodicity in the Southern Hemisphere storm track. The motivation primarily comes from a periodic behavior at intra-seasonal timescales recently highlighted by David Thompson and collaborators. This periodic behavior has a signature period of around 25 days and is called the *baroclinic annular mode* or BAM [*Thompson and Woodworth*, 2014; *Thompson and Barnes*, 2014; *Thompson and Li*, 2015; *Li and Thompson*, 2016].

The works of Thompson and the collaborators concern the variability of a quadratic eddy quantity - eddy kinetic energy (EKE) [3]. Specifically, the variability of the zonal-mean EKE is extracted as the leading mode of the empirical orthogonal function (EOF). The principal component associated with the leading mode displays a robust periodicity of 25 days. It has been shown through regression analysis that precipitation and the eddy heat flux all correlate well with the leading mode of the zonal-mean EKE. Given that the large-scale periodic behavior has been confirmed in Thompson's results, a thorough dynamical understanding of its mechanism is a logical next step. Since the long period in the oscillation has a potential to improve the predictability of weather, this is potentially beneficial to our society, as most of the population lives in the mid-latitudes.

In Section 1.1, I will first investigate the remote sensing from space to illustrate a robust 25-day periodicity in surface winds and precipitation in the Southern Hemisphere summer as a manifestation of the BAM. In Section 1.2, I will summarize the historical

2. About 500 years ago, the intra-seasonal repeating weather patterns in the SH storm track were identified by Vasco da Gama who made the historical exploration to reach India by sea. When his team was close to the Cape of Good Hope, Da Gama documented that *"For twenty-seven days (from March 20 to April 16) we had the wind astern ... But the wind fell and we were becalmed."* [Da Gama's journals in *Ravenstein*, 2010]

3. Eddy kinetic energy (EKE$\equiv (u'^2 + v'^2)/2$) serves the purpose of quantifying the overall strength of eddying motion, where perturbations in both zonal and meridional direction are $u' \equiv u - \overline{u}$ and $v' \equiv v - \overline{v}$.

search for the periodicity in the literature. This will help place the present investigation in a historical perspective and introduce some key ideas. In Section 1.3, I will discuss a contemporary idea - the nonlinear oscillator theory - as a mechanism that has been proposed for the observed periodic behavior. While appreciating its strength as a simple conceptual model, I will point out its inconsistency with observations as well as limitations in its theoretical considerations. In Section 1.4, I will lay out a roadmap of this thesis to quantify and to understand the observed periodic behavior.

The bulk of the dissertation arises from the (to-be) published work [4] in which I was the lead-author. The theoretical framework and analysis of the austral summer comes from *Wang and Nakamura* [2015] (©American Meteorological Society. Used with permission.); The comparison between seasons and idealized simulations comes from *Wang and Nakamura* [2016] (©American Meteorological Society. Used with permission.). The majority of the rest of the thesis, such as the satellite data analysis (Section 1.1), a diagnostic low-order wave-mean flow interaction model and finite-amplitude wave activity modes (Appendix 3.B), the climate model analysis (Section 4.1), the two-layer quasi-geostrophic model results (Section 4.3), the non-normal mode results (Section 5.4) are in preparation for journal publication(s).

4. In addition to the directly related work, the general setup of the two-layer quasigeostrophic model is similar to that in *Nakamura and Wang* [2013]; *Wang and Lee* [2016] (©American Meteorological Society. Used with permission.), and the thesis's key tool – spatial-temporal spectrum analysis – is similar to that in *Wang et al.* [2016].

1.1 A periodic wind and rain rate in remote sensing

We start the discussion from a brief look at observational data that suggest the 20 - 30 day oscillation in the austral summer. Quite so often, reanalysis products are used to investigate nature as I will do in Section 1.3 and Chapter 3; however the interpretation of the reanalysis products requires caution as they are essentially state-of-the-art general circulation model (GCM) outputs that have been assimilated with available observations. As such, I shall introduce the theme of this dissertation with a less filtered observation of nature - satellite remote sensing. This provides an independent evidence for the 20 - 30 day oscillation (apart from the reanalysis products) to firmly motivate this thesis.

In this section, I focus on surface quantities, i.e., rain rate and surface winds, as these are straightforward observations and yet reflect the physical processes in the interior of the atmosphere. With the ability to penetrate through the atmospheric column, microwave radiometers measure precipitation and surface winds with adequate accuracy; especially they are capable of providing almost continuous all-weather observations. Figure 1.1 describes the general climatology of two representative months, January and July.

In both seasons, the Southern Hemisphere storm track (roughly ranging from 35 S to 65 S as indicated by the blue boxes) is characterized by a band of rainfall and strong winds that extends longitudinally over most of the Southern Ocean, whereas in the Northern Hemisphere the storm tracks are only vigorous over the two ocean basins, particularly near the western boundary currents, i.e. the Kuroshio Current and the Gulf Stream. The relatively zonally symmetric storm track in the Southern Hemisphere opens the possibility that winds, after blowing over the entire global circle, are able to re-enter the domain [5].

During the austral summer (January), the storm track is characterized by a more con-

5. In a stark contrast to the zonally symmetric storm tracks in the Southern Hemisphere, major topographic features in the Northern Hemisphere such as the Himalayas and the Rockies significantly detour atmospheric flows, leading to highly localized storm tracks.

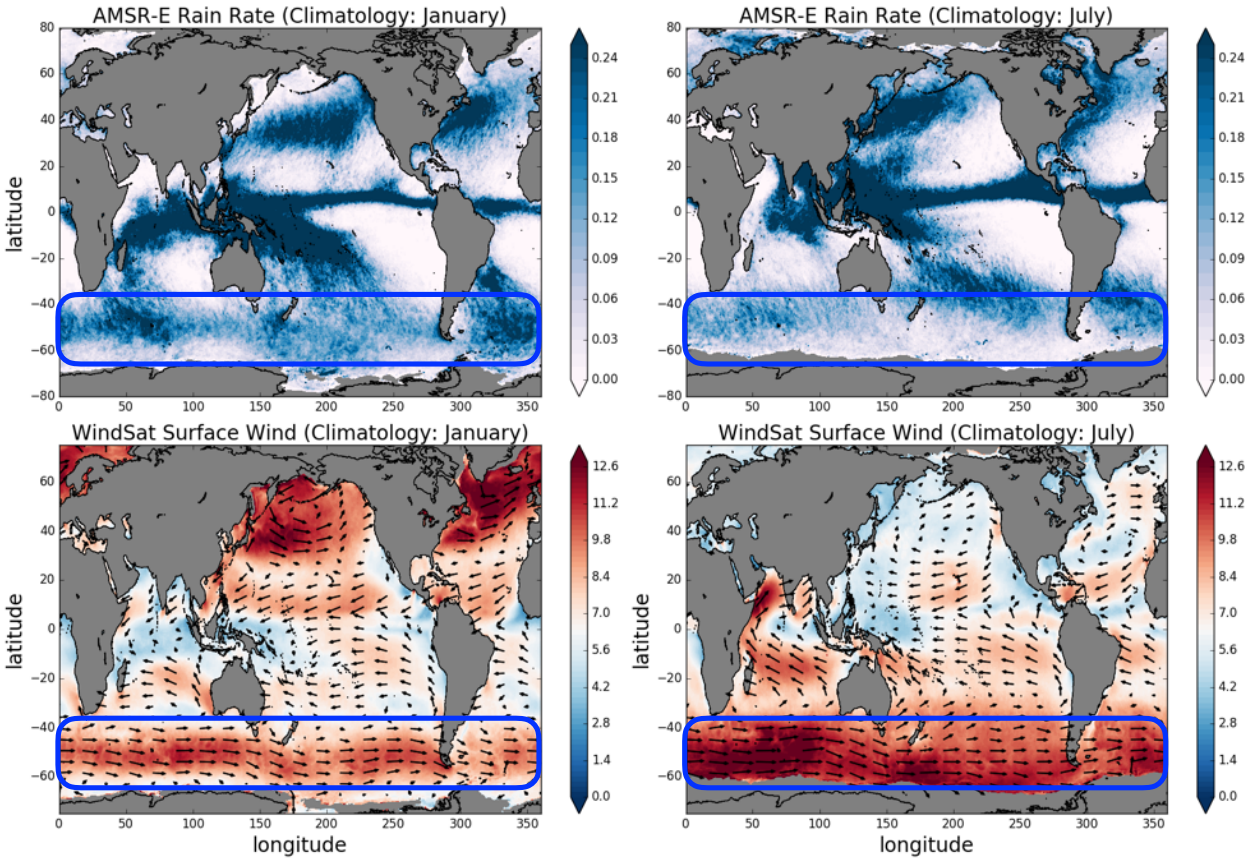

Figure 1.1: (Top row) Remote sensing of rain rate for a 9-year (2002-2011) average of January (left) and July (right). Data are obtained from the Advanced Microwave Scanning Radiometer (AMSR) - E [*Wentz et al.*, 2014], a passive microwave radiometers installed on the polar-orbiting satellite *AQUA*. (Bottom row) Remote sensing of near surface wind for a 12-year (2003-2015) average of January (left) and July (right). Data are obtained from WindSat Polarimetric Radiometer [*Wentz et al.*, 2013], a passive microwave radiometer installed on the polar-orbiting satellite *Coriolis*. Shading and vector length both represent wind amplitude, and the vectors denote wind directions. In all panels, the blue box indicates the approximate location of the Southern Hemisphere storm track.

centrated rain rates and more zonally symmetric surface winds. In contrast, during the austral winter (July), although surface winds are strong over the South Indian Ocean, less rain occurs there, presumbly because the cold ocean surface temperatures do not allow much moisture to remain in the atmosphere. Since precipitation reflects the state of water vapor within the atmosphere, this implies that the static stability within the austral summer storm track within 40 S - 60 S is distinct from the dry static stability.

Let us further examine a particular period of austral summer (December 2011 - February 2012) [6]. In Figure 1.2, the zonal-mean surface zonal winds calculated from the WindSat data (upper panel) wobble on a synoptic timescale, i.e. $\sim$ a week, and shift between north and south [7]. Focusing on the transient perturbations, surface eddy kinetic energy undergoes a very pronounced repeating pattern (middle panel). Indeed, roughly four to five surface EKE peaks can be identified within this 90-day period, hinting that a periodic behavior might exist with a timescale of 20-25 days. The surface zonal-mean EKE correlates well with the zonal-mean rain rate (bottom panel), in the sense that heavy zonal-mean rain rates consistently occur at the peaks of surface EKE.

We take a close look at the two selected snapshots, indicated by the blue vertical lines in Figure 1.2. December 15, 2011 (first vertical line) is characterized by low zonal-mean zonal winds and high EKE and rain rate, while January 16, 2012 (second vertical line) is characterized by high zonal-mean zonal winds and low EKE and rain rate. I therefore refer to the first as 'low index state' and the second as 'high index state'. Figure 1.3 shows the horizontal distribution of rain rates and surface winds for the two states. The surface winds in the low index state have a strong wavy component, whereas the surface winds in the high index state are more zonally symmetric. Similarly, the rain rate in the low index state is organized locally (e.g. around 30, 180, 280 degrees in longitude), whereas the rain rate in the high index state is more spread zonally and overall weaker.

6. The choice of this period is consistent with that in *Wang and Nakamura* [2015]. The key findings hold for all available years.

7. This is a signature of the annular mode [*Thompson and Wallace*, 2000] to be explained in Section 1.3.

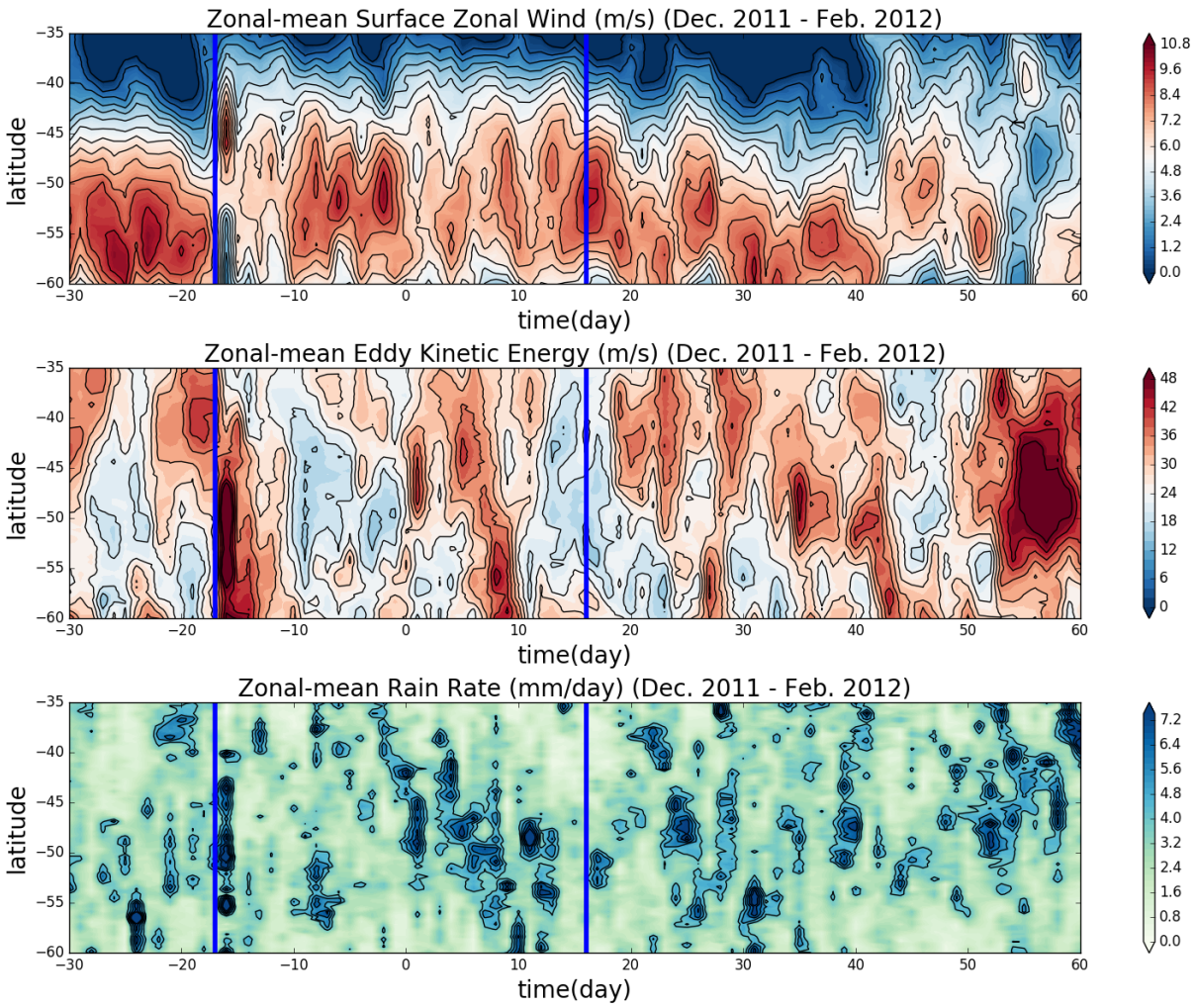

Figure 1.2: Hovmöller diagram for a selected austral summer period (December 2011 - February 2012). The days in the abscissa are relative to January 1, 2012. (Upper) Zonal-mean surface zonal wind. (Middle) Zonal-mean surface eddy kinetic energy (EKE). (Lower) Zonal-mean rain rate. Blue vertical straight lines denote two specific dates (December 15, 2011 and January 16, 2012), whose latitude-longitude snapshots will be presented in Figure 1.3. All data are obtained from WindSat radiometer [*Wentz et al.*, 2013].

Do the above findings illustrate a ubiquitous variability of the large-scale circulation, or are they simply a coincidence for this particular year? To gain confidence on this important issue, I conducted a power spectrum analysis for all available years. Since each satellite only covers a short period of time, I choose the Cross-Calibrated Multi-Platform [*Atlas et al.*, 2010] gridded surface vector winds to conduct multi-year analysis, which combines all available satellite observations via variational analysis method [8]. After removing seasonal cycles, defined as the first four Fourier modes as per *Lorenz and Hartmann* [2001], I calculated power spectrum of a 120-day chunk for each year. Austral summer is defined as December - March and austral winter is defined as June - September. The final results are presented as the multi-year average.

In Figure 1.4, the zonal-mean zonal surface wind has almost no periodicity in either season. It is characterized by red-noise spectra, concentrated near 40 S and 60 S (top panels). In a stark contrast, the zonal-mean surface EKE in summer has a strong periodicity near 0.04 CPD (cycles per day, 25 days in period), between 35 S - 55 S, whereas in winter, it is best summarized as a red noise spectra punctuated with pronounced peaks at 0.02 and 0.06 CPD. The summer rain rates also suggest a robust peak near 25 days, but they are spread over a wide range of latitudes. The winter rain rates are substantially weaker than those in summer, mostly confined to the equatorward of 40 S.

The multi-year analysis suggests that the periodicity of surface precipitation and EKE found in the earlier single-year analysis exists in any given year. However, the surface data only provide circumstantial evidence of what involves the entire atmosphere. Unpacking the mechanism of the observed periodicity calls for a thorough examination of the interior atmosphere, which itself requires an appropriate theoretical framework. This

8. The Cross-Calibrated Multi-Platform gridded data are produced with all available satellite remote sensing (1980-2015), such as radiometer wind speeds, QuikSCAT and ASCAT scatterometer wind vectors, moored buoy wind data. Using a variational analysis method, ERA-Interim model wind fields provide initial guesses. When reliable remote sensing exists, final results are determined by the available observations, although occasionally all instruments fail in which case the results do rely on the ERA-Interim's initial guess. However, the majority of the time period (1980-2015) are covered by one or more remote sensing. I therefore use this data to perform multi-year analysis.

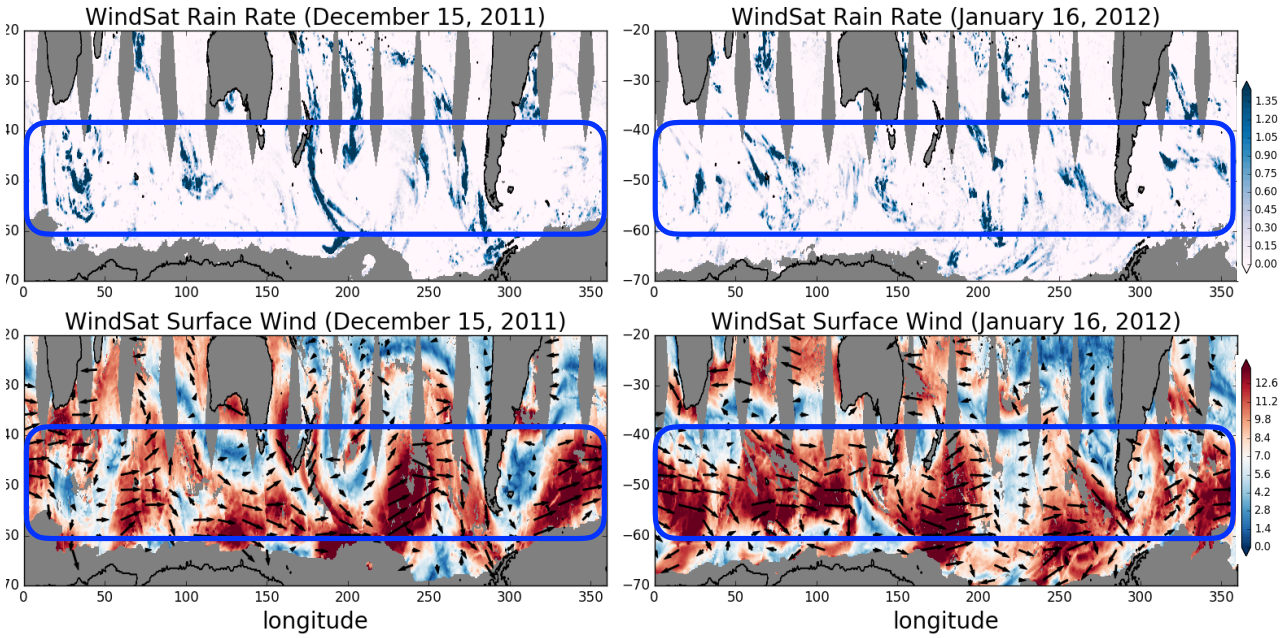

Figure 1.3: Snapshots of December 15, 2011 (left column) and January 16, 2012 (right column). (Top) Rain rate obtained from WindSat. (Bottom) Surface wind amplitude (shading, vector length) and directions (vector) obtained from WindSat. In all panels, the blue box denotes the Southern Hemisphere storm track, and all snapshots are averaged from its daily ascending and descending passes.

motivates the following chapters to address the main question of the thesis: how the observed periodicity in the austral summer storm track activity arises.

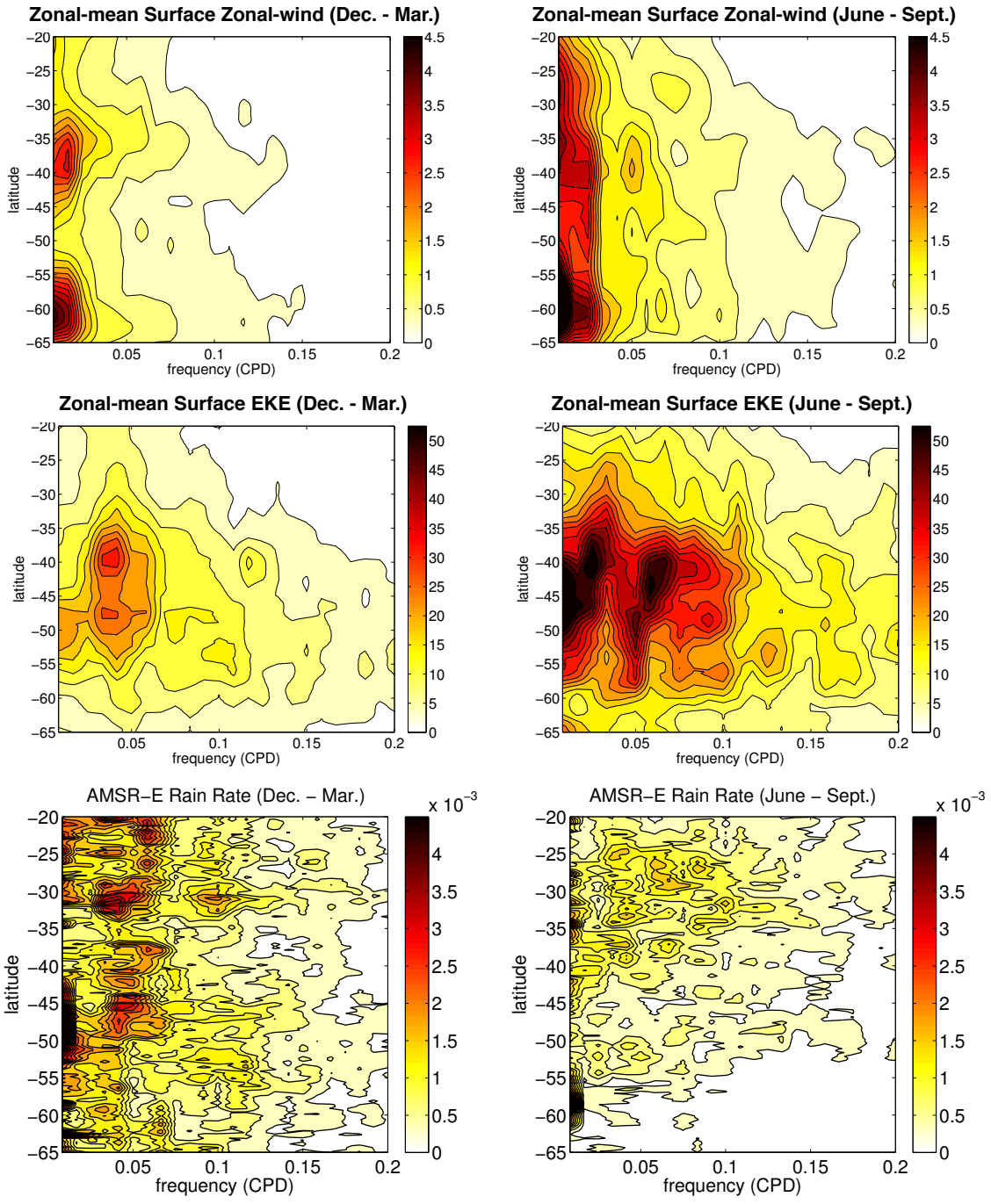

Figure 1.4: Power spectra for the austral summer (left column) and austral winter (right column). (Top) Surface zonal-mean zonal wind weighted by $\cos\phi$, where ϕ is latitude. (Middle) Surface zonal-mean eddy kinetic energy weighted by $\cos\phi$. (Bottom) Rain rate. The surface wind data is obtained from Cross-Calibrated Multi-Platform [*Atlas et al.*, 2010] gridded surface vector winds. The rain rate data is obtained from AMSR-E [*Wentz et al.*, 2014].

1.2 The historical search for periodicity in the mid-latitude weather pattern

Generations of meteorologists have speculated that periodic behavior may exist in the mid-latitude atmosphere, which was in fact the central motive for developing many fundamental concepts in dynamic meteorology [e.g. *Rossby*, 1939; *Namias*, 1950]. Prior to the modern numerical weather prediction, weather forecast relied largely on the analysis of weather charts and personal experiences. A periodicity on intra-seasonal timescale would be of great help to the forecasters by providing a handy first principle.

The mid-latitude circulation of the troposphere is dominated by a meandering jet stream and its behavior affects the weather pattern. *Rossby* [1939] finds that the intensity of zonal circulation fluctuates on a fairly regular fashion, hence he developed a metric *zonal index*: a measure of the surface pressure difference between latitudes 35N and 55N. *Namias* [1950] further connects this zonal index with changing weather patterns - for example, atmospheric blocking events always occur at a low zonal index.

Motivated by these observational discoveries, *Hide* [1953] and *Fultz et al.* [1959] use a rotating tank to simulate the behavior of the atmosphere in the laboratory. The underlying motive for these laboratory experiments is that the atmosphere can be viewed as a special configuration of a differentially heated rotating fluid. Vacillation of the westerly flow was indeed found in these rotating experiments, which led to the development of a series of theories [e.g. *Lorenz*, 1963a; *Pedlosky*, 1970; *Lindzen et al.*, 1982].

A first mechanistic and numerical study of the vacillation in the westerly flow is documented in *Lorenz* [1963a]. A highly truncated two-layer quasi-geostrophic model [9] is adopted to investigate the parameter space of the flow regimes. Although the highly truncated nature of the governing equations casts reasonable doubt on the validity of the theory, *Lorenz* [1963a] shows that, for this nonlinear system, the flow regime can at

9. The two-layer quasi-geostrophic model will be described in detail in Chapter 4

least be categorized into a few types: steady waves, regular periodic vacillations, irregular nonperiodic vacillations. The results of *Lorenz* [1963a] are significant because, in light of the seminal work of *Charney* [1947], *Eady* [1949], and *Phillips* [1951] [10], it is well known that under Earth-like parameters westerly flow is unstable to small perturbations, hence chaotic behavior is expected in the nonlinear regime. Surprisingly, under certain flow configurations, *Lorenz* [1963a] finds that a nonlinear rotating fluid *can* exhibit a regular periodic behavior. In fact, the motive to search for periodicity in *Lorenz* [1963a] came with a significant concurrent work [*Lorenz*, 1963b] [11], in which it was found that the atmosphere contains an intrinsic nonperiodic behavior (now known as chaos). Periodicity and chaos are two sides of the same coin: periodicity may in principle be embedded in a seemingly chaotic atmospheric flow. *Pedlosky* [1970, 1971, 1982] shows that the periodic behavior can arise from the weakly nonlinear interaction between the mean flow and the baroclinically unstable eddies.

However, at the time of Hide, Fultz, and Lorenz, no adequate observational evidence was available to support the speculations based on the zonal index fluctuations [*Rossby*, 1939; *Namias*, 1950] that a robust periodic behavior truly exists in the jet stream. *Lorenz* [1963a] made an opening remark as "*If hidden periodicities really do exist (in nature), they are very well hidden*". As I will discuss in this thesis, we have made some advances in unearthing these "*hidden*" periodicities.

A first observational evidence of periodic behavior in the mid-latitude circulation was presented by *Webster and Keller* [1974, 1975] who found from a one-year limited balloon data that the eddy kinetic energy in the Southern Hemisphere storm track had a periodicity of three weeks. Unfortunately, the available data was sparse prior to the satellite era, therefore the conclusion based on one-year balloon data could not be generalized to a ubiquitous behavior of the general circulation.

10. See Chapter 2.1.2 for detailed references and discussions on baroclinic instability.

11. This contribution opened the field of nonlinear dynamics.

The systematic and continuous satellite remote sensing opened the modern era of atmospheric dynamics and gave new hope to find the periodic behavior. Using FGGE III-b analysis [12], *Chen et al.* [1987] identified a possible quasi-periodic variation of several energy variables [13] and highlighted its existence in the summertime Southern Hemisphere.

With the advent of the modern global gridded reanalysis datasets, the spatio-temporal variabilities of the zonal-mean zonal flow has been studied intensively. In the mid-latitudes, the most notable feature in the zonal-mean zonal flow is eddy-driven jets. Unlike the subtropical jets that are driven by angular momentum transported from the tropics through the Hadley cell, the climatological surface westerlies in the extratropics are driven by the meridional convergence of westerly momentum flux associated with baroclinic eddies [*Held*, 1975]. Eddy-driven jets display strong variability because the weather systems interact with and alter the mean state. The principal pattern of the extratropical atmosphere's variation is the *annular modes*: meridional excursions of surface westerlies and jets on the synoptic and longer timescales. They were discovered in the late 1990s [*Thompson and Wallace*, 2000; *Baldwin et al.*, 2003]. The annular modes are the leading patterns of variability that persist year-round in the extratropics of each hemisphere. They are characterized by a meridional seesawing of atmospheric mass and angular momentum between high-latitude and mid-latitude regions separated by a node around 45° North/South [*Thompson and Wallace*, 2000]. These north-south fluctuations are robust at almost all longitudes in the Southern Hemisphere, whereas mainly over the North Atlantic sectors in the Northern Hemisphere [*Limpasuvan and Hartmann*, 2000]. While the north-south motions themselves are not rigorously annular, the statistics are sufficiently annular for this leading EOF mode to dominate the total variance [*Gerber and Thompson*, 2016]. The annular modes have become a synonym of the aforementioend zonal indices. Annular modes entail changes in the mean flow and the eddies and their inter-

12. The FGGE is a acronym of First GARP (Global Atmospheric Research Program) Global Experiment, which used the data assimilation scheme of the European Center for Medium Range Weather Forecasts.

13. Available potential energy and kinetic energy of the zonal-mean state and eddy.

action. Specifically, in the high-index phase (jet being displaced poleward), baroclinic eddies shift from mid-latitude to high-latitude simultaneously with the eddy-driven jets, as shown clearly by the Eliassen-Palm (E-P) flux analysis [14] [*Lorenz and Hartmann*, 2001].

The most widely adopted method to quantify the annular modes is the empirical orthogonal functions (EOF) analysis. From eigenanalysis of covariance matrix, EOFs provide the principal components of variation together with variance explained. Various meteorological fields such as geopotential height (representing mass shifts) and zonal wind (representing mid-latitude jet displacements) may be used as the basis of EOF analysis. The first EOF in each hemisphere represents variability associated with north-south oscillation of the mid-latitude jet. The structure of these modes tilts very little with altitude, suggesting that the annular modes are vertically coherent, extending from the surface to the lower stratosphere [*Thompson and Wallace*, 2000; *Limpasuvan and Hartmann*, 2000; *Lorenz and Hartmann*, 2001].

However, annular modes do not possess any single robust period [*Feldstein*, 2000; *Gerber et al.*, 2008]. Instead, it is characterized by a red-noise process with an e-folding timescale of 10 days.

More recently, *Thompson and Woodworth* [2014] and *Thompson and Barnes* [2014] identified a robust oscillation in eddy kinetic energy in the Southern Hemisphere extratropics with a period of 25-30 days. The oscillation is largely associated with the variability in the low-level meridional eddy heat flux and baroclinicity of the flow, rather than the eddy momentum flux, and for this reason it is distinct from the annular modes and termed *baroclinic annular mode* or BAM. It appears that this phenomenon is consistent with the similar variability recognized earlier by *Webster and Keller* [1974, 1975] with limited balloon data and by *Chen et al.* [1987] using FGGE III-b analysis.

The recent developments surrounding the BAM highlight that the amplitude of the eddies in the Southern Hemisphere storm track exhibits a robust 25 - 30 day oscillation,

14. The E-P flux analysis will be explained in Chapter 2.1.

but its precise mechanism is yet to be understood. This opens a new theme of periodic behavior in the mid-latitudes, which I intend to explore in this thesis.

1.3 A contemporary view: nonlinear oscillator as a mechanism of periodicity

Given the observational evidence provided by Thompson and the collaborators on the BAM, one of the first questions to be asked is this: How is it that large-scale eddy prefers a periodic behavior to a more chaotic one, particularly during the austral summer? [15] *Thompson and Barnes* [2014] (hereafter TB14) invoke a nonlinear oscillator model of the BAM based on the feedback between the baroclinicity of the flow and the meridional eddy heat flux. The periodic behavior of this model is reminiscent of the limit cycle in the amplitude of weakly nonlinear baroclinic waves with weak dissipation [*Pedlosky*, 1970, 1971]. The timescale of oscillation in their model depends on the (empirically determined) strength of feedback and the relaxation timescale of baroclinicity. *Ambaum and Novak* [2014] (hereafter AN14) propose, in a different context, a similar nonlinear oscillator model for storm track variability that incorporates both growth and damping of eddies as well as restoration of baroclinicity (Eady growth rate). In their model the timescale of oscillation is determined by the specified restoration rate for baroclinicity. In the context of the BAM, periodicity in the nonlinear oscillator models should be interpreted as a growth-decay cycle of baroclinic wave packet, rather than an individual eddy lifecycle that has much shorter timescales [e.g. *Lee and Held*, 1993]. The meridional eddy heat flux and growth rate characterize the average properties of eddies within the packet, influencing each other through a feedback process.

15. An earlier version of this material appeared in *Wang and Nakamura* [2016]. ©American Meteorological Society. Used with permission.

In TB14, the simple nonlinear oscillator model is constructed as:

$$\frac{\partial}{\partial t}\left\langle \overline{v'T'} \right\rangle = -\alpha \left\langle \frac{\partial \overline{T}}{\partial y} \right\rangle + \epsilon(t), \tag{1.1}$$

$$\frac{\partial}{\partial t}\left\langle \frac{\partial \overline{T}}{\partial y} \right\rangle = \beta \left\langle \overline{v'T'} \right\rangle - \left\langle \frac{\partial \overline{T}}{\partial y} \right\rangle / \tau, \tag{1.2}$$

where t and y are time and latitude; the angle bracket denotes the average over latitudes; α and β are coefficients to be determined through regression analysis; $\overline{v'T'}$ and $\frac{\partial \overline{T}}{\partial y}$ denote the anomalies of the zonal-mean meridional eddy flux of heat and the zonal-mean meridional temperature gradient; τ is a linear damping time for baroclinicity, and $\epsilon(t)$ reflects stochastic forcing of the heat flux by white noise.

The model in AN14 is similarly constructed:

$$\frac{\partial}{\partial t}\left\langle \overline{v'T'} \right\rangle = 2\left(-k\left\langle \frac{\partial \overline{T}}{\partial y} \right\rangle - s_0 \right)\left\langle \overline{v'T'} \right\rangle, \tag{1.3}$$

$$\frac{\partial}{\partial t}\left\langle \frac{\partial \overline{T}}{\partial y} \right\rangle = l^2 \left\langle \overline{v'T'} \right\rangle - \frac{F}{k}, \tag{1.4}$$

where l is meridional wavenumber, F denote diabatic heating, k is a parameter to be determined, and s_0 is an eddy dissipation rate. Note that all F, k, and s_o are constants that need to be determined externally.

Comparing the two models, several differences arise: while the TB14 model is driven by stochastic forcing $\epsilon(t)$, the AN14 model is driven by diabatic heating F which is constant in time; while the TB14 model considers linear feedback between the eddy heat flux and the meridional temperature gradient, the AN14 model involves a nonlinear relation. Moreover, AN14 retain the explicit dependence on meridional wavenumber to be more consistent with the zonally averaged thermodynamic equation, although in practice this parameter is also a constant and externally prescribed.

Despite the differences, since both models are nonlinear oscillators by construction, a periodic behavior appears in certain parameter ranges as a result of feedback between the

eddy heat flux and the meridional temperature gradient. The nonlinear oscillator model represents a zero-dimensional eddy flux closure that predicts amplitude vacillation, but observational evidence suggests that it might not be an adequate model for the BAM. To demonstrate why, I start from the zonal-mean temperature gradient equation:

$$\begin{aligned}\frac{\partial}{\partial t}\left\langle\frac{\partial\overline{T}}{\partial y}\right\rangle &= -\frac{\partial^2}{\partial y^2}\left\langle\overline{v'T'}\right\rangle + \frac{\partial^2}{\partial y^2}\left\langle\overline{v}\,\overline{T}\right\rangle + \frac{\partial}{\partial y}(F+D)\\ &= -\frac{\partial^2}{\partial y^2}\left\langle\overline{v'T'}\right\rangle + \text{residual},\end{aligned} \tag{1.5}$$

The first term on the right-hand side represents large-scale eddy forcing, the second term represents the arrangement by the mean meridional circulation, F is diabatic heating and D is thermal damping. Since the eddy forcing is the primary driver of the zonal-mean temperature gradient in the mid-latitudes, the last three terms are lumped together as a residual term. Note that equation (1.4) (the AN14 model) is analogous to this equation, the meridional wavenumber replacing the meridional derivative. Since the angle bracket represents meridional integral over the latitude band in which the BAM is observed, equation (1.5) may be rewritten as:

$$\frac{\partial}{\partial t}(\overline{T}(y_1)-\overline{T}(y_2)) = -\frac{\partial}{\partial y}\left(\overline{v'T'}(y_1)-\overline{v'T'}(y_2)\right) + \text{residual}, \tag{1.6}$$

where y_1 and y_2 are the bounding latitudes of the BAM.

First, I used the European Centre for Medium-range Weather Forecasts (ECMWF) ERA-Interim reanalysis [*Dee et al.*, 2011] and computed the difference in the 850 hPa zonal-mean potential temperature between 40.5 S ($= y_1$) and 55.5 S ($= y_2$) as a bulk measure of the low-level baroclinicity of the mean state in the mid-latitude. Figure 1.5a shows the power spectrum of this quantity for summer (December-March). The spectrum is red and it shows little evidence of a spectral peak around the BAM frequencies (~ 0.04 CPD).

I have also evaluated the tendency and the meridional eddy flux terms in equation

(1.6) from the 6 hourly reanalysis product and saved the data daily. Figure 1.5b shows the spectra for these terms. The tendency (black) and eddy forcing (red) have comparable spectral intensity. Their difference associated with the residual term in (1.6) is mainly due to (unresolved) turbulent heat flux in the vertical (c.f. *Herman* [2015]), which acts as a damper for the temperature variability particularly at low frequencies. This turbulent heat flux is especially strong over the ocean surfaces. Here both spectra have a peak around 0.17 - 0.2 CPD (5-7 days), consistent with synoptic weather systems but not with the BAM. It is notable that despite the clear spectral peak in the eddy heat flux around 0.04 CPD (TB14), its meridional derivative (the red curve in Figure 1.5b) does not show a comparable spectral peak. This suggests that the direct influence of the eddy heat flux on baroclinicity is not particularly strong at the BAM frequency. The corresponding spectra for winter (June-September) are shown in Figures 1.5c and 1.5d. The overall power of baroclinicity is weaker in winter (Figures 1.5a and 1.5c). This is due partly to weaker meridional temperature gradients (see Figure 3.11a below) and partly to a stronger thermal damping from the ocean surface (the difference between the two curves in Figure 1.5d). Again the baroclinicity spectrum is largely red (Figure 1.5c) and the tendency and the eddy forcing terms have broad spectra with no distinctive peak at the BAM frequency.

If equations (1.1)-(1.2) or (1.3)-(1.4) describe the frequency selection mechanism, at least one expects both the eddy heat flux and the zonal-mean baroclinicity to exhibit similar spectral peaks. The apparent lack of a pronounced spectral coupling between baroclinicity and the eddy heat flux casts doubt on the validity of the nonlinear oscillator models, which assume feedback between them. (I have also used the tropospheric mean vertical shear of the zonal-mean zonal wind as a surrogate for baroclinicity assuming thermal-wind balance, and the result was essentially similar.)

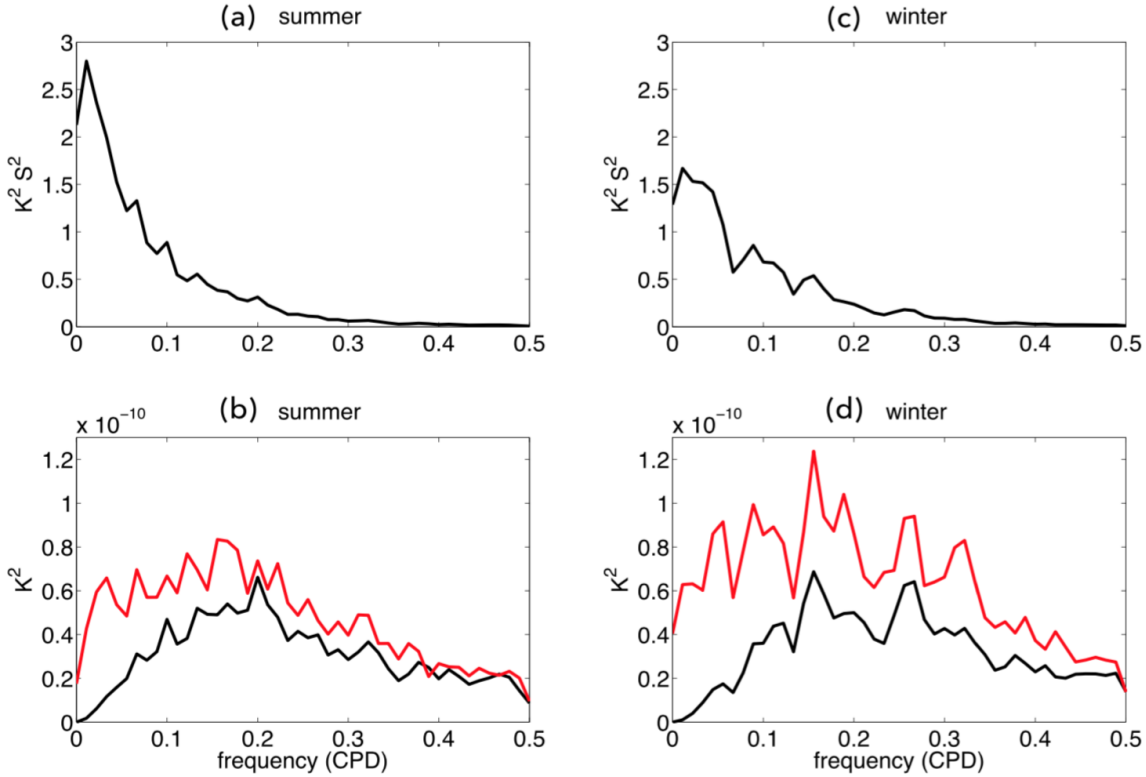

Figure 1.5: Spectral densities of baroclinicity properties at 850 hPa for the Southern Hemisphere summer (December-March). (a) $\bar{\theta}(55.5°\,\mathrm{S}) - \bar{\theta}(40.5°\,\mathrm{S})$. (b) Same as (a) but for the tendency of $\bar{\theta}(55.5°\,\mathrm{S}) - \bar{\theta}(40.5°\,\mathrm{S})$. (c) Same as (b) but for the difference in $(a\cos\phi)^{-1}\partial(\cos\phi\overline{v'\theta'})/\partial\phi$. between 55.5°S and 40.5°S, where a is the Earth's radius and ϕ is latitude. Based on the 1979-2014 ERA-Interim reanalysis. (appeared in *Wang and Nakamura* [2016]. ©American Meteorological Society. Used with permission.)

1.4 The problem at hand

The motives for finding periodic behaviors in the mid-latitude circulation have profoundly impacted the field of atmospheric dynamics, and in a sense, even gave birth to the field itself. With the help from satellite observation and large computational power, we are in a golden age to seek a more certain and satisfactory answer.

Observational evidences alone do not guarantee physical understanding. Part of the key challenge is to evaluate the role of eddy in producing the observed 20 - 30 day oscillation in EKE and surface heat flux. It is no small task because the observed eddy field is a mixture of waves and turbulence - geostrophic turbulence. Waves are small-amplitude eddy, for which the governing equations may be linearized and certain dispersion relations may be derived. Whereas turbulence has energy comparable to that of the mean flow and lacks a dispersion relation, which challenges its theorization. Added to the difficulty is the incomplete observation of the complex spatial-temporal structure of the atmosphere. Faced with these difficulties, during the formative stage of dynamic meteorology (through 1960s), the best approach (and perhaps the only hope at that time) was classical linear theories of baroclinic instability and wave-mean flow interaction.

If the dynamics were linear and all waves were neutral, the observed periodicity in the eddy amplitude would be understood in terms of wave dispersion through the superposition principle. On the other hand, if nonlinearity (interaction between eddy and the mean flow) is at the heart of the periodic behavior, as assumed in the works of *Lorenz* [1963a], *Pedlosky* [1970, 1971, 1982], and the nonlinear oscillator model of TB14 and AN14, then one needs to carefully scrutinize how eddy and mean flow interact with each other using real data.

A traditional diagnostic for the partitioning and interaction between eddy and the mean state is the Lorenz energy cycle [*Lorenz*, 1955]. Although widely used for 'interpreting' the underlying dynamics of eddy growth and decay, the energy budget is complete only in the global average and it cannot be partitioned into individual wave modes even

in the small-amplitude limit. In this thesis, I employ instead the recently developed *finite-amplitude wave activity* (FAWA) diagnostic [*Nakamura and Zhu*, 2010] which extends the classical mid-latitude theory for wave-mean flow interaction. As more fully explained in the next chapter, with FAWA I can diagnose wave activity of a materially conserved field with exactness, e.g. the net displacement of potential vorticity substance from the zonal line of equivalent latitude. This new diagnostic not only recovers the linear results in the small-amplitude limit, but also generalizes the non-acceleration theorem [*Charney and Drazin*, 1961] for an arbitrary eddy amplitude. Most notably, the budget of the vertically integrated FAWA is significantly simpler to interpret than the energy budget, and it can be closed at each latitude. Although the FAWA budget itself does not constrain the periodicity in the eddy amplitude, performing the spectral analysis for each term in the FAWA budget helps us understand the key dynamical processes around the BAM frequencies.

In this dissertation, I focus on the Southern Hemisphere summer as it exhibits a coherent annular structure in both time-mean flow and storm track density [*Hoskins and Hodges*, 2005; *Lee*, 2014] - an ideal condition for the application of the FAWA diagnostic. Not only does the region sustain the fascinating periodicity, it serves as a nature's testbed for how eddy and the mean flow interact.

Thematically, the next chapter builds a required theoretical framework and diagnostic of FAWA and mean flow; the third chapter applies the theory to the reanalysis products to examine the 20 - 30 day periodicity in the austral summer; the fourth chapter adopts a hierarchy of numerical models to explore the key processes that affect the eddy forcing spectra and the FAWA spectra. Chapter five concerns the mechanistic interpretation of the 20-30 day oscillation in the observation and models. The thesis concludes with a brief summary chapter.

CHAPTER 2

A DIAGNOSTIC THEORY FOR EDDY - MEAN FLOW INTERACTION

Over the last two decades there has been a substantial amount of work to quantify the variability of jet streams in the extratropical troposphere in reanalysis products [*Hartmann and Lo*, 1998; *Limpasuvan and Hartmann*, 2000; *Wallace*, 2000; *Thompson et al.*, 2000; *Lorenz and Hartmann*, 2001; *Lee and Kim*, 2003; *Gerber et al.*, 2008; *Simpson et al.*, 2013]. The jet variability in the mid-latitudes is largely eddy-driven and as such most existing work concerns the response of the mean flow to eddy forcing, but the corresponding variability in the driving eddy has received relatively scant attention.

A straightforward definition of eddy is the local departure from the zonal mean. This perspective is useful because of the anisotropic nature of the mid-latitude troposphere, i.e., the zonal flow is substantially stronger than the meridional flow. Eddies can be transient or stationary. This thesis focuses on the transient part, which is a reasonable assumption for studying the Southern Hemisphere storm track where the effects from topography are at best of secondary importance.

One can then partition moments of physical variables such as the zonally averaged kinetic energy into contributions from the eddy (EKE) and from the zonal-mean field (ZKE), as touched on in the footnote of page 3. The global energy cycle concerns conversion of energy between eddy and the zonal-mean state [*Lorenz*, 1955]. The energy conversion is often used to characterize repeated baroclinic eddy life cycles in the troposphere. The energy conversion arises because the globally averaged eddy energy is not conserved when the zonal-mean state is nonuniform (i.e., when it involves temperature gradients and wind shear) even if the dynamics is conservative. As a diagnostic, the energy conversion provides supportive evidence for the underlying processes (e.g. baroclinic instability) but does not explain why it is happening. Furthermore, since the energy cycle is closed only in the global mean, its local application causes a handful of complications [*Plumb*, 1983].

Given the limitation of the energy cycle as a diagnostic, I will develop an alternative, simpler theoretical framework suitable to quantify eddy - mean flow interaction in a latitude-by-latitude fashion. Tropospheric eddy-mean flow interaction is formulated in terms of the vertically integrated budget of *finite-amplitude wave activity* (FAWA). At each latitude the dynamics is governed by three coupled equations for the interior- and surface FAWA and the barotropic zonal-mean zonal flow. Although this diagnostic framework by itself does not predict periodicity, it provides a convenient platform with which to address the observed periodic behavior in the austral summer.

Section 2.1 recaps basic concepts and conventional wisdoms of mid-latitude eddy-mean flow interaction. Section 2.2 lays out the theoretical framework. The new theory not only highlights the dynamics of storm tracks but also introduces a broader perspective to the mid-latitude general circulation – global angular (pseudo-) momentum cycle.

2.1 Basic concepts

The large-scale dynamics of the mid-latitude atmosphere is well described by the primitive equations: a set of fundamental conservation laws, i.e., energy, mass, and momentum conservation, and the physical properties of the atmosphere. While the effects of latent heat of condensation can make a quantitative difference, the large-scale dynamics in the Earth's mid-latitude atmosphere is, to the lowest order, governed by dry processes[1]. Thus the dry part of primitive equations serves as an indispensable building block of the theoretical and numerical development for the dynamics of the mid-latitude atmosphere.

The primitive equations for the atmosphere are a simplified version of the more general equation of fluid dynamics (i.e. the Navier-Stokes equation) mainly in two ways: (1) the Earth's gravitational force sets the vertical stratification and balances the verti-

1. Admittedly, this is a major assumption, and the reader is reminded that thermodynamics processes also interact with the atmosphere, i.e. *Pierrehumbert* [2010] cautions in its preface: "The days are long gone when leading-edge problems could be found in planetary fluid dynamics alone, so even the student whose primary interests lie in atmosphere/ocean dynamics will need to know a considerable amount about the other bits of physics that make up the climate system."

cal pressure gradient (hydrostatic balance), and (2) the Earth's rotation gives rise to the Coriolis pseudo-force, which partially balances the horizontal pressure gradient force. Compared to the tropics, the vertical motion associated with large-scale circulation in the mid-latitudes is relatively weak, and the horizontal acceleration is dominated by the local projection of the Coriolis force (due to planetary rotation) and large-scale pressure gradient.

The traditional eddy-mean flow partition is performed in the Eulerian coordinate, in which the mean flow is defined as the zonally averaged flow field and eddy as the departure from it. One of the main roles of large-scale eddies in the atmosphere is to transport heat meridionally, and thus regulates the equator-to-pole temperature difference. At the same time, these large-scale eddies also redistribute angular momentum, which can modify the mean flow.

To quantify these transport processes and to understand the eddy-mean flow interaction, conventional wisdom consists of the following three steps:

1. *Simplify the system*: the introduction of quasigeostrophic (QG) approximation and the associated potential vorticity for the mid-latitude atmosphere.

2. *Understand why eddies appear*: the theory for baroclinic instability (a predictive theory but largely in the domain of linear dynamics).

3. *Diagnose the effects of eddy on the mean flow*: the transformed Eulerian mean (TEM) formalism (valid for nonlinear regimes but it is diagnostic), which describes the interaction between the mean flow and eddies.

I will briefly explain the above three points of conventional wisdom in the following three subsections. Though some of these concepts are well-documented in the literature and textbooks, they are laid out here as a foundation for this thesis and a useful background material that I will build on in the next section.

2.1.1 *Conventional wisdom one: simplify the system*

A materially conserved tracer always labels the same material elements and can be of great value for quantifying and delineating advective processes [2]. A fluid flow under the influence of rotation and stratification generally possesses a built-in dynamical tracer, potential vorticity (PV), that is materially conserved under adiabatic, frictionless flow [3].

In a strictly two-dimensional incompressible system, PV is simply the vertical component of absolute vorticity (twice the local spin rate of a fluid element).

In a baroclinic stratified atmosphere governed by the primitive equations with three conservation principles [4], the 'Ertel-Rossby PV' is conserved following the 3D flow velocity [*Rossby*, 1940; *Ertel*, 1942; *Hoskins et al.*, 1985]:

$$\frac{D}{Dt}P = 0, \quad where \quad P \equiv \frac{1}{\rho}\zeta \cdot \nabla\theta \tag{2.1}$$

where ζ is the absolute vorticity vector, θ is potential temperature, and ρ is density. The conserved quantity P has a unit of $Km^2kg^{-1}s^{-1}$ [5] and P increases monotonically from a negative value at the South Pole to a positive value at the North Pole, vanishing at the equator. What separates PV from other material tracers (such as chemical tracers) is that the thermal structure and velocity distribution of the entire atmosphere may be inverted from PV under certain balance relations between mass and momentum. For example this is certainly the case for the 2D incompressible flow, for which streamfunction may be inverted from absolute vorticity. Although this 'invertibility principle' does not apply to the Ertel-Rossby PV for the primitive equations, we will see below that the principle handily applies to its quasigeostrophic approximation.

2. The nonadvective process can be backed out by a quasi-conservative tracer.

3. The conservation of PV arises from the particle relabeling symmetry [*Salmon*, 1998].

4. A parcel of dry air will conserve (1) potential temperature (adiabatic), (2) mass, and (3) circulation.

5. Typical value of P in the mid-latitude troposphere is on the order of $10^{-6}Km^2kg^{-1}s^{-1}$, conventionally defined as one 'potential vorticity unit', or PVU.

Based on the observation that large-scale atmospheric motions evolve on a timescale longer than the rotation timescale, an important further simplification of the primitive equations - quasi-geostrophic PV (hereafter QGPV) equation - is introduced by *Charney* [1948]. The slowness of flow evolution is measured by a small Rossby number $R_o \equiv U/Lf_0$, where U and L are characteristic velocity and length scales of the motion, and f_0 is the characteristic Coriolis parameter. Also assuming that the departures from the solid body rotation and from horizontally uniform stratification are small, and that the smallness of these departures is also measured by the Rossby number R_o, one can perform a multiple scale analysis of the primitive equations with R_o as the sole small parameter (e.g. *Pedlosky* [1979]). The final result is the material conservation of QGPV written on the β-plane (x, y, z), entirely in terms of the geostrophic streamfunction ψ_g:

$$\frac{D_g}{Dt} q_g = 0, \quad q_g = f_0 + \beta y + \nabla_H^2 \psi_g + \frac{f_0^2}{\tilde{\rho}} \frac{\partial}{\partial z} \left[\tilde{\rho} \frac{\partial \psi_g / \partial z}{N^2} \right], \tag{2.2}$$

where D_g/Dt is material derivative following the geostrophic wind

$$(u_g, v_g) \equiv (-\partial \psi_g / \partial y, \partial \psi_g / \partial x), \tag{2.3}$$

where $z = -H \ln(p/p_0)$ is pressure pseudo-height, H is a constant scale height [6], $p_0 \equiv 1000 hPa$. β is the (constant) meridional gradient of the Coriolis parameter [7]; $\nabla_H^2 \psi_g$ is geostrophic relative vorticity, $N^2(z)$ is static stability (the Brunt-Väisälä frequency squared), and $\tilde{\rho} = \rho_0 e^{-z/H}$ is the density of the one-dimensional background state.

The QG system allows us to focus exclusively on the slowly evolving large-scale eddies because it filters the large Rossby number (fast) dynamics such as inertia-gravity waves. Since the second equation in (2.2) is an elliptic equation, q_g can be inverted to back out the winds and thermal structure through ψ_g, as long as the boundary conditions

6. This thesis assumes a scale height of 7 km for all subsequent calculation.

7. Note that the formal QGPV equation is only valid on the β plane, although in the subsequent chapters a local f on the sphere is used for the diagnostics purpose.

for ψ_g are provided. In particular, the lower boundary condition for ψ_g is determined by geostrophic advection of 'temperature' $\partial\psi_g/\partial z$ [8]. The appropriate boundary conditions, along with an initial condition, allow QGPV to be a sole prognostic variable, which can be integrated forward in time with no other equations. In other words, for this system, equation (2.2) is effectively *the* equation of motion [*Hoskins et al.*, 1985]. This simplifies greatly the description and prediction of the mid-latitude atmospheric flow.

Figure 2.1 compares different flavors of PV in the upper troposphere. Even though the Ertel-Rossby PV is conserved following the 3D velocity, if one uses the isentropic coordinate, the vertical velocity is absorbed in the movement of the coordinate so the Ertel-Rossby PV is advected by the horizontal, isentropic wind (in the adiabatic limit). The Ertel-Rossby PV in the isentropic coordinate (top panel) is simply the absolute vorticity divided by the isentropic density. This, together with its 2D advection, simplifies the analysis and reduces numerical noise – for example, PV computed in the isentropic coordinate is smoother than PV computed from equation (2.1) (middle panel). However the isentropic analysis has difficulty in handling the lower boundary condition, where isentropes intersect with the surface. QGPV (bottom panel) is conserved on the pseodo-height surface and the lower boundary condition is straightforward, which greatly simplies the analysis. As shown in Figure 2.1, all flavors of PV capture equally well the pole-to-equator gradient largely reflecting the latitudinal dependence of the Coriolis parameter, the large-scale meridional excursion of air masses by the eddies, and the concentrated PV gradients along the folded dynamical tropopause in the mid-latitudes. The material conservation of QGPV under an eddying circulation will prove an important asset in developing the diagnostic theory in section 2.2.

8. More precisely, $\partial\psi_g/\partial z = (R/(f_0 H))T$, where R is gas constant.)

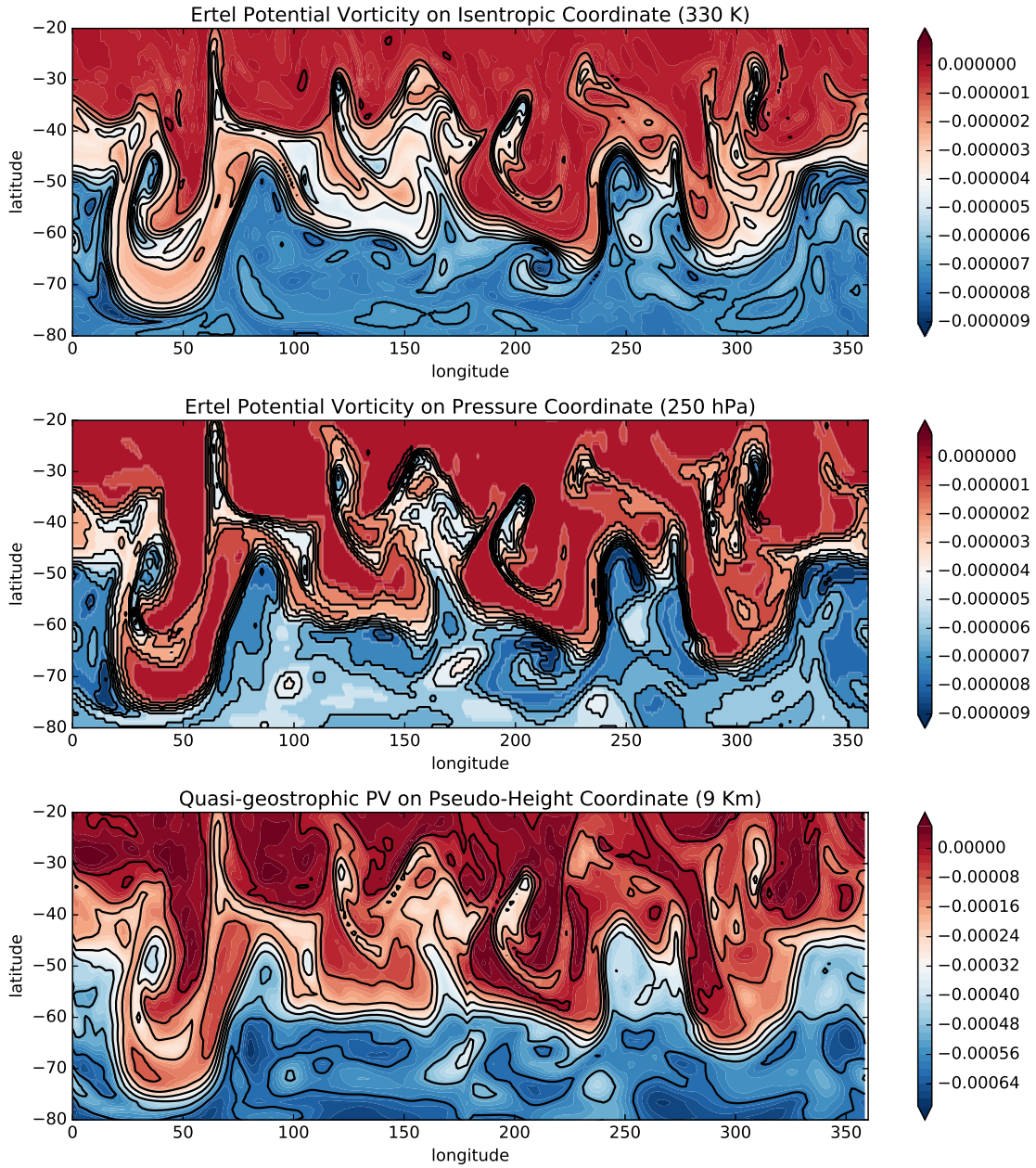

Figure 2.1: (Upper) Ertel-Rossby PV on isentropic coordinate at 330 K. (Middle) Ertel PV interpolated on pressure coordinate at 250 hPa. (Bottom) Quasi-geostrophic PV on pseudo-height coordinate at 9 Km. In the calculation of QGPV, Coriolis parameter in (2.2) has been replaced by the local value $f = 2\Omega \sin\phi$, where ϕ is the latitude. All panels are snapshots of respective PV on December 15, 2011 and based on ERA-Interim products. Contour interval for Ertel PV is $10^{-6} K m^2 kg^{-1} s^{-1}$ and contour interval for QGPV is $10^{-4} s^{-1}$.

2.1.2 Conventional wisdom two: understand why eddies appear

The QGPV equation allows us to formulate a simplified theoretical model of the mid-latitude troposphere, in which finite-amplitude transient perturbations – Rossby waves – appear and propagate. In the mid-latitudes, these perturbations primarily arise from orography, land-sea contrast, or baroclinic instability. When the surface is largely covered by the oceans and the orographic forcing is weak, baroclinic instability plays the leading role in generating large-scale eddies. This is the case in the Southern Hemisphere storm track, the nature of which will be examined in detail in Chapter three.

The rapid rotation of the Earth maintains the equator-to-pole temperature gradient but such a mean state is unstable to infinitesimal wavy perturbations at large scales; they grow at the expense of the available potential energy of the mean state. Intuitively, baroclinic instability can be understood as a mechanism through which the atmosphere adjusts the slope of isentropes in response to the differential heating between the pole and the equator. When the Earth is differentially heated, isentropic surfaces that distinguish material elements with different entropy are slanted. Such a slanted configuration of isentropes supports a set of bottom-trapped perturbations ('edge waves') propagating eastward relative to the background flow. At the same time in the interior of the mid-latitude atmosphere, the positive meridional PV gradients support Rossby waves propagating westward relative to the background zonal flow. The edge waves and the Rossby waves are vertically stacked. Each individual vortex point in propagating waves induces environmental flow patterns, which allows the two stacked perturbations to interact with each other. In the presence of Doppler shift by a vertically sheared mean flow (due to the meridional temperature gradient through thermal wind balance), these infinitesimal vortices of the two wave types may be phase-locked and mutually reinforcing, growing exponentially. Such mutual amplification eventually flattens the slanted isotrope, since the growing baroclinic waves transport heat poleward.

This process can be summarized succinctly by the dynamics of linear *wave activities*,

second moments of QGPV and surface temperature anomalies. The linear wave activities in the interior and at the surface are defined as:

$$A_{lin} \equiv \frac{\overline{q'^2}}{2\partial\overline{q_g}/\partial y}, \tag{2.4}$$

$$B_{lin} \equiv \frac{f_0^2}{2N_0^2 H} \frac{\overline{(\partial\psi_g'/\partial z)^2}}{\partial^2\overline{\psi_g}/\partial y \partial z}\bigg|_{z=0}. \tag{2.5}$$

Defining the density-weighted vertical average

$$\langle(\,\cdot\,)\rangle \equiv \int_0^\infty e^{-z/H}(\,\cdot\,)dz \Big/ \int_0^\infty e^{-z/H}dz, \tag{2.6}$$

and the meridional average denoted by square brackets, it is straightforward to manipulate the linearized version of the QGPV equation (2.2) and the lower boundary condition to derive the conservation of the total wave activity [*Charney and Stern*, 1962; *Pedlosky*, 1964]:

$$\frac{\partial}{\partial t}\left[\langle A_{lin}\rangle + B_{lin}\right] = 0. \tag{2.7}$$

If the zonal-mean PV gradient and the zonal-mean surface temperature gradient (divided by the Coriolis parameter) are of the same sign everywhere in the domain, then without violating the total wave activity conservation law (2.7), the total wave activity cannot grow (or decay) everywhere simultaneously. This is a sufficient condition for eddy fields to be modally stable. Conversely, a necessary condition for modal instability is that the zonal-mean PV gradient and/or the zonal-mean surface temperature gradient take on both signs somewhere in the domain, a theorem well known as the Charney-Stern-Pedlosky stability criterion. For the Earth's mid-latitudes $\partial\overline{q_g}/\partial y$ is almost everywhere positive in the interior of the atmosphere, whereas $\partial^2\overline{\psi_g}/\partial y\partial z$ at the surface (the zonal mean temperature gradient divided by f) is almost everywhere negative, so the necessary

condition for instability is met. The wave activity of the interior Rossby waves [$< A_{lin} >$] is therefore positive and the wave activity of the surface edge waves [B_{lin}] is negative. Their mutual reinforcement makes the former more positive and the latter more negative, while their sum being invariant (actually zero) through equation (2.7). The agent of their mutual reinforcement is the low-level meridional eddy heat flux, which acts as a vertical radiation stress between the waves.

This above process, known as baroclinic instability, is conventionally investigated through a linearized QGPV equations [*Charney*, 1947; *Eady*, 1949; *Phillips*, 1951], which by construction assumes that eddies are of small amplitude. A linearized system comes with eigenvalues and eigenvectors. When instability occurs (eigenvalues are complex), the mathematical solution of the small amplitude eddy can grow exponentially, creating an instability mechanism that gives rise to and maintain the amplitude and size of eddies in the observed atmosphere.

2.1.3 Conventional wisdom three: diagnose eddies' effects on the mean flow

Large-scale eddies in the atmosphere governed by the quasigeostrophic dynamics usually move at a certain speed and maintain coherent structures. The horizontal phase tilts in the eddies' geometry give rise to the Reynolds stress, which, when convergent, modifies the mean flow. With the quasigeostrophic scaling, the zonal-mean zonal wind equation in the Eulerian coordinate reads:

$$\frac{\partial \overline{u}}{\partial t} = f_0 \overline{v} - \frac{\partial}{\partial y} \overline{u'v'}. \tag{2.8}$$

The above formula shows that the two terms on the RHS, the Coriolis torque due to the mean meridional circulation and the eddy momentum flux convergence, drive the local change of zonal-mean zonal momentum. This interpretation leads to a conundrum because the two RHS terms are intrinsically connected with each other because the mean

meridional circulation in the mid-latitudes is largely eddy-driven. What's more, these two terms are often of similar magnitude and largely cancel each other [9], rendering only a small residual as the *de facto* driving force for the zonal-mean flow. As a result, equation (2.8) is not terribly revealing as to the origin of the net eddy forcing on the zonal-mean zonal flow.

A workaround is to use a different accounting method: the *transformed Eulerian mean* (TEM) diagnostic formalism [*Andrews and McIntyre*, 1976]. The TEM framework combines both momentum equation and thermodynamics equation, with the understanding that eddies alter not only the zonal-mean zonal momentum through the Reynolds stress but also the zonal-mean thermal structure through the heat fluxes. The TEM zonal momentum equation reads:

$$\frac{\partial \overline{u}}{\partial t} = f_0 \overline{v}^* + \frac{1}{\tilde{\rho}} \nabla_{yz} \cdot \mathbf{F}, \tag{2.9}$$

where the horizontal residual velocity [10] is:

$$\overline{v}^* = \overline{v} - \frac{1}{\tilde{\rho}} \frac{\partial}{\partial z} \left(\frac{\tilde{\rho} \overline{v'\theta'}}{d\tilde{\theta}_0/dz} \right) \tag{2.10}$$

and the vector $\mathbf{F}$ is the Eliassen-Palm (E-P) flux density [*Eliassen and Palm*, 1961; *Andrews and McIntyre*, 1976], whose divergence equals the zonal-mean meridional flux of eddy QGPV:

$$\frac{1}{\tilde{\rho}} \nabla_{yz} \cdot F = \overline{v' q'_g}, \quad \mathbf{F} = \left(-\tilde{\rho} \overline{u'v'}, \ \frac{\tilde{\rho} f_0}{d\tilde{\theta}_0/dz} \overline{v'\theta'} \right), \tag{2.11}$$

and the gradient operator is defined in the $y-z$ plane:

$$\nabla_{yz} \equiv \left(\frac{\partial}{\partial y}, \frac{\partial}{\partial z} \right). \tag{2.12}$$

9. The two RHS terms of (2.8) exactly balance each other in the time mean, but the cancellation is significant even without time averaging.

10. Although the eddy flux terms in equations (2.10), (2.11), and (2.17) are expressible solely in terms of geostrophic streamfunction, here we use velocity and potential temperature to aid physical interpretation.

The above identity (2.11) is known as *Taylor's identity*. Meanwhile, it is readily shown that the local sink or source of wave activity is due to a divergence of the E-P flux vector:

$$\frac{\partial A_{lin}}{\partial t} + \frac{1}{\tilde{\rho}} \nabla_{yz} \cdot \mathbf{F} = O(\alpha^3), \tag{2.13}$$

where A_{lin} is the linear wave activity defined by equation (2.4) and the RHS denotes terms whose order of magnitude is cubic (or higher) in wave amplitude. Equation (2.13) is known as the *generalized Eliassen-Palm relation* [*Andrews and McIntyre*, 1976].

The reason why equation (2.9) is favored over (2.8) is that, in the small-amplitude limit, the E-P flux density equals $\tilde{\rho} c_g A_{lin}$, where c_g is the group velocity of the Rossby wave. Therefore the E-P flux becomes the flux of wave activity (pseudomomentum) carried by the Rossby wave packet. In equations (2.9) and (2.13), the vector **F** describes how wave activity (pseudomomentum) is transmitted within the atmosphere from one location (latitude-height) to another and how it modifies the mean flow (zonal-mean zonal momentum). The QGPV flux, or equivalently the divergence of the E-P flux, directly drives the mean flow and alters wave activity at the same rate, analogous to the action-reaction relation. One can appreciate this by eliminating the eddy forcing terms from equations (2.9) and (2.13) to form:

$$\frac{\partial \overline{u}}{\partial t} = -\frac{\partial A_{lin}}{\partial t} + f_0 \overline{v}^* + O(\alpha^3). \tag{2.14}$$

The acceleration of the zonal wind is achieved at the expense of wave activity. This action-reaction relation is rigorous only when the residual circulation and the wave amplitude are both small so that the last two terms of (2.14) are negligible.

In reality, the residual circulation and the E-P flux divergence can have comparable values in the upper troposphere [11] [*Pfeffer*, 1987; *Nakamura and Solomon*, 2010]. The

11. This is not a general feature for all fluids. For example, in the Southern Ocean, the eddy overturning circulation and the wind-driven mean overturning circulation are of the similar magnitude but opposite in sign, canceling each other leaving a quite small residual circulation [*Marshall and Speer*, 2012].

relative magnitude of the Coriolis torque of the residual circulation and of the E-P flux divergence with respect to the acceleration of the zonal-mean zonal wind depends on the vertical versus horizontal aspect ratio of the E-P flux divergence. A deep eddy forcing tends to drive the zonal-mean zonal flow, whereas a shallow eddy forcing drives the residual circulation [*Pfeffer*, 1987].

The linear form of wave activity A_{lin} [equation (2.4)] is easy to diagnose from the data but only accurate to the second order in wave amplitude. When the QGPV gradient in the denominator changes sign, A_{lin} can become spuriously large and eventually negative (as will be seen in Figure 3.2 below). This limitation can be overcome by the *finite-amplitude wave activity* to be introduced in the next section.

Similar to the momentum equation (2.8), the Eulerian-mean thermodynamic equation is:

$$\frac{\partial \overline{\theta}}{\partial t} = -N^2 \overline{w} - \frac{\partial}{\partial y} \overline{v'\theta'} + \overline{S}, \tag{2.15}$$

where $\overline{S}$ denotes the zonal-mean nonadiabatic heating (radiation and convection).

The corresponding TEM thermodynamic equation is:

$$\frac{\partial \overline{\theta}}{\partial t} = -N^2 \overline{w}^* + \overline{S}, \tag{2.16}$$

where the vertical residual velocity is given by:

$$\overline{w}^* = \overline{w} + \frac{\partial}{\partial y}\Big(\frac{\overline{v'\theta'}}{d\tilde{\theta}_0/dz} \Big). \tag{2.17}$$

In the TEM thermodynamic equation (2.16), the zonal-mean potential temperature is driven solely by the vertical residual circulation in the adiabatic limit. In the interior of the troposphere, $\overline{w}^*$ is upward in the tropics (cooling) and downward in the extratropics (warming) and hence acts to reduce the slope of the isentropes. This tendency is balanced by radiative-convective heating in the tropics and radiative cooling in the extratropics.

The residual circulation [equations (2.10) and (2.17)] represents the difference be-

tween the mean meridional circulation and the eddy overturning circulation driven by the meridional eddy heat flux. By eliminating the tendency terms from equations (2.9) and (2.16) using the thermal wind balance, one can derive an elliptic equation for the streamfunction of the residual circulation, in which gradients of the E-P flux divergence and the nonadiabatic heating appear as inhomogeneous 'forcing' terms. Since the radiative heating is a slow process in the troposphere, the residual circulation is primarily driven by the E-P flux divergence (the eddy QGPV flux). In addition to the direct forcing that they exert on the zonal-mean zonal flow [euqation (2.9)], the eddies modify the zonal-mean state indirectly through the residual circulation. In summary, the TEM framework encapsulates the central role of the QGPV flux as eddy forcing on the zonal mean state[12].

12. The TEM formalism emphasizes the eddy's impact on the zonal-mean state, but the interaction works in both ways. For example, it is worth mentioning that the horizontal shear of the zonal-mean zonal wind has a strong impact on the mid-latitude's eddy growth [*James and Gray*, 1986; *James*, 1987], particularly in the lower troposphere [*Hartmann*, 2000]. As the barotropic wind shear increases, the meridional scale of the unstable modes becomes smaller and they can tap less available potential energy stored in the domain before leading to irreversible barotropic decay. This feedback effect suppresses further baroclinic growth [*Nakamura*, 1993]. This *barotropic governor* mechanism also operates in the inverse energy cascade range of geostrophic turbulence.

2.2 Finite-amplitude wave activity (FAWA) theory

In the TEM set of *Andrews and McIntyre* [1976] summarized in the previous section, the generalized Eliassen-Palm relation (2.13) is accurate only up to second order in eddy amplitude. *Finite-amplitude wave activity* (FAWA) or *pseudomomentum* [*Nakamura and Zhu*, 2010, hereafter NZ10] [*Nakamura and Solomon*, 2010, 2011] was recently developed to address this shortcoming.

In this section [13], I will develop a simple diagnostic framework for eddy-mean flow interaction based on the budget of FAWA. For a purely barotropic flow, the theory predicts that the sum of the zonal-mean zonal flow and FAWA remains constant at each latitude under conservative dynamics, a direct result of Kelvin's circulation theorem [NZ10]. In this limit the zonal-mean zonal flow grows at the expense of FAWA and vice versa, so their variation is antiphase [for a barotropic flow there is no residual circulation, A_{lin} is replaced by FAWA, and there is no cubic eddy term in equation (2.13)]. We will see that an analogous eddy-mean flow interaction in the real atmosphere entails covariation of three key quantities: the barotropic zonal-mean zonal wind and the interior- and surface FAWA at each latitude. The three quantities are driven by the interior eddy momentum flux convergence and the low-level meridional eddy heat flux but also modified by non-conservative processes such as frictional and thermal damping. This three-component model will be our baseline diagnostic theory for characterizing the eddy-mean flow interaction in the mid-latitude atmosphere.

13. An earlier version of this material in this section appeared in *Wang and Nakamura* [2015] (©American Geophysical Union. Used with permission.) and *Wang and Nakamura* [2016] (©American Meteorological Society. Used with permission.)

2.2.1 *Density-weighted, vertically averaged FAWA*

FAWA is defined as the net displacement of a materially conserved substance from the zonal line of equivalent latitude. In this study, I use quasigeostrophic potential vorticity (QGPV) to define the interior FAWA

$$A(\phi, z, t) = \frac{1}{2\pi a \cos\phi} \left(\iint\limits_{\phi' \le \phi} q_g dS - \iint\limits_{q_g \le Q} q_g dS \right), \tag{2.18}$$

where a is the radius of the planet, λ and ϕ are longitude and latitude, $z = -H \ln(p/p_0)$ is pressure pseudoheight, $dS = a^2 \cos\phi' d\phi' d\lambda$ is the area element, and QGPV is defined in equation (2.2) [14].

In equation (2.18), $Q(\phi, z, t)$ is the value of the q_g contour such that the wavy PV contour $q_g = Q$ encloses the same area as the region south of latitude ϕ. (Note that the surface integrals extend northward from the South Pole.)

The second integral in (2.18) is constant in time even when the bounding QGPV contour is transient and wavy, because QGPV is materially conserved. However, the waviness of the bounding contour implies that a net 'exchange' of high and low PV has taken place across the latitude line ϕ, and FAWA measures the amount of such exchange. This eddy-mean state partition based on the hybrid Eulerian-Lagrangian averaging allows FAWA to quantify the exact pseudomomentum carried by eddies [NZ10 Eq. (11)].

Similarly, I use the surface potential temperature to define surface FAWA B [NZ10 Eq. (41)]:

$$B(\phi, t) = \frac{f}{2\pi a \cos\phi H(\partial\tilde{\theta}/\partial z)} \left(\iint\limits_{\phi' \le \phi} \theta dS - \iint\limits_{\theta \le \Theta} \theta dS \right), \tag{2.19}$$

where θ and $\partial\tilde{\theta}/\partial z$ are evaluated at the surface. When there is topography $z = \eta_B(\lambda, \phi)$, θ

14. In the spherical coordinate, the Coriolis and the β terms are replaced by the latitude dependent Coriolis parameter $f = 2\Omega \sin\phi$, where $\Omega = 7.29 \times 10^{-5} s^{-1}$ is the Earth's rotation rate.

is replaced by $\theta_{z=0} + \eta_B (\partial\tilde{\theta}/\partial z)_{z=0}$ [15]. Note $A \geq 0$ and $B \leq 0$ by construction. The small-amplitude limits of equations (2.18) and (2.19) recover the linear definitions [equations (2.4) and (2.5)].

A and B satisfy the governing equations [NZ10]

$$\frac{\partial A}{\partial t} = -\overline{v'q'_g} + \dot{A} = \frac{1}{a\cos^2\phi}\frac{\partial}{\partial\phi}\left(\overline{u'v'}\cos^2\phi\right) - f e^{z/H}\frac{\partial}{\partial z}\left(\frac{e^{-z/H}\overline{v'\theta'}}{\partial\tilde{\theta}/\partial z}\right) + \dot{A}, \tag{2.20}$$

$$\frac{\partial B}{\partial t} = -\left.\frac{f\overline{v'\theta'}}{H(\partial\tilde{\theta}/\partial z)}\right|_{z=0} + \dot{B}, \tag{2.21}$$

where the overbar and prime denote the zonal average and departure from it, respectively, and $\dot{A}$ and $\dot{B}$ denote nonconservative sources and sinks of A and B, the latter primarily through the exchange of heat with the underlying land or sea surface. The last expression of (2.20) arises from Taylor's identity (2.11) that connects the eddy QGPV flux with the divergence of the E-P flux density.

Although identical to the traditional TEM set in the previous section, a major strength of equations (2.20) and (2.21) is that they are valid for an arbitrary eddy amplitude.

In the quasigeostrophic approximation the zonal-mean zonal velocity obeys

$$\frac{\partial\bar{u}}{\partial t} = f\bar{v} - \frac{1}{a\cos^2\phi}\frac{\partial}{\partial\phi}\left(\overline{u'v'}\cos^2\phi\right) + \dot{U}, \tag{2.22}$$

where $\dot{U}$ denotes forcing such as surface friction and gravity wave drag. This is a spherical generalization of equation (2.8).

Applying the density-weighted vertical average [(2.6)] to (2.20) and (2.22), one obtains

$$\frac{\partial}{\partial t}\langle A\rangle = \frac{1}{a\cos^2\phi}\frac{\partial}{\partial\phi}\left\langle\overline{u'v'}\cos^2\phi\right\rangle + \left.\frac{f\overline{v'\theta'}}{H(\partial\tilde{\theta}/\partial z)}\right|_{z=0} + \left\langle\dot{A}\right\rangle, \tag{2.23}$$

15. For the analysis of the Southern Hemisphere storm track in the next section the topography was ignored ($\eta_B = 0$).

$$\frac{\partial}{\partial t}\langle\bar{u}\rangle = -\frac{1}{a\cos^2\phi}\frac{\partial}{\partial\phi}\left\langle\overline{u'v'}\cos^2\phi\right\rangle + \left\langle\dot{U}\right\rangle, \tag{2.24}$$

where $\langle\bar{v}\rangle = 0$ was assumed (no net meridional transport of mass). Because of the density weighting, the vertical average primarily samples the troposphere [see a recent discussion in *Huang and Nakamura*, 2016].

From equations (2.21), (2.23), (2.24), one can eliminate the eddy flux terms:

$$\frac{\partial\langle\bar{u}\rangle}{\partial t} = -\frac{\partial}{\partial t}\left(\langle A\rangle + B\right) + \left(\left\langle\dot{U}\right\rangle + \left\langle\dot{A}\right\rangle + \dot{B}\right). \tag{2.25}$$

In the absence of nonconservative effects, the barotropic zonal-mean wind $\langle\bar{u}\rangle$ increases entirely at the expense of $\langle A\rangle + B$. In this limit, the mean flow anomaly (departure from the time-mean) and the wave activity anomaly will be opposite of each other:

$$\Delta\langle\bar{u}\rangle = -\Delta\left(\langle A\rangle + B\right). \tag{2.26}$$

This is a vertically averaged, finite-amplitude extension to the *nonacceleration theorem*, first introduced by *Charney and Drazin* [1961] for small-amplitude baroclinic Rossby waves [c.f. (2.14) above]. At each latitude, the barotropic component of the zonal-mean wind covaries with the sum of the interior and surface finite-amplitude wave activities.

2.2.2 *Globally averaged FAWA and global momentum cycle*

As shown above, the interaction between large-scale eddies and the zonal-mean zonal wind in the Earth's mid-latitude atmosphere is expressed succinctly in the TEM formalism of *Andrews and McIntyre* [1976], which has subsequently been extended to finite-amplitude Rossby waves and balanced eddies (NZ10).

Figure 2.2 summarizes the zonal momentum-wave activity cycle defined by equations (2.21), (2.23), (2.24) *at each latitude*. The direction of the arrows in Figure 2.2 is typical

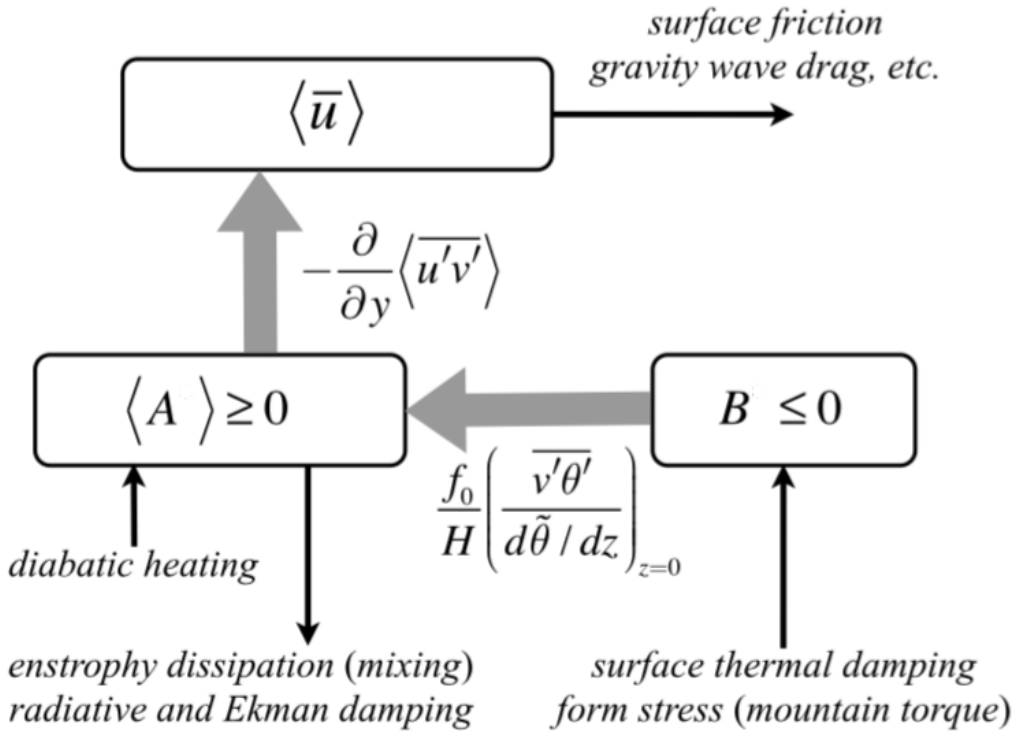

Figure 2.2: Zonal momentum-wave activity cycle as expressed in equations (2.21), (2.23), and (2.24). The fat gray arrows indicate eddy fluxes whereas the thin black arrows indicate sources and sinks. The directions of the arrows are representative of the latitudes for a baroclinically unstable, eddy-driven jet. See text for details. (appeared in *Wang and Nakamura* [2016]. ©American Meteorological Society. Used with permission.)

of a baroclinically unstable, eddy-driven jet. A poleward surface eddy heat flux transfers wave activity from B to $\langle A \rangle$, making the former more negative and the latter more positive. This represents baroclinic instability and vertical propagation of Rossby waves forced at the surface, among other things. The convergence of eddy momentum flux drives $\langle \bar{u} \rangle$ at the expense of $\langle A \rangle$ (e.g., barotropic decay of baroclinic eddies; *Randel and Stanford* [1985]). External sinks include surface drag on $\langle \bar{u} \rangle$ and loss of $\langle A \rangle$ through mixing (i.e. enstrophy dissipation) and radiative and Ekman damping (NZ10). On the other hand, diabatic heating (latent heat of condensation) can be a source of $\langle A \rangle$ and offset some of its dissipation. Surface thermal damping of B also works as a source of wave activity because B is negative. In the quasigeostrophic framework, form stress by topography also constitutes a source of wave activity through the boundary potential temperature anomaly (and hence B). For a vertically propagating neutral Rossby wave forced at the surface, the form stress and the meridional eddy heat flux balance the budget of B.

Compared to the global energy cycle of *Lorenz* [1955], the zonal momentum-wave activity cycle has two advantages for describing eddy-mean flow interaction:

- Unlike the energy cycle its budget is closed at each latitude, allowing the meridional structure of the eddy - mean flow interaction to be described;

- The sole eddy forcing for the total FAWA $< A > + B$ is the convergence of the meridional eddy momentum flux, whereas the total eddy energy is driven by barotropic *and* baroclinic conversions, whose directions also depend on the choice of the coordinate (see a detailed discussion in *Plumb* [1983]).

When averaged over a band of latitudes to even out the convergence and divergence of the vertically integrated eddy momentum flux, equations (2.23) and (2.21) become (the latitudinal average is denoted by the square bracket):

$$\frac{\partial}{\partial t}\left[\langle A \rangle\right] = \frac{1}{H}\left[\frac{f\overline{v'\theta'}}{d\tilde{\theta}/dz}\right]_{z=0} + \left[\left\langle \dot{A} \right\rangle\right], \tag{2.27}$$

$$\frac{\partial}{\partial t}[B] = -\frac{1}{H}\left[\frac{f\overline{v'\theta'}}{d\tilde{\theta}/dz}\right]_{z=0} + \left[\dot{B}\right]. \tag{2.28}$$

In the conservative limit where the last terms in (2.27) and (2.28) are negligible, the global budget of FAWA is governed solely by the surface eddy heat flux and the domain integral of wave activity (sum of the interior and surface contributions) is conserved:

$$\frac{\partial}{\partial t}\left([\langle A\rangle] + [B]\right) = 0. \tag{2.29}$$

This last constraint may be used to extend the Charney-Stern-Pedlosky criterion for modal baroclinic instability for finite amplitude [*Charney and Stern*, 1962; *Pedlosky*, 1964; *Nakamura and Zhu*, 2010]: for the domain averaged interior and surface FAWAs to grow simultaneously without violating (2.29), they must have opposite sign. This condition is met for the Earth's atmosphere since $A \geq 0$ and $B \leq 0$ (NZ10). In the nonconservative limit, time averaging (denoted by curly bracket) of equations (2.27) and (2.28) gives

$$\frac{1}{H}\left\{\left[\frac{f\overline{v'\theta'}}{d\tilde{\theta}/dz}\right]_{z=0}\right\} = \left\{\left[\dot{B}\right]\right\} = -\left\{\left[\left\langle\dot{A}\right\rangle\right]\right\}. \tag{2.30}$$

Therefore, the time-mean latitudinal-mean surface eddy heat flux (poleward in the Earth's atmosphere) is proportional to the mean damping rate of both surface and interior FAWAs. In this case the inflows and outflows balance for the two bottom boxes in Figure 2.2 (eddy momentum flux convergence and frictional damping of $\langle\bar{u}\rangle$ vanish upon latitudinal average).

In the next chapter I will use the wave activity budget described in this chapter to explore the anatomy of the observed periodicity in the austral summer storm track.

CHAPTER 3

OBSERVED PERIODICITY IN THE SOUTHERN HEMISPHERE STORM TRACK

In this chapter [1], I apply the theory developed in Chapter 2 to the Southern Hemisphere (SH) storm track to quantify its periodic behavior, as alluded to by the remote sensing of surface variables in Chapter 1. The surface of the SH storm track is largely covered by the oceans and orographic forcing is weak, hence the internal dynamics of the atmosphere - baroclinic instability - dominates. The modulation of wind speeds and rain rate seen in Figure 1.4 should therefore be related to the modulation of the baroclinic eddy activity. At the same time, the modulation of eddy amplitude implies a simultaneous modulation of the zonal-mean state.

Based on the theoretical considerations in Chapter 2, I expect a covariation of FAWA and the mean flow. In this chapter, I will show that in the austral summer, a robust covariation of FAWA and the mean flow exists between 40 - 55 S on timescales around 25 days yet the periodicity and amplitude of variation are more pronounced in FAWA than in the zonal-mean flow. These findings corroborate the previous results on the BAM. I will then show that strong thermal damping on surface FAWA, together with distinct spectral shapes of the low-level meridional eddy heat flux and the interior eddy momentum flux convergence, explains this asymmetry as well as why the wave activity variability of the BAM is dominated by the eddy heat flux. Finally, with a spectral decomposition of the FAWA budget I will demonstrate that the nature of eddy-mean flow interaction varies significantly depending on the timescales.

The chapter is organized as follows. Section 3.1 outlines the diagnostic method and datasets. Section 3.2 shows the budgets of the vertically integrated FAWA where a pe-

1. An earlier version of this material in this chapter appeared in *Wang and Nakamura* [2015] (©American Geophysical Union. Used with permission.) and *Wang and Nakamura* [2016]. (©American Meteorological Society. Used with permission.)

riodicity is identified in 40 - 55 S during the austral summer, and emphasizes the importance of the low-level meridional eddy heat flux for driving this periodicity. Section 3.3 investigates the seasonality of the observed eddy forcing spectra and the zonal-mean background state. I will also compare FAWA and EKE as diagnostics of the BAM. Section 3.4 summarizes the results.

3.1 Diagnostic method and data

I use four times daily reanalyses for winds and temperature from the European Centre for Medium-Range Weather Forecasts ERA-Interim datasets [*Dee et al.*, 2011] for 1979-2013. The horizontal resolution of the adopted dataset is 1.5 degrees (approximately 150 km near the equator), although the ERA-Interim atmospheric model has a T255 spherical-harmonic representation (approximately 80 km near the equator) for key dynamical fields.

In what follows equations (2.21), (2.23) and (2.24) are evaluated from meteorological data at each latitude and time, the nonconservative terms being the residual of the budget [2].

Quasigeostrophic PV (see Chapter 2.1.1 for details) is calculated following the procedures described in *Nakamura and Solomon* [2010]. In particular, the analysis is performed on 49 evenly spaced (1 km) pressure pseudo-height after vertically interpolating the data from the original 37 pressure levels.

The main difficulty in applying the theory to data is the treatment of the lower boundary, which is commonly raised to 850 hPa to avoid the complications due to the boundary layer [*Hoskins et al.*, 1985]. However this invalidates equation (2.21) because the vertical advection of heat is not negligible at the top of the boundary layer, unless $\dot{B}$ is reinterpreted to absorb it. On the other hand, placing the boundary at the sea level involves (in

2. The residual also contains analysis or numerical errors which are not explicitly evaluated in this thesis.

addition to the departure from quasigeostrophy in the boundary layer) difficulty in evaluating the surface static stability accurately, the uncertainty of which can be as large as a factor of 2. In this study I discretize Taylor's identity [see equation (2.11)] in the vertical such that the boundary values are evaluated as a weighted average of the values at the two lowest levels (z = 0 and 1 km). This effectively places the lower boundary within the boundary layer, with static stability more or less representing the layer-averaged value. The result is, as it turns out, not too different from the case in which the boundary is raised to the top of the boundary layer. I also ignore topography, which is probably permissible for the SH mid-latitudes. As we will see, the key findings presented in this study remain largely unaffected by the uncertainty in the boundary values.

The analysis will be shown for the austral summer (December-February; for spectral analysis also March) and for the austral winter (June-August; for spectral analysis also September), respectively. I remove the mean seasonal cycle, which is defined as the annual average plus the first four Fourier modes for the climatological seasonal cycle [3], consistent with *Lorenz and Hartmann* [2001]. When spectral analysis is presented, data is windowed for the respective periods by the Hamming window (see technical explanations in *Oppenheim and Schafer* [2009]).

3. The climatological seasonal cycle is calculated based on the 35 year data.

3.2 Periodic behavior in austral summer

3.2.1 Covariation of FAWA and mean flow in austral summer

The main driver of eddy-mean flow interaction in the mid-latitudes is synoptic baroclinic eddies [*Hartmann and Lo*, 1998; *Lorenz and Hartmann*, 2001] [4] . Strong interaction between the zonal mean flow and finite-amplitude eddies fosters dynamically rich behaviors in the Earth's mid-latitude atmosphere. The SH summer exhibits a coherent annular structure in both time-mean flow and storm track density [*Hoskins and Hodges*, 2005; *Lee*, 2014], therefore it is an ideal place to observe such interaction.

An example of covariation of the mean flow and wave activity is shown in Figure 3.1, analyzed for 46.5 S from December 2011 through February 2012. This latitude is at the center of the latitudinal band in which surface EKE shows strong periodicity during the austral summer (Figure 1.4). The top two panels show the time-height cross sections of $\Delta\bar{u}$ and ΔA (departures from seasonal-mean values). While $\Delta\bar{u}$ is vertically coherent from the surface to the lower stratosphere [*Thompson et al.*, 2000], ΔA is more localized to the upper troposphere as a result of concentrated PV gradients near the tropopause [*Nakamura and Solomon*, 2010, 2011].

Despite the different structures, once vertically averaged, $\Delta\langle\bar{u}\rangle$ and $\Delta(\langle A\rangle + B)$ largely compensate each other, as shown by the black and red curves in the third panel of Figure 3.1. This is consistent with equation (2.26). Because of its negative values the surface wave activity B is supposed to offset some of the interior wave activity $\langle A\rangle$ and its anomaly. However, the very small difference between $\Delta(\langle A\rangle + B)$ (red) and $\Delta\langle A\rangle$ (cyan) indicates that B fluctuates little (B itself is also much smaller than $\langle A\rangle$). More importantly, the covariation of the mean flow and wave activity is quasi-periodic for this season and latitude. I will later address the timescale of covariation in Figure 3.5 below.

4. An earlier version of this material appeared in *Wang and Nakamura* [2015]. ©American Geophysical Union. Used with permission.

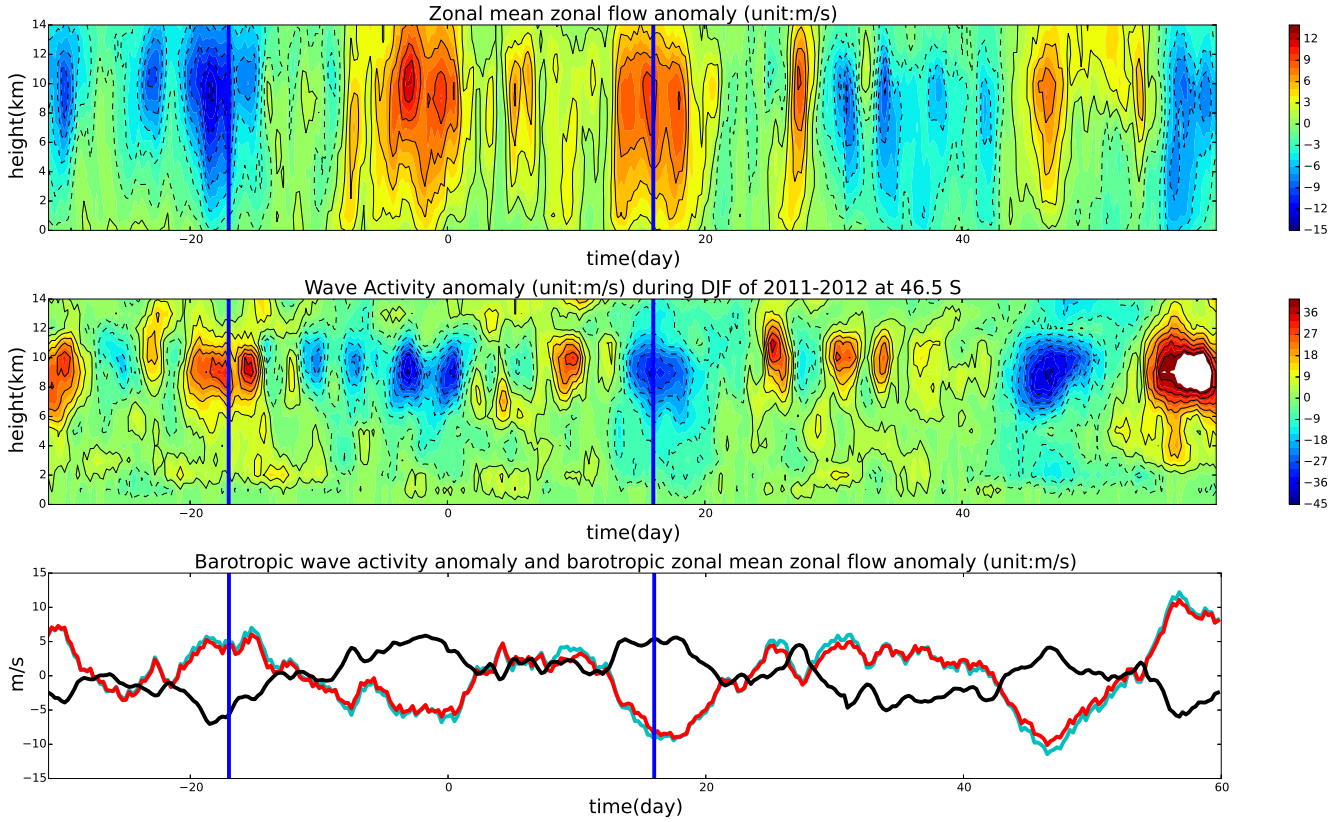

Figure 3.1: Top two panels show time-height cross sections of zonal-mean zonal wind anomaly (departure from seasonal mean values) $\Delta\bar{u}$ and wave activity anomaly ΔA at 46.5 S for December 2011 - February 2012. (0 in the horizontal axis corresponds to 1 January 2012.) Contour intervals are 2 ms^{-1} ($\Delta\bar{u}$) and 6 ms^{-1} (ΔA) with negative values dashed. The third panel shows anomalies in barotropic zonal-mean zonal wind $\Delta\langle\bar{u}\rangle$ (black) and barotropic wave activity $\Delta(\langle A\rangle + B)$ (red) and $\Delta\langle A\rangle$ (cyan). Two blue vertical lines in each panel refer to the low and high index cases to be described in Figure 3.3. The same instances are also sampled in Figures 1.2 and 1.3. Based on the ERA-Interim reanalysis. See text for details. (appeared in *Wang and Nakamura* [2015]. ©American Geophysical Union. Used with permission.)

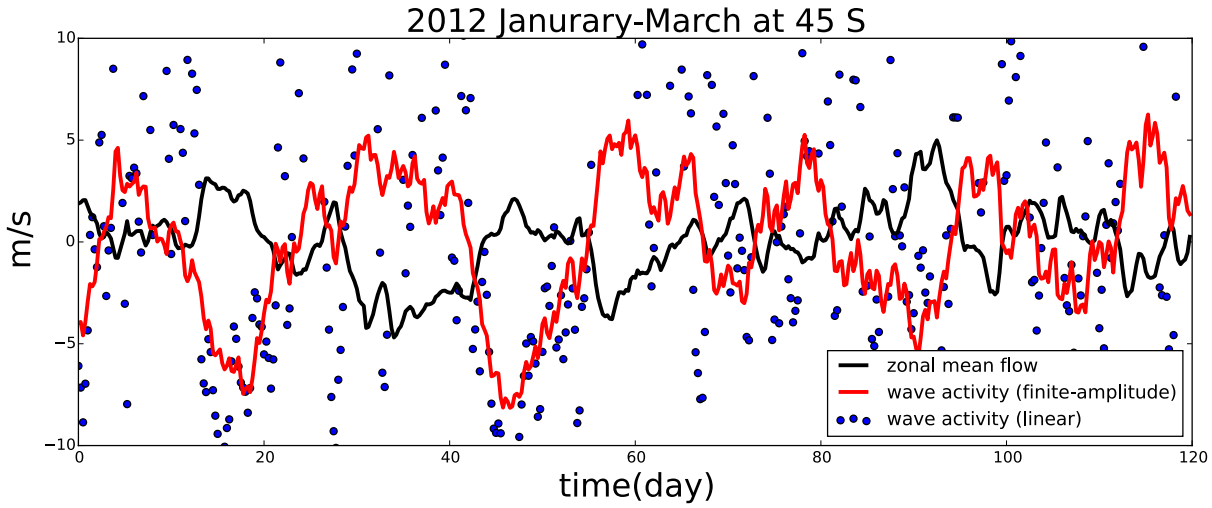

Figure 3.2: A comparison between density-weighted linear wave activity (blue dots) and finite-amplitude wave activity (red curve), and the zonal-mean zonal flow (black curve). Analysis is shown for the period between January 1, 2012 - April 30, 2012 and is based on ERA-Interim products.

It is stressed that the use of FAWA is essential for this budget analysis. Figure 3.2 is similar to the bottom panel of Figure 3.1 but for a slightly different latitude (45 S) and period (January-April 2012). The figure also shows the linear wave activity A_{lin} given by equation (2.4) in dots. Because of large variation in the zonal-mean QGPV gradient, A_{lin} undergoes a much greater variability than FAWA.

Figure 3.3 delineates hemispheric atmospheric flows during a period in which wave activity is high and the mean flow is weak (top panels) and another period in which the opposite is true (bottom panels). These instances correspond to the two blue vertical lines in Figure 3.1. In the former (Dec. 15, 2011) the 250 hPa geopotential reveals a highly meandering westerly flow in the mid-latitudes and the core of the jet is split into polar and subtropical latitudes, with westerly winds significantly weakened around 45-55 S. In the latter (Jan. 16, 2012) eddies are relatively weak and the jet exhibits a single, enhanced core around 50 S. The two states exemplify the opposing phases of mid-latitude eddy-

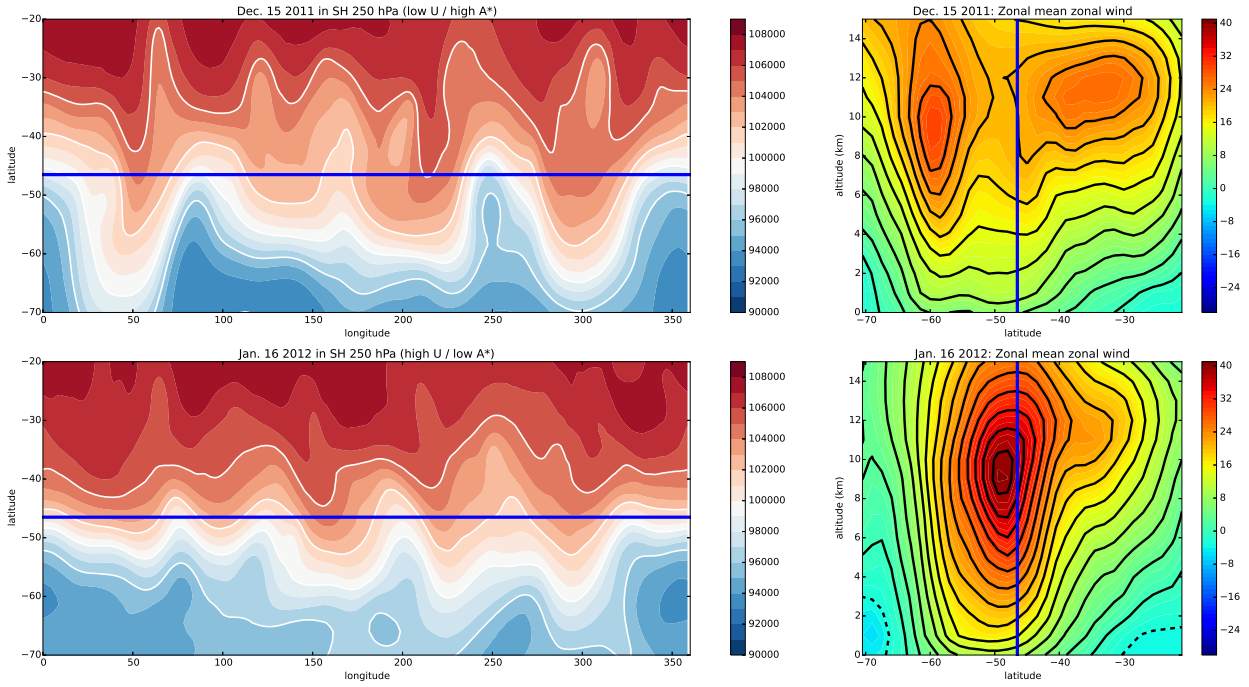

Figure 3.3: Upper panels: 250 hPa geopotential field (left) and vertical structure of zonal mean zonal wind (right) on 1800 UTC Dec. 15, 2011. Lower panels: same as upper panels but for 1800 UTC Jan. 16, 2012. White contours in the left panels are 99000, 102000, 105000 $m^2 s^{-2}$. Contour interval for the right panels is 3 ms^{-1} with negative values dashed. Blue lines indicate 46.5 S, the latitude of analysis for Figure 3.1. At the altitude of 250 hPa ($z \sim 9.7$ km), winds are approximately in geostrophic balance and blow parallel to the wavy contours of geopotential in the left column. (appeared in *Wang and Nakamura* [2015]. ©American Geophysical Union. Used with permission.)

mean flow vacillation captured by the covariation of the barotropic wave activity and the barotropic zonal-mean zonal wind in the bottom panel of Figure 3.1.

Figure 3.4 summarizes the covariation of the barotropic zonal-mean flow and FAWA at 46.5 S for the months of December through February over 35 years (1979-2013) in scatter diagrams. In all panels the horizontal axis is $\Delta\langle\bar{u}\rangle$. The vertical axes are $\Delta\langle A\rangle$ (left), ΔB (middle), and their sum (right). Each dot represents 6-hourly data. In the upper panels anomalies are defined as departures from the mean seasonal cycle. $\Delta\langle A\rangle$ displays a robust anticorrelation with $\Delta\langle\bar{u}\rangle$. While the data points cluster around a line, its slope is clearly steeper than -1, meaning that $\langle A\rangle$ varies more than $\langle\bar{u}\rangle$. The surface wave activity anomaly, ΔB, on the other hand, shows a positive correlation with $\Delta\langle\bar{u}\rangle$

because the sign of B is opposite of $\langle A \rangle$'s. However the very gentle slope suggests that B only slightly offsets $\langle A \rangle$, consistent with the bottom panel of Figure 3.1. As a result, ($\Delta \langle \bar{u} \rangle$, $\Delta(\langle A \rangle + B)$) clusters around an axis whose slope is slightly closer to -1 (indicated by the solid red line in the right panel) but still significantly steeper. Since equation (2.26) would place the data points exactly on the red line, the scatter and deviation from the -1 slope suggest that effects of nonconservative processes are significant. Nevertheless, the strong anticorrelation between the barotropic flow and wave activity reveals a largely adiabatic nature of the mid-latitude eddy-mean flow interaction during the austral summer. In the lower panels, anomalies are defined as departures from the 3-day running mean. These high-frequency transients in FAWA and the mean flow exhibit much smaller variance (note different scales of the axes) but a slope closer to -1 (lower right panel). Notice that the change in the slope is more notable in the left panel than in the middle, suggesting that the nonconservative term $\left\langle \dot{A} \right\rangle$ in equation (2.25) is relatively small at high frequencies but $\dot{B}$ is not.

The top two panels of Figure 3.5 show power spectra of $\langle \bar{u} \rangle$ and $\langle A \rangle + B$ as functions of frequency and latitude for four months of austral summer (December-March). The spectrum of $\langle \bar{u} \rangle$ is strongest at low frequency (less than 0.02 CPD) and at the flanks of the jet but minimal near the jet axis ($\sim$ 48 S), very similar to the analysis of the surface wind spectra based on the remote sensing data in Figure 1.4 (top left). This is consistent with our current understanding of the Southern Annular Mode (SAM) [*Hartmann and Lo*, 1998; *Lorenz and Hartmann*, 2001; *Gerber et al.*, 2008]: the leading variability of the zonal-mean zonal wind is a slow meridional fluctuation of the jet axis. The persistency of the SAM at low frequency is believed to result from a 'positive eddy feedback,' [*Feldstein and Lee*, 1998; *Robinson*, 2000; *Lorenz and Hartmann*, 2001; *Zurita-Gotor et al.*, 2013; *Nie et al.*, 2014].

The power spectrum of FAWA is quite distinct, however. Although low frequency peaks do appear at the flanks of the jet, FAWA is marked by a very robust periodicity

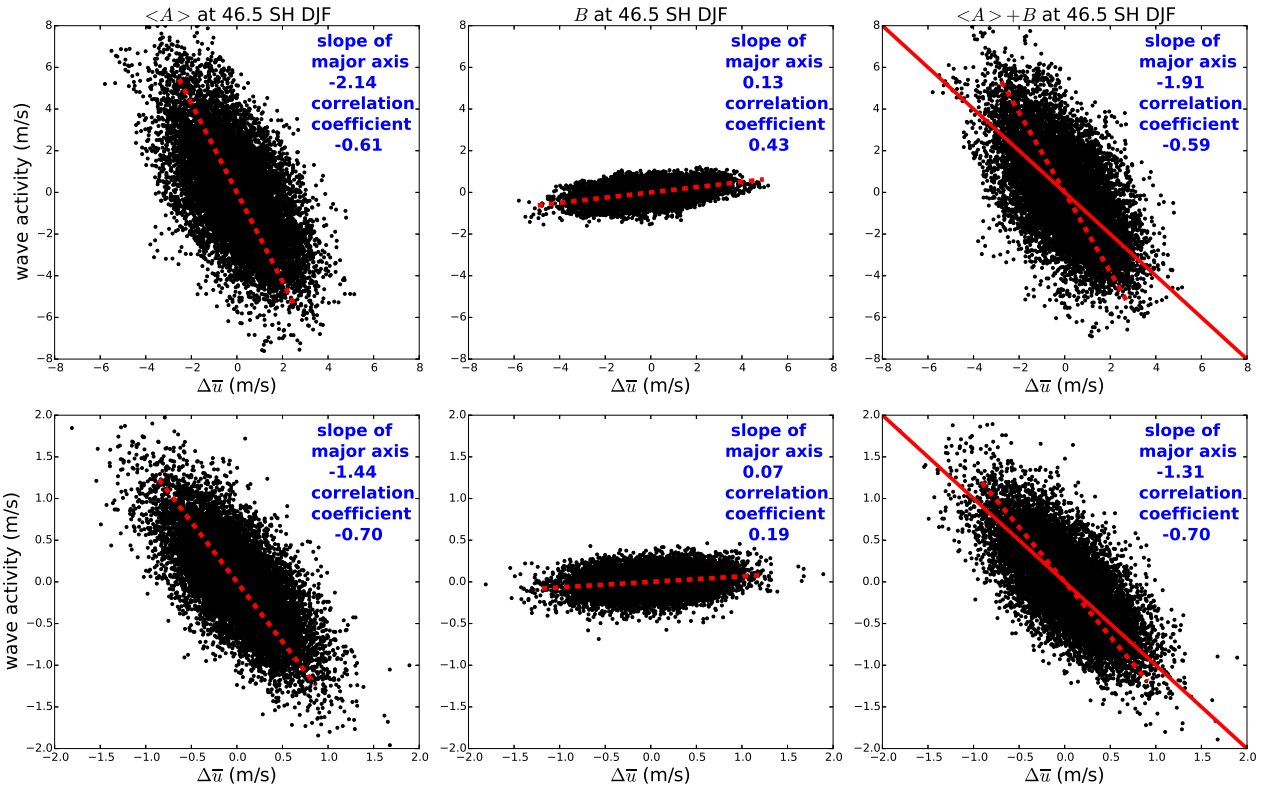

Figure 3.4: Covariation of wave activity and the zonal-mean zonal wind at 46.5 S for the months of December-January-February. The horizontal axes are the anomalies of $\langle \bar{u} \rangle$. The vertical axes are the anomalies of $\langle A \rangle$ (left panels), B (middle panels) and $\langle A \rangle + B$ (right panels). Upper panels: anomalies are defined as departures from the mean seasonal cycle. Lower panels: anomalies are defined as departures from the 3-day running mean. Note the different scale and range of axes between the upper and the lower panels. The solid red lines in the right panels indicate the slope of -1. The dashed lines show the orientation of the major axis of the fitted ellipsoid, computed from the covariance matrix. The slopes of the major axes and the correlation coefficients are indicated in each panel. The major axis of the ellipsoid is essentially the principle component of EOF. Based on ERA-Interim 6 hourly data for 1979-2013. (appeared in *Wang and Nakamura* [2015]. ©American Geophysical Union. Used with permission.)

around 0.03-0.05 CPD (20-30 days) between 40 S and 55 S. This corresponds to the BAM found in the leading pattern of eddy kinetic energy [*Thompson and Woodworth*, 2014; *Thompson and Barnes*, 2014] and here a peak power appears at the period of 25 days. Similar spectra are found for the surface EKE based on the remote sensing data in Figure 1.4 (second left). A corresponding peak is not visible in the spectrum of the zonal-mean wind (Figure 3.5 top panel), but their cospectrum (the amplitude of the real part of the complex cross-spectrum), a measure of the shared variance between FAWA and the mean flow, shows a peak at 0.04 CPD near the jet axis (third panel). Coherence-squrared spectrum (bottom panel), very similar to the square of correlation coefficient, clearly identifies an enhanced correlation between FAWA and the zonal-mean wind between 42 - 52 S and 0.04 - 0.07 CPD (BAM) in addition to the low frequency peaks at the flanks of the jet (SAM). It also increases significantly at high frequency, consistent with Figure 3.4. (The improvement of correlation at high frequency is not captured by the cospectrum because the variances of $\langle \bar{u} \rangle$ and $\langle A \rangle + B$ both decrease as frequency increases.)

3.2.2 Eddy forcing spectra in austral summer

To understand the distinct spectra for $\langle \bar{u} \rangle$ and $\langle A \rangle + B$ in the mid-latitudes, I show in Figure 3.6 power spectra of the tendency and flux terms in equations (2.21), (2.23), and (2.24) at 46.5 S for the same period as Figure 3.5. The top left panel shows the power spectra of the first two terms on the right-hand side of equation (2.21) and of their sum. The convergence of the vertically integrated momentum flux (blue) has a generally broad spectrum that peaks around 0.15 CPD ($\sim$ 7 days) although the spectrum also contains some small peaks. The meridional eddy heat flux contribution (red) has a distinctive peak around 0.04 CPD ($\sim$ 25 days), at which the power is nearly twice as large as that of the momentum flux convergence. Crossover of the two spectra occurs around 0.06 CPD ($\sim$ 17 days). Thus the predominant contribution to the total eddy forcing (the vertically integrated PV flux, magenta) comes from the former in the high frequency range and from the latter

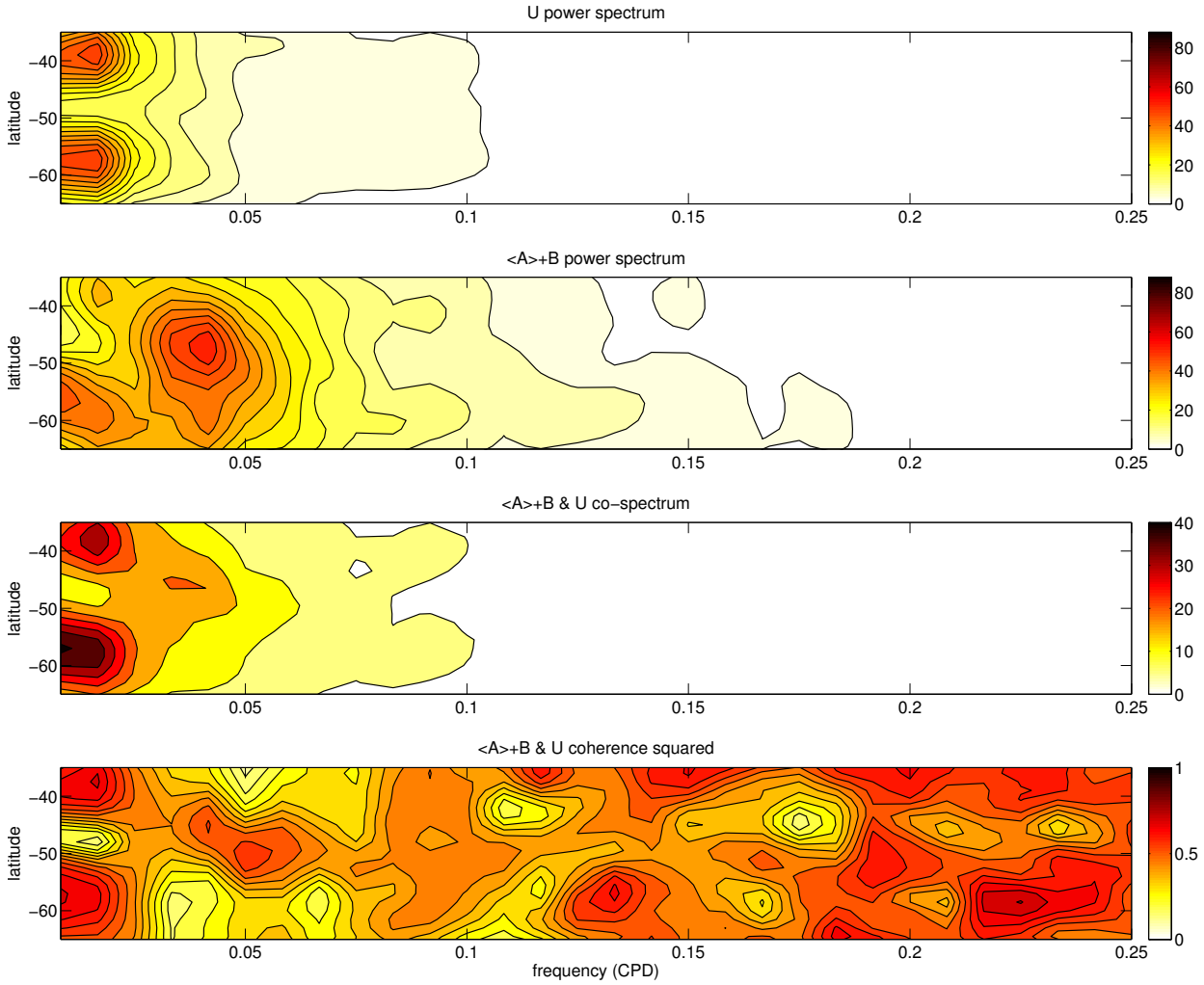

Figure 3.5: Spectral analysis for 4 austral summer months (December-March) as functions of frequency (0.0167 - 0.25 CPD) and latitude (35° – 65°S). Top: power spectrum for $\langle \bar{u} \rangle$. Contour interval is 4 m^2. Second from top: same as top but for $\langle A \rangle + B$. Third: cospectra of $\langle \bar{u} \rangle$ and $\langle A \rangle + B$. Contour interval is 2 m^2. Bottom: same as third but for coherence squared. Contour interval is 0.05. Zero contours are highlighted in white. Based on the ERA-Interim reanalsis (1979-2013). (appeared in *Wang and Nakamura* [2015]. ©American Geophysical Union. Used with permission.)

in the low frequency range. The top right panel compares the spectra of the same momentum flux convergence (blue) and the tendency of barotropic flow (black). The two spectra share similar shapes but the latter has significantly lower power at frequencies lower than 0.25 CPD (>4 days), suggesting the increasing role of friction represented by $\left\langle \dot{U} \right\rangle$ in equation (2.24). The bottom left compares the spectra of the low-level meridional eddy heat flux term and of the tendency of surface wave activity. At low frequency the former utterly dominates the latter, suggesting that the predominant balance in equation (2.21) is between the two right-hand side terms:

$$\frac{1}{H}\left(\frac{f\overline{v'\theta'}}{d\tilde{\theta}/dz}\right)_{z=0} \approx \dot{B} \approx -\frac{B}{\tau_H} > 0. \tag{3.1}$$

Notice that, since $B \leq 0$, a positive $\dot{B}$ corresponds to a damping of surface wave activity. Also, since both B and the meridional eddy heat flux term have the surface static stability in the denominator, the ratio of the tendency and flux terms is unaffected by the uncertainty in the surface static stability. If the left-hand side of equation (3.1) is modeled as linear damping of B, the average damping time τ_H is found to be about 0.9 day, close to the damping time of surface temperature estimated by *Swanson and Pierrehumbert* [1997] over the Pacific storm track (1 day) using Lagrangian tracer calculations. *Blanco-Fuentes and Zurita-Gotor* [2011] also demonstrate a strong influence of surface thermal damping in the low frequency variability of baroclinicity in the SH mid-latitudes. Then by adding equations (2.21) and (2.23) and using equation (3.1), one obtains

$$\frac{\partial}{\partial t}(\langle A \rangle + B) \approx \frac{1}{a\cos^2\phi}\frac{\partial}{\partial \phi}\left\langle \overline{u'v'}\cos^2\phi \right\rangle + \left.\frac{f\overline{v'\theta'}}{H(\partial\tilde{\theta}/\partial z)}\right|_{z=0} + \left\langle \dot{A} \right\rangle. \tag{3.2}$$

The bottom right panel of Figure 3.6 compares the spectra of this tendency term and the sum of the first two terms on the right-hand side. The two spectra agree well except for 0.05-0.3 CPD (3-20 days) and below 0.03 CPD (> 30 days), where the tendency has smaller power than the eddy forcing due to $\left\langle \dot{A} \right\rangle$. The source of the discrepancy below

0.03 CPD is believed to be radiative damping of FAWA whose timescale in the troposphere is several weeks, whereas at 0.05-0.3 CPD it is more likely due to mixing driven by large-scale circulation. Compared to the tendency of $\langle \bar{u} \rangle$ in the top right panel, the wave activity tendency has more power at low frequencies due to the additional heat flux contribution [compare equation (3.2) with (2.24); also compare the solid and dashed black curves in the top right panel in Figure 3.6]. This explains the generally lower power and the lack of peak around 0.04 CPD in the spectrum of the zonal-mean zonal wind at this latitude as seen in Figure 3.5. This is also likely the main cause of the scatter and departure from the -1 slope in the third panel of Figure 3.4: since the greater tendency of FAWA in the frequency range of BAM translates to a greater variance of FAWA than the zonal-mean flow, the $\Delta \langle \bar{u} \rangle - \Delta \langle A \rangle$ slope becomes steeper than -1.

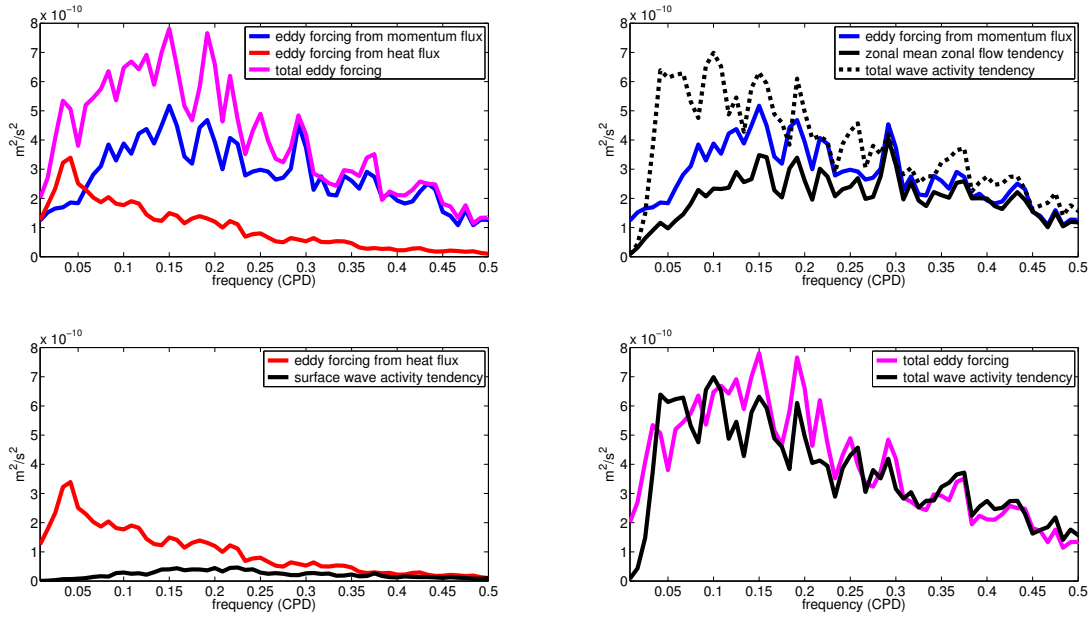

Figure 3.6: Top left: power spectra of total eddy forcing (vertically integrated PV flux, magenta) and contributions from eddy momentum flux convergence (blue) and low-level meridional eddy heat flux (red). Top right: power spectra of eddy momentum flux convergence (blue), the zonal-mean zonal flow tendency $\omega\hat{\bar{u}}(\omega)$ (black), and total wave activity tendency $\omega(\langle\hat{A}\rangle(\omega)+\hat{B}(\omega))$ (dashed black). Lower left: power spectra of eddy forcing from low-level meridional heat flux (red) and surface wave activity tendency $\omega\hat{B}(\omega)$ (black). Lower right: power spectra of total eddy forcing (magenta) and total wave activity tendency (black). Analysis is performed at 46.5 S for the same period as Figure 3.5. See text for details. (appeared in *Wang and Nakamura* [2015]. ©American Geophysical Union. Used with permission.)

3.3 Seasonality

In the previous section, I formulated eddy-mean flow interaction in terms of latitude-by-latitude, vertically integrated budgets of finite-amplitude wave activity (FAWA) [*Nakamura and Zhu*, 2010] and the zonal-mean zonal wind. When I applied it to the austral summer with the ERA-Interim reanalysis product, a pronounced antiphase covariation of FAWA and the zonal-mean zonal wind was found between 40 and 55 S (Figure 3.5 bottom). While such covariation is expected from the nonacceleration relation under adiabatic and frictionless dynamics (*Charney and Drazin* [1961] and equation (2.26) above), the austral summer stands out in that the covariation appears quasi-periodic with a timescale much longer than the typical lifespan of synoptic eddies (see Figure 3.1). It was shown that the FAWA power spectra exhibit a distinctive peak around 25 days (~ 0.04 CPD) between 40 and 55 S (Figure 3.5 second panel), although the corresponding spectra of the zonal-mean zonal wind are red and dominated by variabilities at the flanks of the storm track latitudes. That the foregoing analysis (particularly the spectra) is consistent with the remote sensing of surface variables in Chapter 1 shows that the periodicity involves the eddy-mean flow interaction of the entire troposphere of austral mid-latitudes. However, in the remote sensing data there is significant seasonal variation (Figure 1.4). I shall therefore examine the seasonal variation in the FAWA budgets next, in the hope that it will provide a clue for the driver of the periodic behavior in the austral summer [5] .

3.3.1 FAWA and EKE

As explained in the previous section, the predominant 20-30 day periodicity in FAWA during the austral summer is consistent with the recently identified baroclinic annular mode (BAM) in eddy kinetic energy (EKE) [*Thompson and Woodworth*, 2014; *Thompson and Barnes*, 2014] (hereafter as TW14 and TB14, respectively).

5. An earlier version of this material appeared in *Wang and Nakamura* [2016]. ©American Meteorological Society. Used with permission.

Thompson and the collaborators find that the periodicity in EKE is associated with the low-level meridional eddy heat flux, which shows a well-defined spectral peak around 20-30 days during the austral summer (as I also find; Figures 3.6 and 3.7). A similar analysis for the Northern Hemisphere shows that the spectral peak in EKE and the low-level heat flux is more robust in summer [*Thompson and Li*, 2015] (hereafter TL14). While TW14, TB14 and TL14 all use the leading EOF of the zonally averaged EKE to define the BAM, I choose to work with FAWA partly because it possesses (unlike EKE) a closed latitude-by-latitude budget, and partly because it has a direct theoretical connection with the low-level meridional eddy heat flux [equation (2.23)]. Despite the difference in the conservation properties, the vertically integrated FAWA and the zonally averaged EKE at 300 hPa both display a qualitatively similar spectra in the frequency-latitude space for the austral summer (Figures 3.7a and 3.7b): they both exhibit a distinctive spectral peak centered around 47 S and 0.04 CPD, which coincides with the spectral peak in the low-level meridional eddy heat flux (Figure 3.7c).

When the analysis is repeated for the austral winter, the picture changes significantly. Figures 3.7d-3.7f show the corresponding quantities for the months of June-September. FAWA no longer possesses a compact spectral peak in the extratropics and instead exhibits multiple peaks, including two strong ones at high latitudes (60-65 S) and a secondary maximum at a slightly higher frequency ($\sim$ 0.06 CPD) at lower latitudes ($\sim$ 40 S) (Figure 3.7d).

The EKE spectra are appreciably different from FAWA: they are split into multiple peaks over a wide latitudinal range with the strongest power appearing around 35 - 40 S and at lower frequencies (0.02-0.03 CPD) (Figure 3.7e). Meanwhile, the spectra of the low-level meridional eddy heat flux are dominated by large values in high latitudes at higher frequencies (0.05-0.1 CPD) (Figure 3.7f). Therefore, unlike summer, spectra of FAWA, EKE and eddy heat flux appear quite disparate. As shown in Appendix 3.A, the leading EOF of EKE is qualitatively similar between the two seasons, but it explains sub-

stantially less variance in winter than in summer (30 versus 45 percent) and its peak frequency is less separated from the seasonal timescale. Clearly, the structure of eddy spectra and the underlying dynamics are more complex in winter, and the BAM's periodicity is harder to detect in raw data.

To further elucidate the similarity and differences between FAWA and EKE as a diagnostic, I show in Figure 3.8 the time-latitude plots of the anomalies in the vertically integrated FAWA (Figure 3.8a) and the zonally averaged EKE at 300 hPa (Figure 3.8b) for the year 2012. The two show similar patterns but there are appreciable differences during winter months (days 150-300): for example, some large wave activity events in high latitudes are missing in EKE. Figure 3.8c shows the part of the EKE anomaly explained by the leading EOF (BAM), and its amplitude (the BAM index, TW14, normalized to a unit variance) is shown as the blue curve in Figure 3.8d. Also shown in Figure 3.8d is the volume integral of FAWA between 20 and 70 S [see equation (2.27)] (red curve), again normalized to a unit variance. The domain-integrated FAWA correlates with the BAM index remarkably well (r = 0.72). I thus argue that, despite the difference in their latitudinal structures, both diagnostics capture the same low frequency variability of the eddy amplitude when integrated over the extratropics.

3.3.2 Eddy forcing spectra

In section 3.2.2, I compared the magnitude of the terms in equations (2.21), (2.23), and (2.24) for the austral summer storm track. It is found that the left-hand side of equation (2.21) is negligible compared to the right-hand side terms and that B is small compared to $\langle A \rangle$. Then assuming that $\dot{B}$ represents thermal damping of B due to exchange of heat with the underlying surface, I derived (3.1) and estimated $\tau_H \sim 0.9$ day in the BAM-related latitudes, close to ~ 1 day found by *Swanson and Pierrehumbert* [1997] as the thermal damping timescale of surface temperature in the Pacific storm track using Lagrangian tracer calculations.

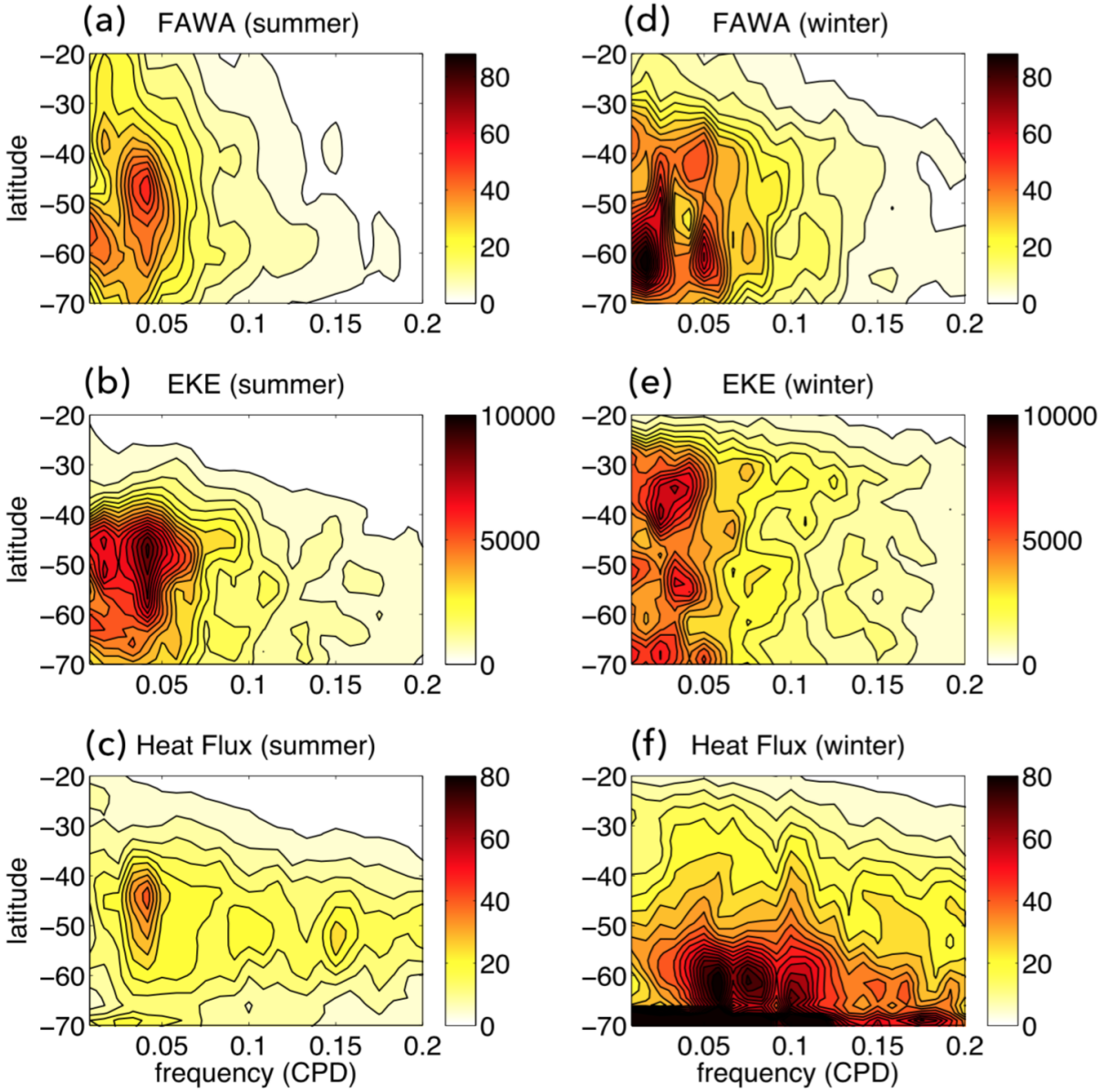

Figure 3.7: Power spectra of eddy properties as functions of frequency and latitude. Top row [(a),(d)]: total wave activity $\langle A \rangle + B$. See WN15 and section 2 for the definition of wave activity. Contour interval is 4 m^2. Second row [(b), (e)]: eddy kinetic energy at 300 hPa. Contour interval is 500 $m^4 s^{-2}$. Bottom row [(c), (f)]: meridional eddy heat flux $\overline{v'\theta'}$ at 850 hPa. Contour interval is 4 $K^2 m^2$. Left column [(a)-(c)]: December-March. Right column [(d)-(f)]: June-September. Based on the ERA-Interim reanalysis 1.5° × 1.5° gridded data (Dee et al. 2011) for 1979-2014. (appeared in *Wang and Nakamura* [2016]. ©American Meteorological Society. Used with permission.)

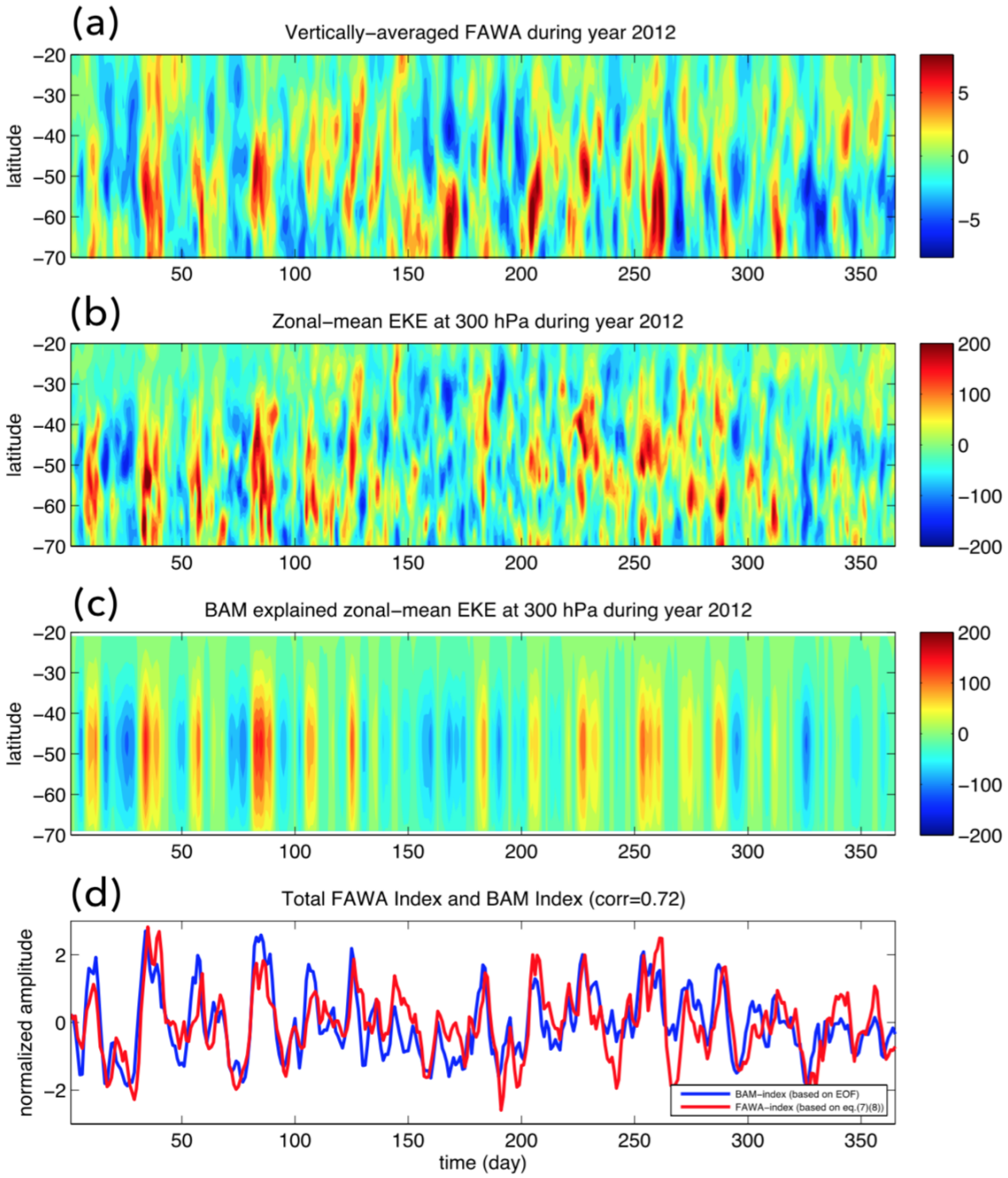

Figure 3.8: (a) Anomaly (departure from the annual mean) of the vertically averaged wave activity $\langle A \rangle + B$ as a function of time and latitude for the year 2012. (b) Same as (a) but for the 300 hPa zonal-mean EKE. (c) Same as (b) but for the part of the EKE anomaly 'explained' by the first EOF. (d) The BAM index (regression on the first EOF of the zonal-mean 300 hPa EKE anomaly, blue), and the volume integral of wave activity between 20° S and 70° S (red). Both curves are normalized to the unit variance. Based on the ERA-Interim reanalysis (1979-2014). (appeared in *Wang and Nakamura* [2016]. ©American Meteorological Society. Used with permission.)

Since the tendency of B is negligible, covariation of FAWA and the zonal-mean flow is dictated by equations (2.23) and (2.24). It was found that at high frequencies (> 0.1 CPD) $\langle \bar{u} \rangle$ and $\langle A \rangle$ are both primarily driven by the eddy momentum flux term, whereas the eddy heat flux forcing near the surface has a peak power around the BAM frequency ($\sim$ 0.04 CPD) at which it dominates the eddy momentum flux forcing in equation (2.23) (Figure 3.6). This last result is reproduced in the bottom panel of Figure 3.9a, which shows the power spectra of the first two right-hand side terms of (2.23) at 46.5 S for the warm season. The 0.04 CPD spectral peak in the red curve drives the BAM through the second term on the right-hand side of (2.23).

The bottom panel of Figure 3.9b shows the same quantities for the cold season. In winter at 46.5°S, the eddy heat flux spectrum is more red-noise-like and lacks a clear peak, and is comparable to the eddy momentum flux forcing only in the low frequency limit. I have repeated the analysis at other latitudes - for example at 40°S at which FAWA maximizes in winter - and found that the results are qualitatively similar. Figure 3.9 also depicts the vertical structure of the power spectrum of the density-weighted eddy momentum flux convergence (top) and the scaled eddy heat flux (middle) at the same latitude.

In both seasons the density-weighted eddy momentum flux convergence is concentrated in the upper troposphere (see a recent discussion in *Ait-Chaalal and Schneider* [2014]), although in winter the magnitude is significantly greater. The eddy momentum flux convergence spectra are marked by a few distinct peaks in frequency but otherwise broad (Figure 3.9, top panels). In contrast, the spectra of density-weighted eddy heat flux occupy mostly the middle- to lower troposphere (Figure 3.9, middle panels). Even though the spectral peak at $\sim$ 0.04 CPD in the bottom panel of Figure 3.9a pertains to the near-surface eddy heat flux (2.23), this spectral peak in eddy heat flux extends vertically up to $\sim$ 8 km, suggesting that the 20-30 day periodicity in the eddy heat flux is present through the entire troposphere (Figure 3.9a middle panel). Although in both seasons the eddy

heat flux and its contribution to the eddy PV flux are more confined to low frequency (< 0.25 CPD) than the eddy momentum flux contribution, the 0.04 CPD peak in the eddy heat flux clearly distinguishes the two spectra from each other in the austral summer.

The 20-30 day cycle in the low-level eddy heat flux means that, through equation (3.1), $\dot{B}$ should also exhibit similar periodicity. This is corroborated by the recent work by *Herman* [2015] who shows that atmosphere-ocean turbulent heat exchange (which represents $\dot{B}$) varies strongly on the timescale of the BAM in the austral summer. However this is not an intrinsic timescale of air-sea heat exchange, which is driven by large-scale dynamics of the atmosphere and slaved to its meridional eddy heat flux, not the other way round. On the other hand, air-sea heat exchange does provide a rapid thermal damping to the atmosphere immediately above sea surface, which keeps the surface wave activity consistently weak: $0 < -B \ll \langle A \rangle$. This makes it difficult to interpret the BAM variation of $\langle A \rangle$ in terms of the traditional baroclinic lifecycles, in which B would also undergo a comparable variation (and sign changes).

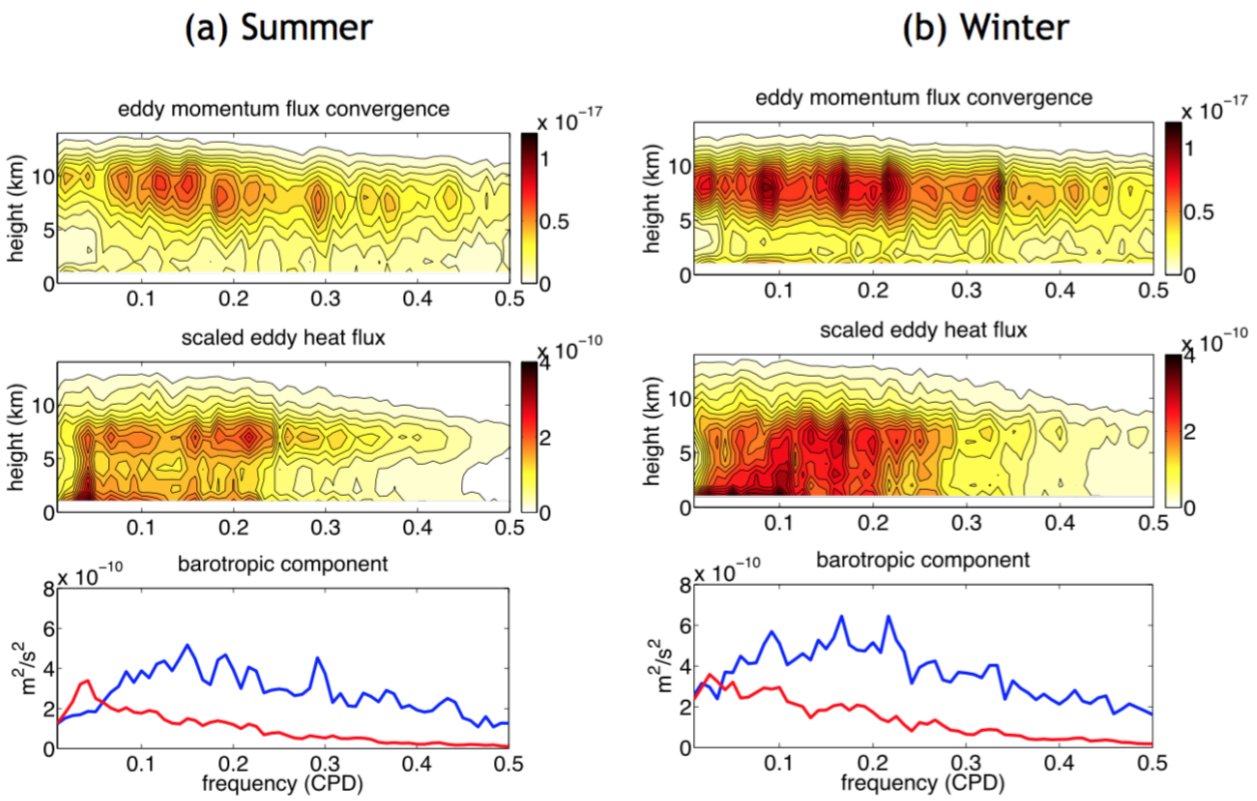

Figure 3.9: Power spectra of the eddy fluxes at 46.5°S. Top: convergence of eddy momentum flux density $(\tilde{H}a\cos^2\phi)^{-1}\partial(e^{-z/H}\overline{u'v'}\cos^2\phi)/\partial\phi$, where ϕ is the radius of the Earth, ϕ is latitude, $H = 7\,km$ and $\tilde{H} \equiv \sum_{n=1}^{n=49} e^{-n\Delta z/H}\Delta z = 6.5\,km$ (n indicates the vertical levels of analysis and $\Delta z = 1$ km.) Contour interval: $6.0\times10^{-19}s^{-2}$. Middle: scaled eddy heat flux density $(f\tilde{H}^{-1})(e^{-z/H}\overline{v'\theta'})(d\tilde{\theta}/dz)^{-1}$, where the Coriolis parameter is evaluated at 46.5°S. Contour interval: $2.0\times10^{-11}m^2s^{-2}$. Bottom: Red curve: the eddy heat flux contribution to the barotropic component of the eddy PV flux. Blue curve: the eddy vorticity flux contribution to the barotropic component of the eddy PV flux. The vertical integral of the top panels corresponds to the blue curves in the bottom panels, whereas the values of the middle panels at z = 0.5 km correspond to the red curves. Left: December-March. Right: June-September. The range of frequency shown is 0.0167-0.5 CPD. See text for details. (appeared in *Wang and Nakamura* [2016]. ©American Meteorological Society. Used with permission.)

3.3.3 *Zonal-mean background state*

To understand the seasonality of the eddy fluxes in Figure 3.9, particularly the low frequency peak in the eddy heat flux that only occurs in the warm season, I explore the role of the zonal-mean state in shaping the eddy flux spectra. To the extent that the large-scale eddies in the SH storm track obey the quasigeostrophic dynamics, the zonal-mean zonal winds and the meridional gradients of the zonal-mean QGPV in the interior and of the zonal-mean potential temperature near the surface are of particular interest.

Figure 3.10 shows the meridional cross sections of the zonal-mean zonal wind and potential temperature (top), zonal-mean QGPV gradient (middle), and the eddy heat flux (bottom) for the warm and cold seasons of the Southern Hemisphere. The zonal-mean zonal wind captures the well-known regime transition between the extratropical ('merged') jet in summer (top left) to the subtropical jet in winter (top right) [*Lee and Kim*, 2003; *Lachmy and Harnik*, 2014]. Corresponding to this, the PV gradient exhibits significant seasonality near the tropopause. In the austral summer, the PV gradient is concentrated in a narrow latitude band slightly poleward of the jet axis (middle left). In the austral winter, the tropopause-level PV gradient spreads over two maxima: one in the subtropics and the other in the mid-latitude, the former being the strongest. A negative flow curvature near the jet axis generally enhances the PV gradient but the variation in the vertical shear is found to contribute strongly to the PV gradient in the austral summer (not shown). In addition, strong PV gradients appear in the lower troposphere around the edge of the Antarctica in the austral winter (middle right), a result of the vast thermal contrast between continental ice and relatively warm ocean surface.

The seasonal march of the meridional gradients of the tropopause-level PV and of the low-level (850 hPa) temperature is shown in Figure 3.11 as a function of time and latitude. In the warm season (the merged jet regime) the PV gradients maximize around $50-55°$S whereas in the cold season (the subtropical jet regime) a band of strong PV gradients also appears around 30°S (top). The low-level temperature gradients maximize at $45-50°$S

in the warm season, whereas in the cold season they exhibit very large values around the edge of the Antarctica, surrounded by relatively uniform values in the extratropics (bottom).

The foregoing analysis reveals that in the austral summer, both the low-level baroclinicity and the tropopause-level PV gradients are meridionally confined to the mid-latitudes, whereas in the austral winter the two quantities are more meridionally spread and their maximum values do not align vertically. Thus during the austral summer, we can expect baroclinic eddies to be generated primarily in the meridionally narrow baroclinic zone in the mid-latitudes. Furthermore, a well-defined jet in the zonal-mean wind in the austral summer provides critical lines for the eddies on the flanks and thus hinders their radiation from the baroclinic zone. Thus the mid-latitudes of the austral summer become a zonal waveguide for the baroclinic eddies. Indeed, *Nakamura and Shimpo* [2004] show that the zonal component of the E-P flux is greatly enhanced during the austral summer. *Chang* [2005] demonstrates that in the austral summer synoptic waves can travel two entire global zonal circles. Consistent with this picture, the bottom panels of Figure 3.10 show that the poleward eddy heat flux in the austral summer is significant (magnitude greater than 10 mKs^{-1}) only within a narrow latitude band of 40 – 60°S in the troposphere. Whereas in the austral winter the same range of eddy heat flux is spread from 30°S poleward in the lower troposphere, with particularly large values appearing near the edge of the Antarctica. The structure of the eddy heat flux is also consistent with the wave activity and heat flux spectra in Figure 3.7. In summer both spectra are concentrated in the mid-latitude (Figures 3.7a and 3.7c), whereas in winter the greatest wave activity is found at latitudes closer to the Antarctica, although a secondary FAWA maximum appears around 40°S (Figures 3.7d and 3.7f).

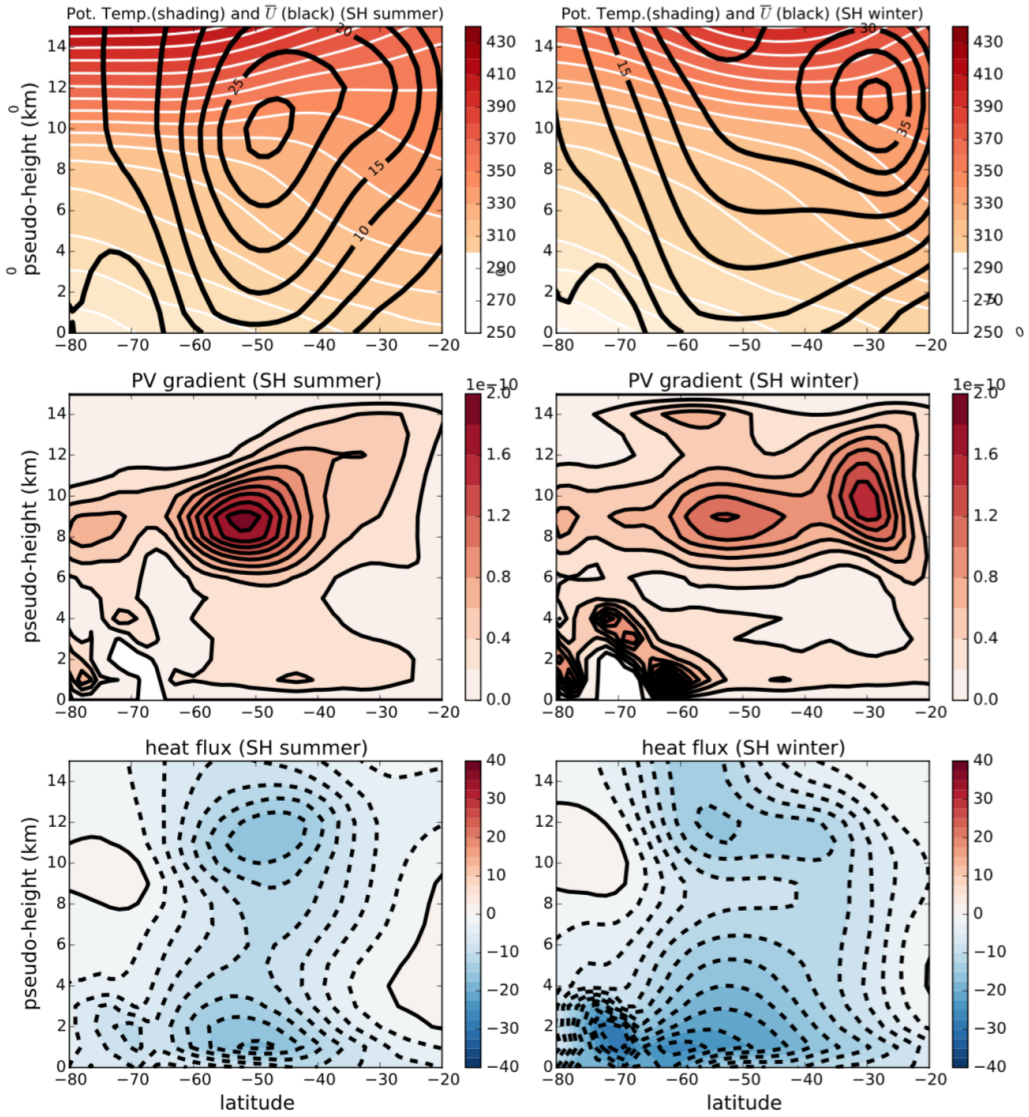

Figure 3.10: The Southern Hemisphere zonal-mean climatology for the December-March (left) and June-September (right). Top: $\{\bar{u}\}$ (black contours, contour interval: 5 ms^{-1}) and $\left\{\bar{\theta}\right\}$ (shading, contour interval: 10 K). Middle: meridional gradients of quasigeostrophic PV (contour interval: 2.0×10^{-11} $m^{-1}s^{-1}$). Bottom: eddy heat flux $\left\{\overline{v'T'}\right\}$(contour interval: 2.5 mKs^{-1}). Based on the ERA-Interim reanalysis 1979-2014. (appeared in *Wang and Nakamura* [2016]. ©American Meteorological Society. Used with permission.)

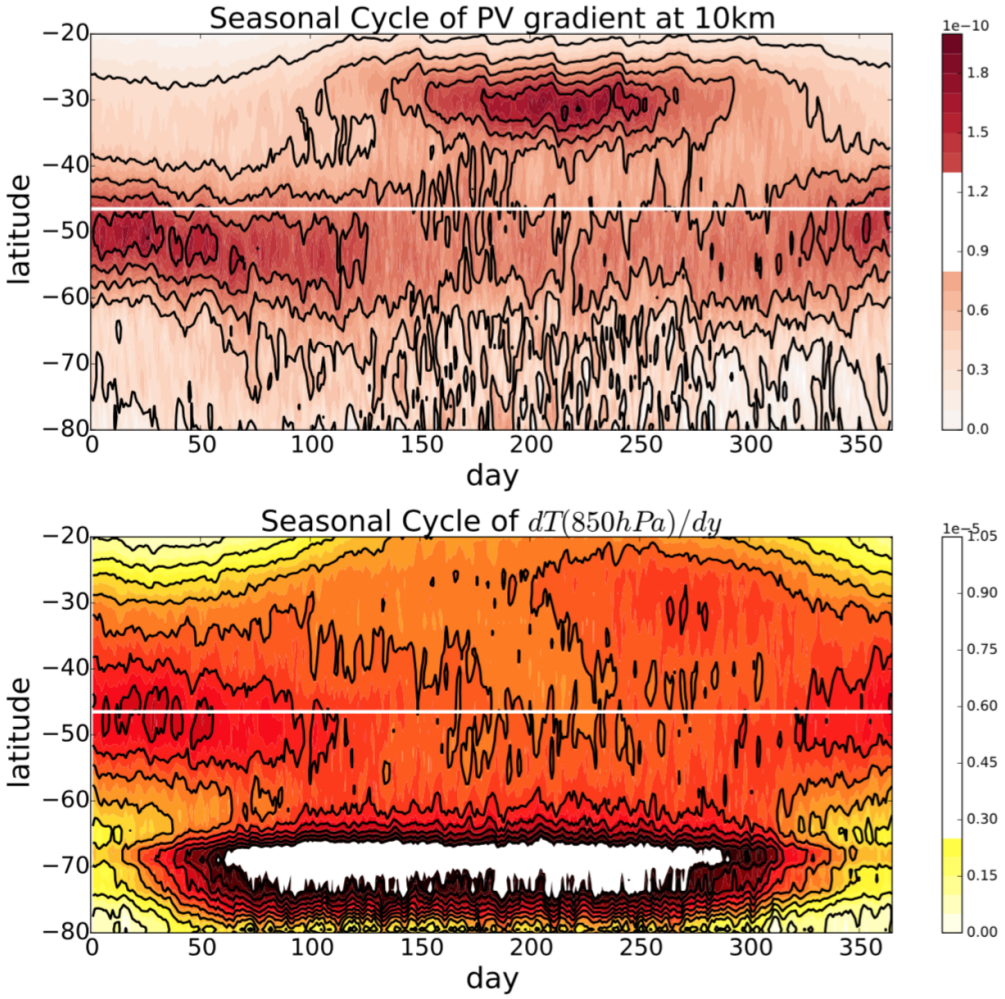

Figure 3.11: Top: Seasonal cycle of the meridional gradients of the zonal-mean quasi-geostrophic PV at the 10 km pressure pseudoheight (contour interval: $4.0\times10^{-11}m^{-1}s^{-1}$). Bottom: Seasonal cycle of the meridional gradients of the zonal-mean potential temperature gradient at 850 hPa (contour interval: $5\times10^{-7}Km^{-1}$). Average of 1979-2014 based on the ERA-Interim reanalysis, with a weak time filtering to suppress excessive noise. The white lines indicate 46.5°S. (appeared in *Wang and Nakamura* [2016]. ©American Meteorological Society. Used with permission.)

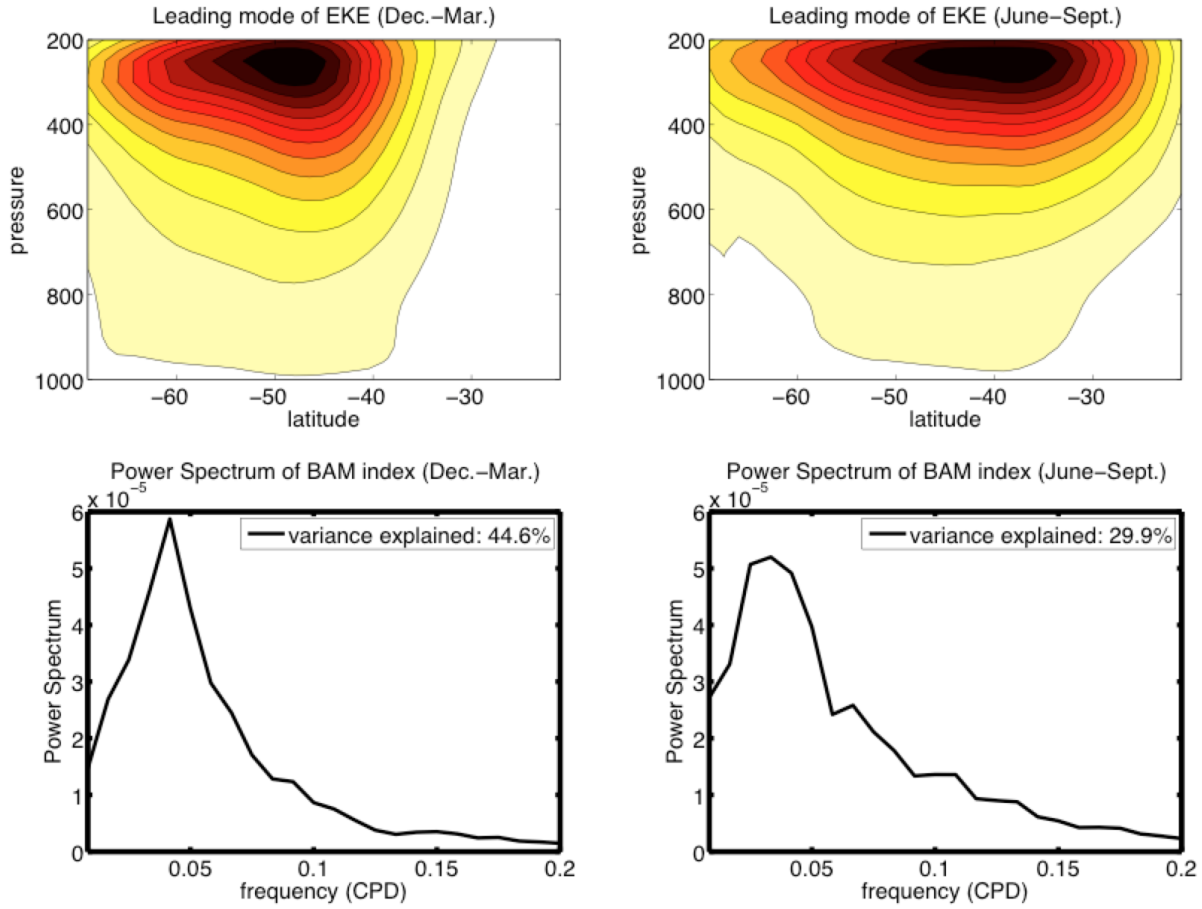

Figure 3.12: Top row: Leading EOF of the zonally averaged EKE anomaly. Bottom row: Power spectrum of the BAM index (expansion coefficient of the leading EOF) in the unit of $m^4 s^{-2}$. Left column: December-March. Right column: June-September. Based on the method outlined in TB14 with the 1979-2014 ERA Interim reanalysis. Note that in December-March, the leading EOF explains $\sim$ 45 percent of the variance, whereas in June-September it explains only 30 percent of the variance. (appeared in *Wang and Nakamura* [2016]. ©American Meteorological Society. Used with permission.)

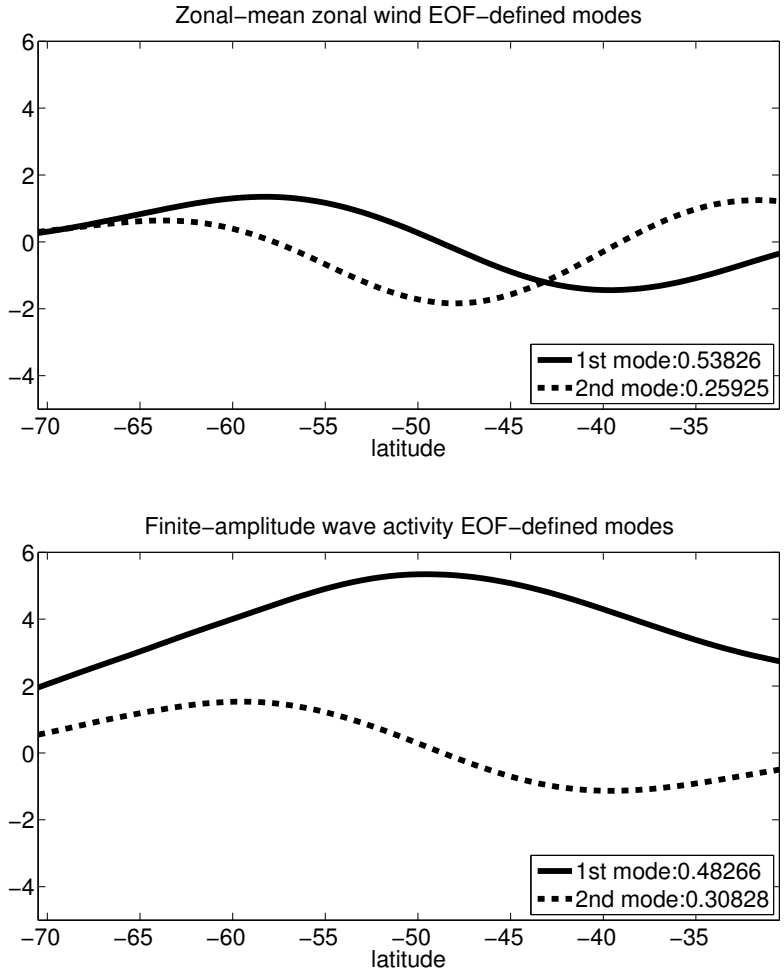

Figure 3.13: Leading modes of EOF for the barotropic component of the zonal-mean zonal wind $\langle \overline{u} \rangle$ (top) and for the barotropic component of FAWA $\langle A \rangle$ (bottom). Both results are with $\cos\phi$ weighting, where ϕ denotes the latitude. Based on the Appendix 3.B with the 1979-2014 ERA Interim reanalysis.

3.4 Short summary

I have formulated the mid-latitude eddy-mean flow interaction based on the latitude-by-latitude budget of barotropic FAWA, summarized in three coupled equations for the interior wave activity, surface wave activity, and zonal-mean zonal flow. Since the wave activity budget can be analyzed locally at each latitude, it complements the energy budget which requires the domain integral to close it. The analysis is also instantaneous and therefore deviates from the more traditional EOF approach [*Thompson and Wallace*, 2000; *Wallace*, 2000], which aims to extract patterns of flow variation from a hemispheric time series of data. That said, EOF can be applied to FAWA, just as it can be applied to EKE: see Appendix 3b.

Application to the mid-latitude austral summer revealed that:

- first-order dynamics of the tropospheric eddy-mean flow interaction is quasi-adiabatic with antiphase covariation of FAWA and the zonal mean zonal flow;
- a very robust 25-day periodicity exists in FAWA in the latitude band from 40 to 50 S, but the zonal-mean zonal flow, while covarying with FAWA, holds a distinct spectral shape and does not exhibit a peak at 25 days. This is consistent with the BAM identified by *Thompson and Barnes* [2014] and *Thompson and Woodworth* [2014];
- the primary reasons for this discrepancy are (a) the distinct frequency spectra between the interior momentum flux convergence and the low-level meridional eddy heat flux and (b) a strong thermal damping of surface wave activity.

While the barotropic zonal-mean wind responds primarily to the interior eddy momentum flux convergence, FAWA also depends on the meridional eddy heat flux due to strong thermal damping at the surface. It is the meridional eddy heat flux, whose power spectrum holds a distinctive peak around 25 days, that is the primary driver of the oscillation of FAWA in the frequency range of the BAM. There are some uncertainties in

the surface static stability that affects surface FAWA B and the meridional eddy heat flux term in equation (2.21). Since in the maritime boundary layer static stability tends to be weaker towards the surface, it is possible that the 1 km vertical resolution used in this study overestimates low-level static stability. However in that case, the true value of the meridional eddy heat flux term in equation (3.2) will be *greater*, and none of the points raised above will be affected qualitatively.

I am yet to explain the spectral shape of the low-level meridional heat flux or why it differs so much from the spectrum of the interior eddy momentum flux convergence. Is it that both fluxes are driven by the same large-scale dynamics but their modulation mechanisms are different, or is it that the strong surface thermal damping also alters the timescale of heat flux modulation, or is there something fundamentally different about the dynamics that governs the two fluxes? These questions will be addressed in a subsequent chapter using numerical models.

Appendix 3.A BAM as the leading EOF of EKE anomaly

Although the emphasis of the present study is the application of the FAWA budget to the BAM in the austral summer, as a starting point I reproduce the previous work by calculating the BAM with the method originally introduced by Thompson and the collaborators (TB14, TW14, TL14). Here I define 'summer months' to be December-March and 'winter months' to be June-September. By making the data 4 months long, I increase the spectral resolution in the low frequency range where the BAM appears. The choice of the months is also guided by the observation that there is a well-known, seasonal jump in the location of the jets in the Southern Hemisphere around April-May and September-October. The summer months are within the regime of a 'merged jet' in the mid-latitude, whereas the winter months are within the regime of 'the subtropical jet' (See Figures 3.10 and 3.11).

For each season I computed the first EOF of the zonal-mean EKE anomaly for the Southern Hemisphere from the ERA-Interim reanalysis, following the method of TB14. This is shown in the top row of Figure 3.12 (arbitrary unit). In both seasons the EOF has its amplitude concentrated in the mid-latitudes of the upper troposphere, but in winter its meridional extent expands significantly into the subtropics. It turns out that in summer, the first EOF explains nearly 45 percent of the total variance, whereas in winter it explains only 30 percent of the variance.

The bottom of Figure 3.12 shows the spectra of expansion coefficient of the EOF (the 'BAM index') for the corresponding seasons. In summer, the spectrum has a distinctive peak around ~ 0.04 CPD, clearly defining the BAM frequency. In winter the spectral peak shifts to lower frequency and its peak widens (0.02-0.03 CPD). In fact, around the left shoulder of the peak the spectral resolution begins to deteriorate. Therefore, the BAM timescale is less well separated from the seasonal time scale in winter, and the spectrum is closer to becoming red.

Appendix 3.B FAM1 and FAM2 as the leading EOFs of FAWA anomaly

For an easy comparison with the annular modes, I computed the leading EOFs of FAWA anomaly for the Southern Hemisphere (all year around) from the ERA-Interim reanalysis.

As shown in Figure 3.13, while the leading EOF of the barotropic component of the zonal-mean zonal wind is the annular mode (i.e., meridionally antisymmetric about the jet axis), the leading EOF of the barotropic component of FAWA is a monopole, and the leading EOF's principal component correlates well with the baroclinic annular mode (as defined in Appendix 3.A) and with the volume integral of wave activity between 20 S and 70 S [as defined in equation (2.27)]. Note that conventionally annular modes are calculated with a $\sqrt{\cos\phi}$ weighting to represent the small per-degree area in high latitudes (e.g. *Thompson et al.* [2000]), while taking that into account, here all EOFs are calculated also with a $\cos\phi$ weighting consistent with equations (2.24) and (2.23). The EOF modes are close to Fourier modes, as suggested by *Gerber and Vallis* [2005]. For the zonal-mean zonal wind, momentum conservation prevents a monopole EOF mode, hence the first EOF mode of zonal wind is a dipole, but no similar constraint on the FAWA. The leading EOFs of the zonal-mean zonal wind and of FAWA both make up about half of the total variance, suggesting that these are dominant modes of variability in the SH storm track.

The structure of the second EOF of FAWA is identical to the structure of the annular mode, and its principal component is strongly anti-correlated ($r = -0.89$) with that of the annular mode. This suggests that the second mode of FAWA is a counterpart of the annular mode, but with opposite phase information – a statistical representation of the non-acceleration theorem in equation (2.26).

For brevity, following the terminology of referring to the annular mode as AM, the FAWA mode 1 and FAWA 2 may be referred to as FAM1 and FAM2. Unlike the annular mode being the sole EOF mode of concern in most literature, FAM1 and FAM2 make up a *family* of two modes with equal physical significance.

With AM, FAM1, and FAM2, the essence of the SH storm track dynamics may be cap-

tured in a low-order model. To construct this model, I first examine the projection of eddy forcing onto different modes. From the eddy forcing spectra of Section 3.3.2 and the FAWA equation (2.23), it is safe to say that the eddy heat flux contribution primarily projects on FAM1, whereas the eddy momentum flux contribution primarily projects on FAM2 (AM). Therefore, I propose that the first order dynamics of the SH mid-latitue eddy-mean flow interaction can be succinctly characterized by the following three coupled equations:

$$\frac{\partial}{\partial t} z = -m - \frac{z}{\tau}, \tag{3.3}$$

$$\frac{\partial}{\partial t} A_1 = m_1 + h + D_1, \tag{3.4}$$

$$\frac{\partial}{\partial t} A_2 = m_2 + D_2, \tag{3.5}$$

where z is the projection from the zonal-mean zonal flow on the AM, A_1 and A_2 are the projections from FAWA on FAM1 and FAM2, respectively, m_i and h are the projections from the eddy momentum flux convergence and from the eddy heat flux, D_1 and D_2 are projections from the diabatic heating. The dissipation of A_1 and A_2 are neglected. Equations (3.3) and (3.5) are coupled through the approximate non-acceleration theorem as $z \approx -A_2$ (in the limit of small damping). Surface wave activity B equation is ignored as its amplitude is small when compared to the interior FAWA. Equations (3.3)-(3.5) govern two independent modes (since z and A_2 are related) in equations (2.21),(2.23),(2.24). That A_1 (BAM) is decoupled from z and A_2 (AM) is because h is slaved to the strong surface thermal damping.

The above model, including FAM1 and FAM2, complements the simple one-equation system in *Lorenz and Hartmann* [2001] by providing the information on eddy through the FAWA equation. With adequate data to evaluate all terms, this diagnostic model can offer insights on feedbacks between them. Unlike *Lorenz and Hartmann* [2001] who rely

on stochastic forcing of the eddy momentum flux convergence term m, this model may be driven by the diabatic wave activity sources (D_1 and D_2) and damped by friction on z, mediated by the eddy fluxes m and h. Of course to close the wave activity-zonal momentum cycle one needs to parameterize m and h, incorporating the process of baroclinic instability etc. Detailed interaction and feedbacks within the new set of equations are the subject of a future study.

CHAPTER 4

A MODEL HIERARCHY OF PERIODICITY IN STORM TRACK

In the previous chapter, I have shown that a statistically significant 25-day periodicity exists in FAWA of the austral summer storm track between 40 S and 55 S, which is primarily driven by the low-level eddy meridional heat flux. Figures 3.10, 3.11, and 3.7 illustrate that the seasonal changes in the zonal-mean state and those of the eddy statistics are closely related.

However, though the FAWA budget provides a useful diagnostic framework, causality is not immediately evident since the mean flow and eddies influence each other. To understand the underlying dynamics I start by asking the question: what would be the simplest model that produces this 25-day periodicity?

An appropriate model hierarchy is very important to single out essential physical processes in nature [*Held*, 2005]. As elucidated in *Shaw et al.* [2016] (see Figure 4.1), employing progressively simpler models incorporating selected physical processes of the full model can be a very helpful strategy to understand challenging phenomena. In our case, at the bottom of the model hierarchy lies the two-layer quasi-geostrophic (QG) model [*Phillips*, 1951, 1954, 1956] that has proven to capture the first order dynamics the mid-latitudes: for example connecting surface frontogenesis with the upper tropospheric transient waves (c.f. Chapter 2.1.2). In fact, the Phillips two-layer QG model was the first simple 'GCM' that demonstrated the feasibility of numerical weather prediction [*Phillips*, 1956]. *Held* [2005] draws an illuminating analogy between the two-layer QG model (for climate science) and *E. coli* (for biology). My strategy in this chapter is to use the model hierarchy to search for hints of the oscillation, and then to identify a minimal model that reproduces the essence of the observed oscillation to reveal the key physical processes.

In Section 4.1 I will briefly investigate a series of state-of-the-art climate model outputs with varying treatment of oceans to explore the possible roles of the air-sea interaction in the 25-day periodicity during the austral summer. In Section 4.2, I adopt a dry

dynamical core of a GCM to investigate the role of the mean state in shaping the eddy forcing spectra for the austral summer. I show that a dry GCM is capable of producing a BAM-like eddy heat flux spectra only if the zonal mean state resembles that of the austral summer and if the surface thermal damping rate is chosen judiciously. In Section 4.3, I adopt the *E.coli* climate model – the two-layer QG model – to show that even this minimally equipped model is capable of producing the 20-30 day periodicity and that it depends critically on the imposed profiles of baroclinicity.

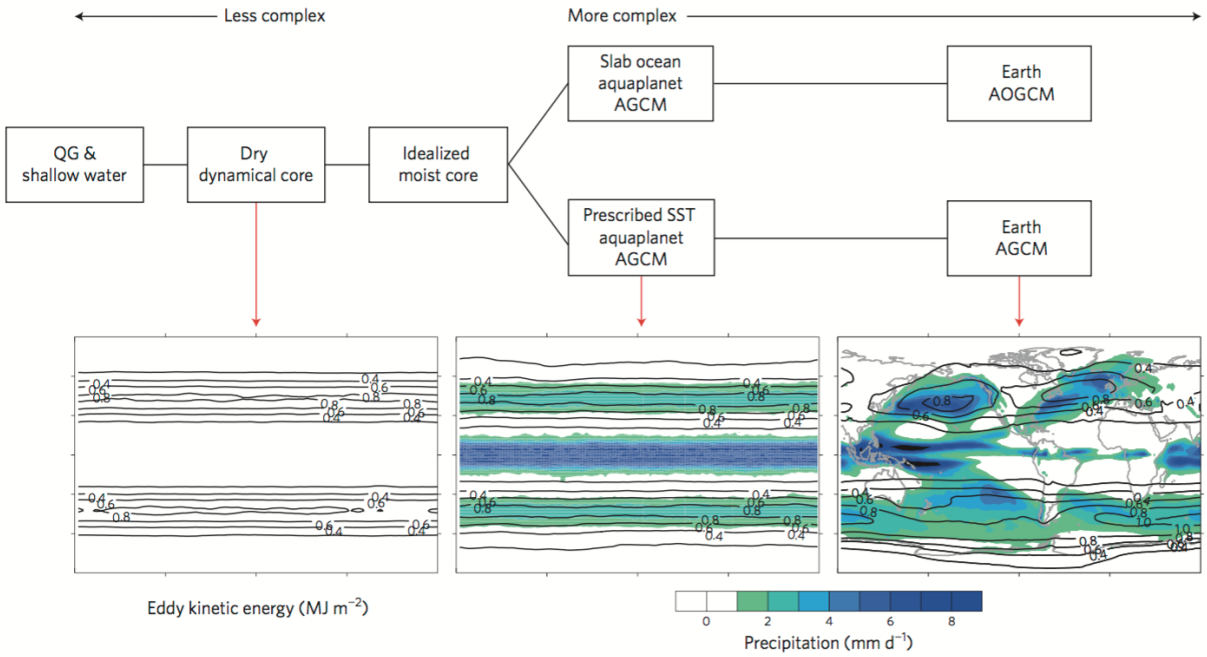

Figure 4.1: Idealized model hierarchy. Lower panels show examples of modelled vertically integrated EKE (contours) and precipitation (shading). Reprinted by permission from Macmillan Publishers Ltd: [Nature Geoscience] (*Shaw et al.* [2016]), copyright (2016)

4.1 Climate models (possible roles of oceans)

As discussed in the previous chapter, the low-level meridional eddy heat flux in the mid-latitudes is a crucial driver for the variability of FAWA. Specifically, a periodicity in the

low-level meridional eddy heat flux leads to a periodicity in the FAWA in the Southern Hemisphere summer. While the periodicity in the austral summer is robust in the ERA-Interim reanalysis products (as it is assimilated with direct observations), the ECMWF model producing the ERA-Interim may or may not reproduce the periodicity on its own. To identify the essential physical processes for the austral summer periodicity, I use a hierarchy of climate model outputs, starting with the ones that reproduce the periodicity and remove one element at a time, which will eventually reveal the indispensable ingredients.

Since the observed periodicity in the storm track ($\sim$ 25 days) is longer than the typical timescale of synoptic eddies in the atmosphere (a few days), there is a possibility that the dynamics of the ocean is affecting the overlying atmosphere. Therefore I begin with a full climate model with dynamically coupled atmosphere and oceans. Throughout this subsection, I will focus on analyzing the existing outputs [1] of the Community Earth System Model version 1 (CESM), whose default full version is a fully-coupled, global climate model that provides state-of-the-art computer simulations of the Earth's climate states. The CESM contains a Community Atmosphere Model (CAM) version 5.2 as its atmospheric component with the nominal 1-degree latitude/longitude resolution, which is consistent with most of the climate models participating in the Coupled Model Intercomparison Project Phase 5 (CMIP5, see a description in *Taylor et al.* [2011]). I adopt the model outputs from a set of pre-industrial control simulations with sufficient integration length [2]. These CESM outputs come from the *Large Ensemble Community Project* [*Kay et al.*, 2015] and the *Aquaplanet Project* [*Medeiros et al.*, 2016].

Figure 4.2 compares the 850 hPa eddy heat flux spectra for both summer and winter

1. On the other hand, I conducted a series of gray radiation model integrations myself, as described below.

2. In this subsection, the high-end 0.1 degree CESM outputs contain 30-year data, the fully-coupled / slab-ocean / atmospehre-only one degree CESM outputs contain 100-year data, the aqua-planet CESM outputs contain 5-year data (no seasonal cycle is allowed, which increases the effective length of the data), and the grey radiation aquaplanet outputs contain 10-year data.

in a hierarchy of CESMs. Since most climate model outputs in this subsection have daily temporal resolution, the top row of Figure 4.2 reproduces the eddy heat flux spectra with the ERA-Interim in Figures 3.7c and 3.7f using the same method [3].

I start the discussion of model hierarchy from the high-end simulations of the CESM that were made possible through the *Accelerated Scientific Discovery* project. The high-end CESM contains an eddy-permitting ocean model with a 0.1 degree horizontal resolution [4], therefore the ocean and atmosphere are tightly coupled. With mesoscale ocean processes resolved, the CESM with 0.1 degree ocean produces variability comparable to the ERA-Interim [5]. As *Ma et al.* [2015] point out, the large-scale atmospheric variability is sensitive to the appearance of mesoscale ocean eddies.

The bottom panels of Figure 4.2 show the meridional eddy heat flux spectra from the outputs of the pre-industral control simulations of CESM with coarser resolution dynamic ocean. Qualitatively in agreement with the ERA-Interim, these results suggest that the 25-day periodicity and its seasonality are robust in a typical climate model such as the default setup of the CESM, although the overall intensity of the heat flux spectra tends to be smaller than the reanalysis, particularly underestimating the high-frequency contributions in summer.

In Figure 4.3, I change the representation of the oceans from the default CESM. I show the meridional eddy heat flux spectra from the pre-industrial control simulations of CESM with a slab ocean (top row) and forced by climatological SST (bottom). Besides

3. In Figure 3.7, I calculated the eddy heat flux based on 6-hourly data and then took the daily average. Here I calculate the daily averages of v and T first and then calculate the eddy heat flux. Note that the two approaches yield different results – the former provides more faithful variances, yet the latter approach is more consistent with the archiving practices of climate models. Though the latter underestimates the variances of the eddy heat flux, it makes the comparison apple-to-apple.

4. Global high-resolution ocean models are prohibitively expensive for most university research groups, e.g. the 0.1 degree CESM takes 25 million core hours to complete a single realization of a 100-year integration.

5. It also appears that only this high-end CESM differs greatly from the others in terms of the winter heat flux spectra. In fact, it captures a BAM-like spectral peak even in the austral winter. This interesting fact is a subject of an ongoing research that is beyond the scope of this thesis.

that both models in Figure 4.3 have the identical surface configuration, including the topography. These models also produce a 25-day periodicity in summer just as the default CESM, which suggests that a dynamical ocean and its thermal interaction with the atmosphere are not crucial for generating this periodicity.

In Figure 4.4, I investigate the periodicity in an even simpler model – an auqaplanet version of the CESM [*Medeiros et al.*, 2016]. No seasonal cycle is allowed, and no topography is added in this simulation. Moreover, while maintaining most of the functionality of the CESM for consistency, a constant cloud droplet and number concentrations in the microphysics package is enforced, which removes cloud-aerosol effects to further simplify the simulation. Although the peak latitude shifts slightly toward the equator, a periodicity around 30 days appears, which qualitatively resembles the ERA-Interim summer condition. This suggests that topography and the zonal asymmetry in the surface boundary condition are not essential ingredients for the 25-day periodicity.

Further, in Figure 4.5, I show the results from a baseline aquaplanet model. This gray-radiation model is described in *Frierson* [2006]. I first run the model with a slab-ocean with the default setup in *Frierson* [2006] for 10 years, then I take the zonal mean and time mean of the generated SST profile, which is subsequently used in the fixed SST simulation. For the fixed SST simulation, I first run the model for 2000 days to reach an equilibrium state, and take the subsequent 10-year outputs for analysis. The model has T85 resolution and 25 layers. This version of the gray-radiation model does not rely on a moist convection scheme. Instead, it adjusts vertical temperature profile through an extended planetary boundary layer, which provides a biased climate. Especially since this model does not resolve ice, its meridional temperature gradient becomes very steep in high latitudes. As shown in Figure 4.5, the heat flux spectra are excessive, especially in high latitudes, and it is hard to identify a well-organized spectral peak. Although there are substantial differences between this gray radiation aquaplanet simulation and the CESM aquaplanet simulation, as I will discuss below it is mainly the difference in the

zonal-mean climatological basic state that leads to the disparate eddy heat flux spectra (It turns out that the realized zonal-mean state in the CESM aquaplanet simulation is not too different from the observed austral summer condition.).

I therefore conclude that as long as climatological effects of the oceans are prescribed, the 25-day periodicity can be faithfully reproduced, although it is entirely possible that the coupling between the atmosphere and oceans determines the basic climatology in the first place. With this insight, the internal dynamics of the atmosphere should be sufficient to generate the 25-day periodicity. Hence in the next section I will exclusively focus on idealized atmospheric models.

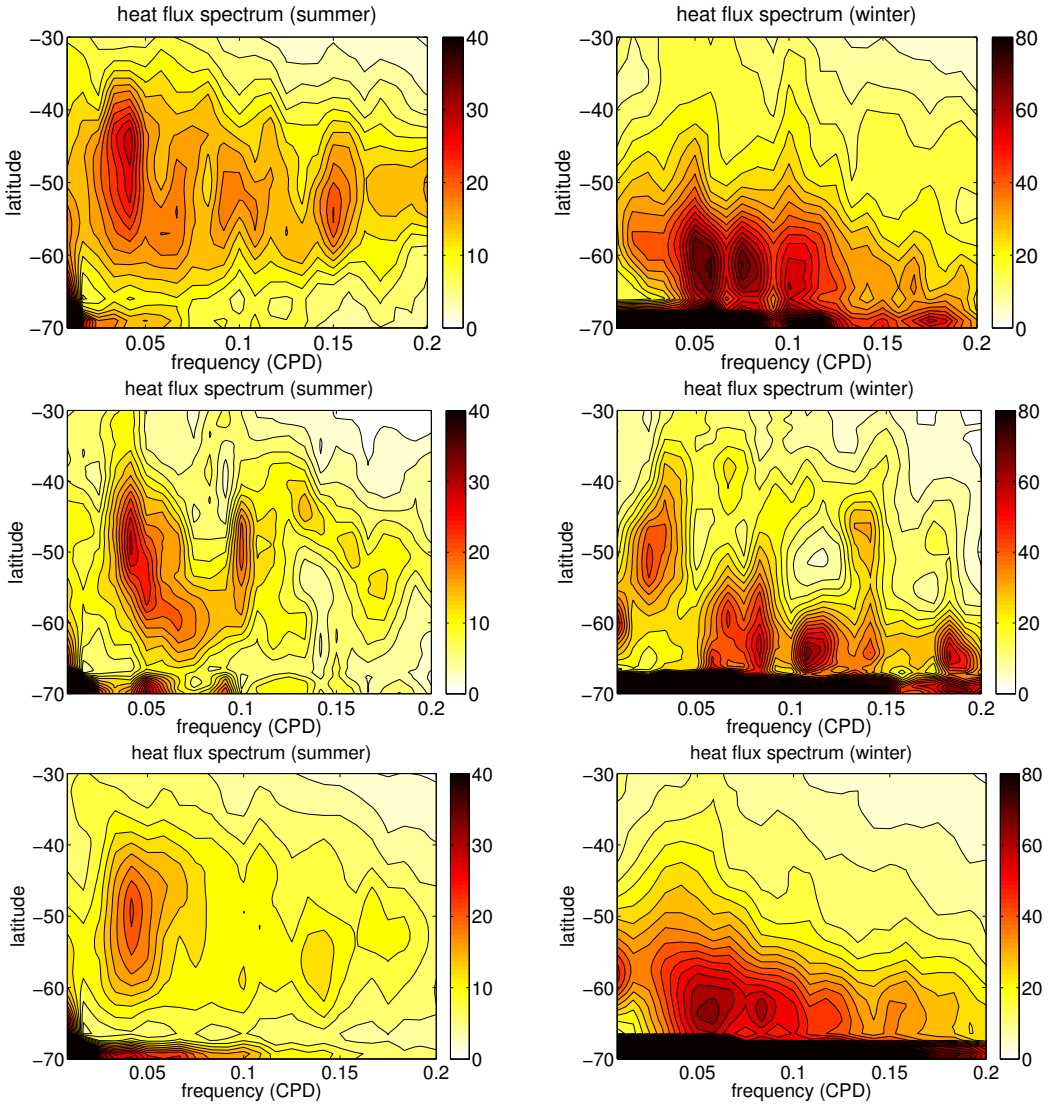

Figure 4.2: 850 hPa Meridional eddy heat flux $\overline{v'T'}$ power spectra for the ERA-Interim reanalysis product (top row), CESM with 0.1 degree ocean and a 0.25 degree atmosphere (middle row) [*Small et al.*, 2014], CESM pre-industrial control simulation [*Kay et al.*, 2015] with one degree dynamical ocean and one degree atmosphere (bottom row).

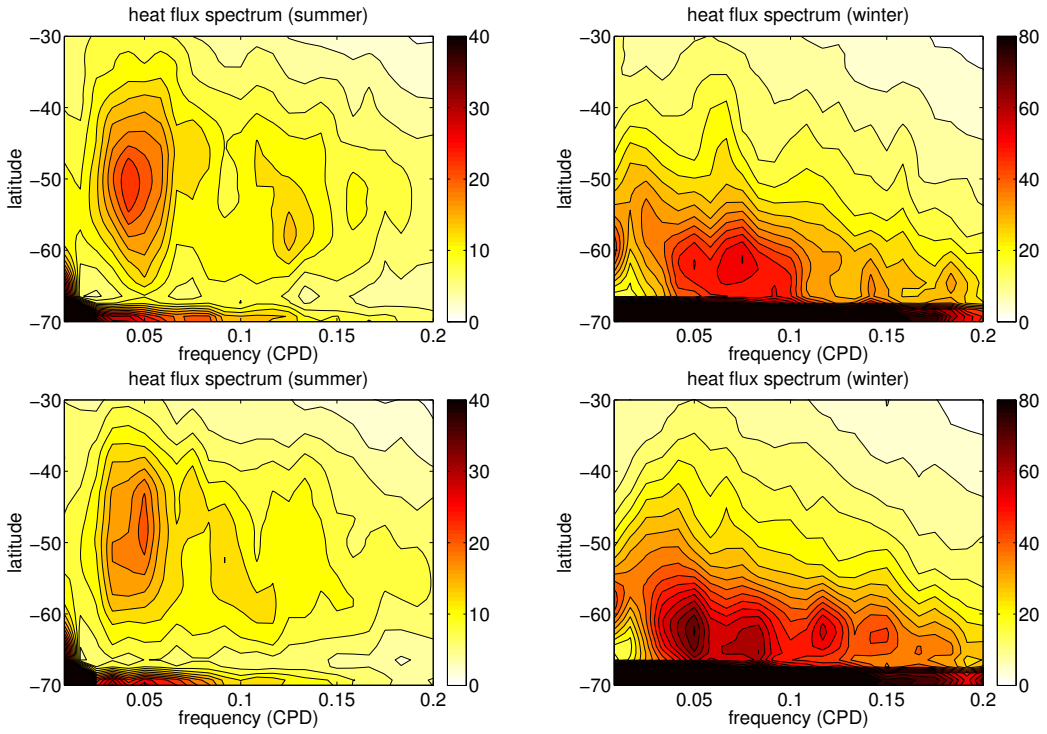

Figure 4.3: Similar to Figure 4.2, but for the meridional eddy heat flux $\overline{v'T'}$ power spectrum for CESM pre-industrial control simulation with one degree slab ocean (top row) and with fixed climatological SST (bottom row). Both models contain a one degree atmosphere.

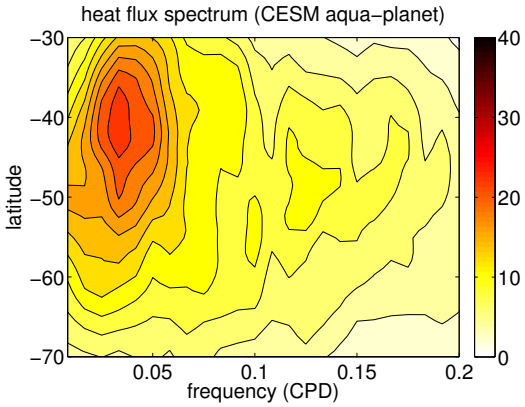

Figure 4.4: Similar to Figure 4.2, but for the meridional eddy heat flux $\overline{v'T'}$ power spectrum for CESM with one degree atmosphere with fixed QOBS SST (Aquaplanet).

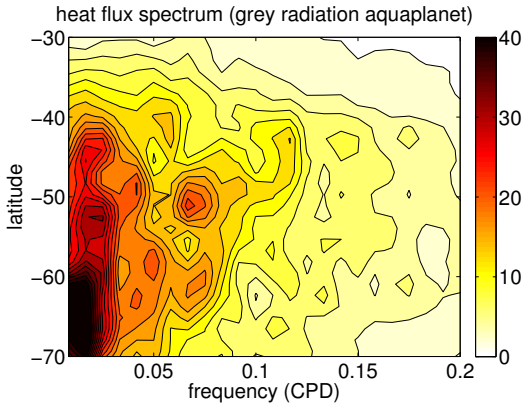

Figure 4.5: Similar to Figure 4.2, but for the meridional eddy heat flux $\overline{v'T'}$ power spectrum for GFDL gray radiation model with T85 resolution and with fixed SST. The SST was obtained as the zonal-mean time-mean SST from a slab-ocean simulation that is identical to that described in *Frierson* [2006].

4.2 Idealized atmospheric general circulation models

Here [6] I use the dynamical core of the Geophysical Fluid Dynamics Laboratory atmospheric GCM. This is a dry primitive equation model with T85 resolution and 20 equally spaced sigma levels. The setup of this model resembles that described in *Held and Suarez* [1994], with linear friction in the bottom level with a damping rate of $(1\text{ day})^{-1}$. In addition, a surface thermal damping rate of $(4\text{ day})^{-1}$ is adopted. To simulate a summer condition, the radiative equilibrium profile T_{eq} is displaced off the equator following *Ring and Plumb* [2007], along with a modification of the stratospheric temperature profile following the appendix of *McGraw and Barnes* [2016]. I refer to this experiment as HS94-SM, where SM means summer.

The model is integrated for 10000 days and the last 8000 days of data are used for the analysis. As shown in Figure 4.6a, HS94-SM produces an eddy heat flux and a momentum flux convergence whose spectra are both broad in frequency. Unlike the austral summer in the ERA (Figure 3.9, bottom), the eddy heat flux contribution to the eddy PV flux is consistently smaller than the eddy momentum flux contribution except at the

6. An earlier version of this material in this section appeared in *Wang and Nakamura* [2016]. ©American Meteorological Society. Used with permission.

lowest frequency at which they are comparable. One may be tempted to attribute this discrepancy to the lack of hydrology. However, there are multiple levels of consequences to removing water from the GCM. For example, the dry model produces a significantly weaker Hadley circulation than the moist model [*Schneider et al.*, 2010] and as a result, the realized time-mean zonal-mean state deviates significantly from the observed mean state. Figure 4.7 depicts the mean state of HS94-SM. Compared to the observed austral summer (Figure 3.10 left), the jet is about 25 percent slower and the tropospheric static stability is significantly weaker (top). In the meantime, HS94-SM also produces an excessive static stability (i.e., temperature inversion) near the surface associated with the cold advection by the equatorward boundary flow [*Held and Schneider*, 1999]. The stronger contrast between the tropospheric and stratospheric static stability leads to an exaggerated QGPV gradient in the upper troposphere, whereas the opposite vertical gradient in the low-level static stability produces a spurious negative QGPV gradient in the mid-latitude lower troposphere (middle). Further, the low-level eddy heat flux in HS94-SM is displaced equatorward relative to the observation (bottom). Given the deviation of the mean state from observation, one cannot straightforwardly attribute the discrepancy of eddy statistics to the lack of hydrology. To separate the effects of the mean state and of hydrology on the eddy spectra, one needs to conduct the experiments differently.

Now I run the above model toward the austral summer. To simulate a climate using the dry dynamical core while maintaining the observed climatological mean state, I adopt the method of *Chang* [2006]. Given a target (observed) zonal-mean temperature profile, a diabatic heating profile is solved iteratively until it balances the time-mean eddy heat flux. The resultant time-mean zonal-mean temperature profile closely matches the target profile. By construction, the obtained diabatic heating profile bears resemblance to the observed diabatic heating profile in the austral summer. I iterate the heating profile for 40 times, with each simulation run for 600 days and the last 400 days taken to calculate the remaining difference from the target. At the end of this iteration, the global

average zonal-mean temperature bias is sufficiently small, i.e.. below 1 K. Thus the effect of moisture on the mean state is incorporated through the zonal-mean heating, whereas eddies are governed by dry primitive equation dynamics. Apart from the adjustment to the mean state, the model architecture and parameter setting are identical to HS94-SM. Since the method of *Chang* [2006] only constrains the zonal-mean temperature field (and the vertical shear in the zonal-mean zonal wind via the thermal wind balance) and not the surface wind, I iterate for the surface friction coefficient in a similar way until the obtained time-mean zonal-mean surface zonal wind closely matches the observation. The resulting optimal damping rate was about $(1.4\ \text{day})^{-1}$. I refer to this experiment as SHSM [7].

When the mean state is adjusted toward the observed austral summer condition, the eddy heat flux in the mid-latitudes exhibits a distinctive low frequency (roughly 30-50 day) spectral peak, which well surpasses the power of eddy momentum flux convergence (Figure 4.6b). Although the spectral shape of the eddy heat flux is closer to that of the observed (Figure 3.9a bottom) than the HM94-SM, the overall power is significantly smaller: less than 1/4 of the observed value. The eddy momentum flux convergence, even though its spectrum is correctly separated from the eddy heat flux spectrum, is disproportionately small at high frequencies (it is comparable to the eddy heat flux). The deficiencies in the eddy flux magnitudes in the GCM with an adjusted mean state are also noted by *Chang* [2006], who attributes them to the lack of diabatic effects on eddies. *Yamada and Pauluis* [2015] also demonstrate that the E-P flux increases significantly in the moist environment. However it is also a natural consequence of the mean state being nudged toward the observed profile by a forcing: since the energy budget constraint is largely met by the zonal-mean forcing, eddies do not need to work as hard to maintain the observed mean state and hence they remain at small amplitude. In addition to the underestimated magnitude, the spectral peak of the eddy heat flux in Figure 4.6b is not sharp and the peak

7. This acronym stands for the Southern Hemisphere summer.

frequency is lower than that of the BAM (∼0.02 CPD).

In the HS94-SM and SHSM experiments above, I have used a surface thermal damping rate of $(4\text{ day})^{-1}$, which linearly decreases to $(40\text{ day})^{-1}$ toward the free troposphere. However, given the analysis in equation (3.1), a stronger surface thermal damping may be more appropriate in the Southern Hemisphere storm track. Strong surface thermal damping was also crucial for decoupling equation (2.23) from (2.21). Thus I have repeated the SHSM experiment with a surface thermal damping rate of $(1\text{ day})^{-1}$. The result in Figure 4.6c shows that the peak of the eddy heat flux spectrum becomes sharper and its frequency is closer to that of BAM (∼ 0.03 CPD).

Figure 4.8 shows the spectra of vertically integrated FAWA for the two SHSM experiments as functions of frequency and latitude. This is similar to Figure 3.7a but the latitude increases upward here due to the experimental symmetry about the equator. (I do not show the FAWA spectra for HS94-SM because the spurious negative QGPV gradients in the lower troposphere of that model prevent FAWA from being calculated accurately.) Keep in mind that both runs have a zonal-mean state nearly identical to the observed profile for the austral summer. With a $(4\text{ day})^{-1}$ surface thermal damping, the spectral peak of FAWA appears at 58° and 0.02 CPD and it extends broadly in the meridional direction and covers the entire extratropics (Figure 4.8a). It is meridionally elongated, more so than the observed spectra of FAWA (Figure 3.7a). However with a $(1\text{ day})^{-1}$ damping, the spectral peak becomes much more compact, located at 48° and 0.03 CPD (Figure 4.8b). Despite an order of magnitude smaller power, the spectral distribution in Figure 4.8b is qualitatively similar to Figure 3.7a.

The above experiments suggest that the profile of the zonal-mean state and the surface thermal damping rate determine the shape of the frequency spectra of the eddy heat flux in the austral summer storm track. Although the lack of latent heat and the forced adjustment toward the observed mean profile underestimate the magnitude of the eddy fluxes, the dry dynamics qualitatively supports a BAM-like oscillation in the eddy heat flux and

FAWA as long as the mean state resembles the observed austral summer condition and the surface thermal damping is carefully chosen.

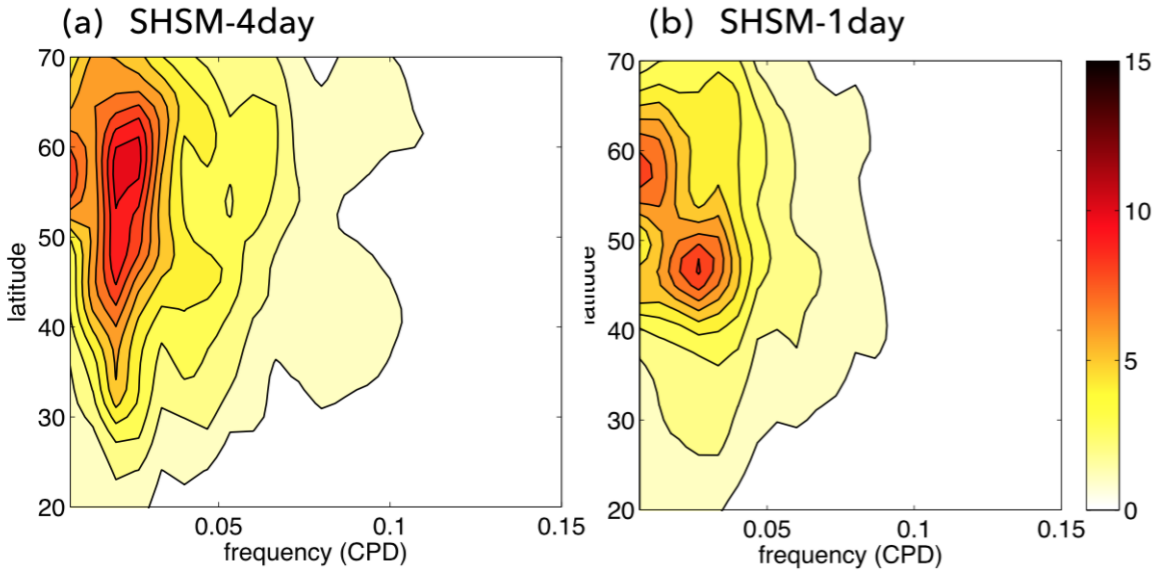

Figure 4.8: Power spectra of the vertically integrated wave activity $\langle A \rangle + B$ as functions of frequency and latitude. (Note: latitude increases upward.) (a) SHSM-4day. (b) SHSM-1day. Contour interval is 1 m^2. See text for details. (appeared in *Wang and Nakamura* [2016]. ©American Meteorological Society. Used with permission.)

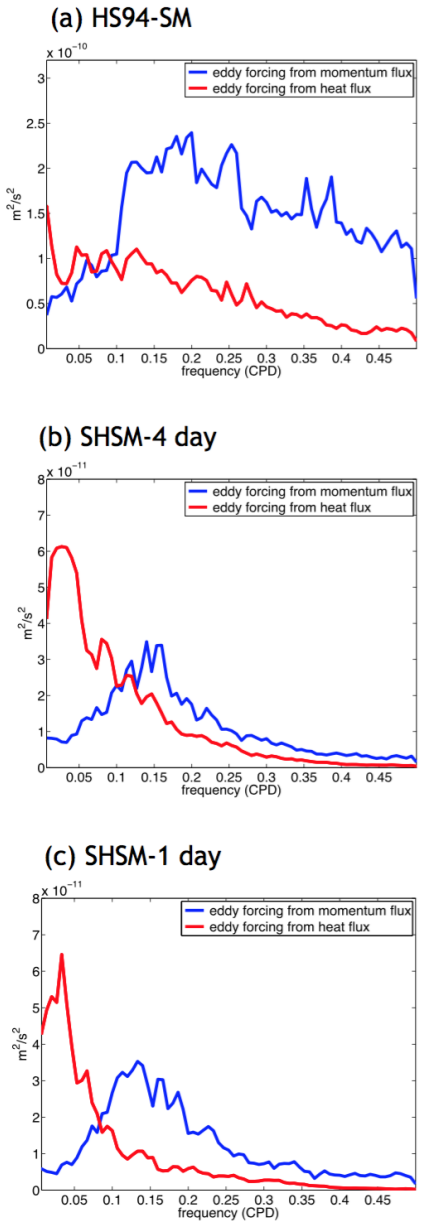

Figure 4.6: Spectra of eddy fluxes at 46.5°S. Red: scaled eddy heat flux. Blue: eddy momentum flux convergence. Conventions are the same as the bottom of Figure 5.1. (a): HS94-SM. (b): SHSM with 4 day thermal damping. (c): SHSM with 1 day thermal damping. See text for details. (appeared in *Wang and Nakamura* [2016]. ©American Meteorological Society. Used with permission.)

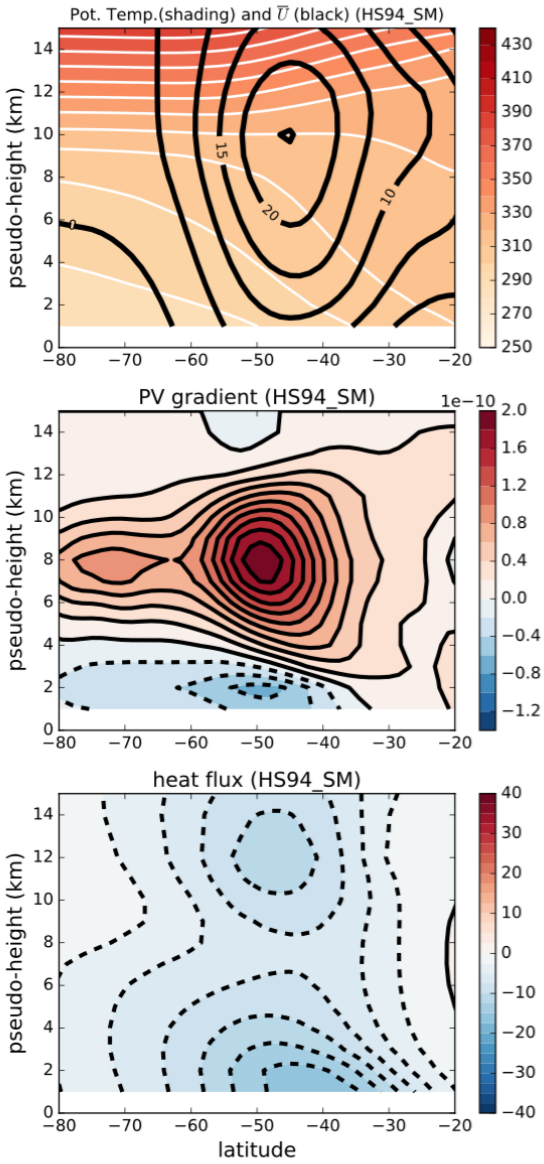

Figure 4.7: Zonal-mean climatology for HS94-SM. The convention is identical to Figure 3.10. The region below z = 1 km is masked due to the interpolation from sigma coordinate to pseudo-height coordinate. (appeared in *Wang and Nakamura* [2016]. ©American Meteorological Society. Used with permission.)

4.3 Two-layer QG model

The two-layer QG model is the simplest climate model that can simulate key characteristics of the extratropical atmospheric general circulation (e.g. *Phillips* [1956]). It contains essential ingredients for the midlatitude storm dynamics, including opposite signs of PV gradients in the two layers, the β-effect, and a meridional density gradient.

4.3.1 Model description

The original two-layer QG model [*Phillips*, 1951] was formulated with equal rest layer thicknesses on the β plane. Although this remains to be a widely adopted practice, following *Nakamura and Wang* [2013] and *Wang and Lee* [2016], I allow the model to have unequal layer thicknesses [8]. This generalization allows one to have a better control of the structure of baroclinicity. The thickness ratio of the two layers also defines the vertical structure of the unstable modes, and keeping it as an adjustable parameter allows one to draw a better analogy between the Phillips and Charney models of baroclinic instability [*Nakamura and Wang*, 2013]. The non-dimensional forms of the governing equations are

$$\frac{\partial q_1}{\partial t} + J(\psi_1, q_1) = -\tau^{-1}\frac{\psi_2 - \psi_1 + \psi_e}{2(2-\delta)} - \kappa\nabla^6\psi_1, \tag{4.1}$$

$$\frac{\partial q_2}{\partial t} + J(\psi_2, q_2) = \tau^{-1}\frac{\psi_2 - \psi_1 + \psi_e}{2\delta} - \gamma^{-1}\nabla^2\psi_2 - \kappa\nabla^6\psi_2, \tag{4.2}$$

where the subscripts 1 and 2 refer to the upper and lower layers, respectively, and the quasi-geostrophic potential vorticity (QGPV) in each layer is:

$$q_1 = \beta y + \nabla^2\psi_1 + \frac{\psi_2 - \psi_1}{2(2-\delta)}, \tag{4.3}$$

$$q_2 = \beta y + \nabla^2\psi_2 - \frac{\psi_2 - \psi_1}{2\delta}. \tag{4.4}$$

8. The model description is modified from the material appeared in *Wang and Lee* [2016]. ©American Meteorological Society. Used with permission.

Note that the constant planetary vorticity is omitted since it does not affect (4.1)-(4.2). Here $\beta = \beta^*/(\Delta U^* {L_d^*}^2)$, where β^*, ΔU^*, L_d^* are constant (dimensional) planetary vorticity gradient, vertical 'shear' (difference in the mean zonal wind between the two layers), and the internal Rossby radius, respectively. τ and γ are nondimensional parameters associated with radiative and Ekman damping, and κ is hyper-viscosity used in the numerical solution. ψ is geostrophic streamfunction, whereas ψ_e prescribes a 'radiative equilibrium' state. δ denotes nondimensional thickness of the lower layer at rest, defined as $\delta \equiv H_2^*/H_0^*$, where $H_0^* \equiv (H_1^* + H_2^*)/2$ and H_1^* and H_2^* are the (dimensional) layer thickness for the upper and lower layers, respectively (the upper layer thickness is $2-\delta$ and $\delta = 1$ corresponds to equal thicknesses). The choice of δ is important – an optimal thickness of the lower layer giving a maximum growth rate of the most unstable mode may be attained both analytically and numerically in a linear system of baroclinic instability [*Nakamura and Wang*, 2013]. Hence this parameter controls the vertical structure of baroclinic instability and the associated criticality of the mean state. In the linear problem the flow becomes subcritical when $\beta\,\delta > 1$. As shown by *Nakamura and Wang* [2013], a shallower lower layer makes it easier to maintain a monotonic (negative) PV gradient, just like the surface temperature gradient (divided by the Coriolis parameter) is monotonic in latitude. In this study we choose a layer thickness ratio of $\delta = 0.25$. The key findings in this study have been tested with other values (e.g. standard equal-layer thickness) as well.

The velocity field is determined by the geostrophic relation:

$$(u_i, v_i) = (-\partial\psi_i/\partial y,\ \partial\psi_i/\partial x), \quad i = 1, 2. \tag{4.5}$$

Time is non-dimensionalized by L_d^*/U^*, where $L_d^* = 750\ km$ is assumed for the internal Rossby radius and $U^* = 45\ ms^{-1}$ is assumed for the velocity scale. Hyper-viscosity is included in both layers to remove enstrophy at small scales. Ekman damping with a dimensional damping time scale of 0.4 day is included in the lower layer only, and radiative

damping relaxes the upper layer zonal mean flow to a prescribed 'radiative equilibrium state' $U_e \equiv -d\psi_e/dy$ and the lower layer to zero wind with a relaxation time scale of 30 days. Similar to the prescription by *Lee and Held* [1991], the following form of radiative equilibrium state $U_e(y)$ is assumed:

$$U_e(y) = \Delta U_0 + \exp\left[-\frac{y^2}{\sigma^2}\right], \tag{4.6}$$

where $\sigma = 2$ is a parameter controlling the width of the baroclinic jet. The main difference between the above U_e profile and the one by *Lee and Held* [1991] is that a domain-wide constant wind shear ΔU_0 is added. As we will see toward the end of this subsection, this additional ΔU_0, which controls the overall strength of baroclinicity, also provides a crucial control for the 25-day periodicity.

The equations (4.1) and (4.2) are solved numerically with Fourier spectral decomposition in the zonal direction and sine function decomposition in the meridional direction. The non-dimensional channel length and width (scaled by L_d^*) are set to $L_x = 20\pi$ and $L_y = 5\pi$, respectively. The chosen width is sufficiently large so that eddy amplitude is negligible near the walls. A sponge layer is added at both northern and southern boundaries to avoid reflecting waves. For the parameters chosen here, the value of the corresponding non-dimensional β is 0.2.

To initialize the numerical integration, following the treatment in *Esler* [2008], a localized, small-amplitude (maximum amplitude of 0.01) perturbation is added to the upper layer eddy PV field with the form:

$$q_1'(x, y, 0) = 0.01 \cdot \left(x - \frac{L_x}{2}\right) \cdot \exp\left[-\frac{(x - \frac{L_x}{2})^2 + y^2}{10^2}\right], \tag{4.7}$$

where the prime denotes the perturbation from the zonal-mean. Since such a perturbation excites all wavenumbers in spectral space, the fastest growing normal mode naturally emerges. Moreover, the small amplitude of the initial perturbation allows the fastest

growing normal mode to attain large amplitude through baroclinic instability before it reaches nonlinear saturation. The simulations are each integrated for 6000 days, and the last 4000 days are stored for analysis.

4.3.2 General properties of eddy-mean flow interaction

The two-layer QG model contains essential properties of the mid-latitude eddy-mean flow interaction. This subsection demonstrates that different flow regimes emerge under different parameter settings and how they are related to the observed features of the mid-latitude eddy-mean flow interaction.

The variability of eddy and the mean flow in the two-layer QG model depends on its flow regime parameters, as initially discovered by *Lorenz* [1963a]. *Lee and Held* [1991] found that when friction on the lower layer is strong, the two-layer QG model can vacillate between a wave-free state and a finite-amplitude wave state over a substantial region of the model's parameter space. *Lee and Feldstein* [1996] (hereafter LF96) evaluated the importance of the width of the baroclinic zone in a two-layer QG model by changing the relative size of the radiative equilibrium state profile to the domain's meridional size. LF96 found that the leading EOF of the zonal-mean zonal flow can change from a monopolar pulsing structure to a dipolar structure as the width of the baroclinic zone increases, and for a sufficiently wide baroclinic zone, a double-jet structure would emerge. The dipole-like oscillation is triggered by the separation between the meridional size of baroclinic eddies and that of the lower layer meridional PV gradient. In other words, the dipole-like oscillation is suppressed if these two scales are comparable.

I obtained similar results to LF96 but by varying a different parameter – layer thickness ratio. In Figure 4.9, as the two-layer QG model becomes more 'top-heavy' (i.e. smaller δ), the leading EOF of the zonal-mean zonal wind changes from monopolar to dipolar. In the left panel of Figure 4.9, the first EOF of the $\delta = 1$ simulations displays a pulsing pattern and there is no obvious dipole-like wobbling pattern. In the right panel

of Figure 4.9, the first EOF of the $\delta = 0.25$ simulations displays an dipole-like wobbling pattern while the second EOF displays a pulsing pattern. These results show that in the zonal-mean zonal flow the dipole-like oscillation is robust when the lower layer thickness is small in the two-layer QG model simulations, especially in the $\delta = 0.25$ case. In light of Figure 3.13, this captures some key features of the annular mode in the real atmosphere.

This is analogous to the results of LF96 because by reducing the layer thickness ratio, one effectively increases the width of the baroclinic zone. Figure 4.10 shows the radiative equilibrium state U_e and the associated PV gradients in the two layers for a layer thickness ratio of $\delta = 1$ (left column, hereafter as D100) and $\delta = 0.25$ (right column, hereafter as D025). Even though U_e is identical in both cases, the lower layer PV gradient in D025 is strongly negative, effectively creating a much wider baroclinic zone. The result in Figure 4.9 shows that either dipole-like variation or monopole-like variation exists in the two-layer QG model and the structure of the leading mode depends on the flow parameters [9].

The two-layer QG model also captures the essence of the finite-amplitude wave - mean flow interaction. In order to adopt the two-layer QG model to study the 25-day periodicity of finite-amplitude wave activity, the zonal-mean zonal flow equation (2.9) needs to be constructed in a vertically discretized form (ignoring the dissipation and friction):

$$\frac{\partial \overline{u}_1}{\partial t} = f_0 \overline{v}_1^* + \overline{v_1' q_1'}, \tag{4.8}$$

$$\frac{\partial \overline{u}_2}{\partial t} = f_0 \overline{v}_2^* + \overline{v_2' q_2'}, \tag{4.9}$$

9. In a non-homogeneous two-layer QG model like the one adopted here, changing one parameter is always accompanied by changing other parameters.

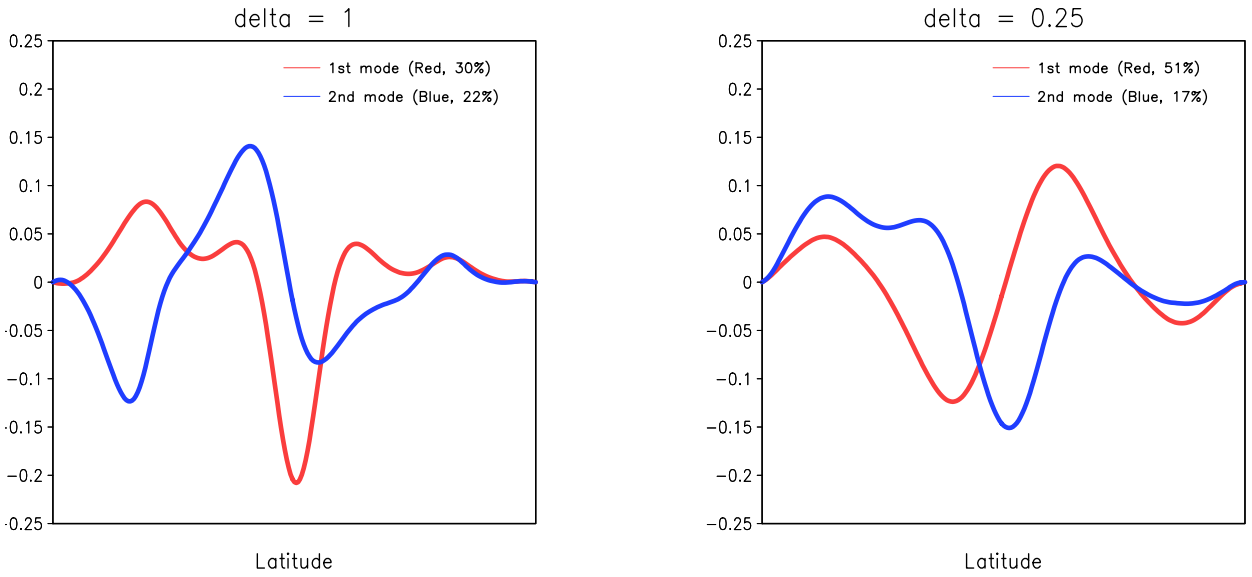

Figure 4.9: The first (red curves) and second (blue curves) EOFs of the barotropic component of the $\overline{u}$ anomaly in a forced-dissipative experiment with a fully nonlinear two-layer model, for layer thickness ratio $\delta = 1$ (left) and $\delta = 0.25$ (right) respectively.

where the residual circulation is defined as [similar to equations (2.10) and (2.17)]:

$$\overline{v}_1^* \equiv \overline{v}_1 - \frac{1}{H_1}\overline{v_1'\eta'}, \tag{4.10}$$

$$\overline{v}_2^* \equiv \overline{v}_2 + \frac{1}{H_2}\overline{v_2'\eta'}, \tag{4.11}$$

where η' is the thickness perturbation defined as $\eta' = f_0(\psi_2' - \psi_1')/g'$, where g' is the reduced gravity $g' = 2{L_d^*}^2 f_0^2/H_0^*$. The eddy meridional mass fluxes $\overline{v_i'\eta'}$ should balance each other between the upper and lower layers:

$$\overline{v_1'\eta'} = -\left(-\overline{v_2'\eta'}\right) \tag{4.12}$$

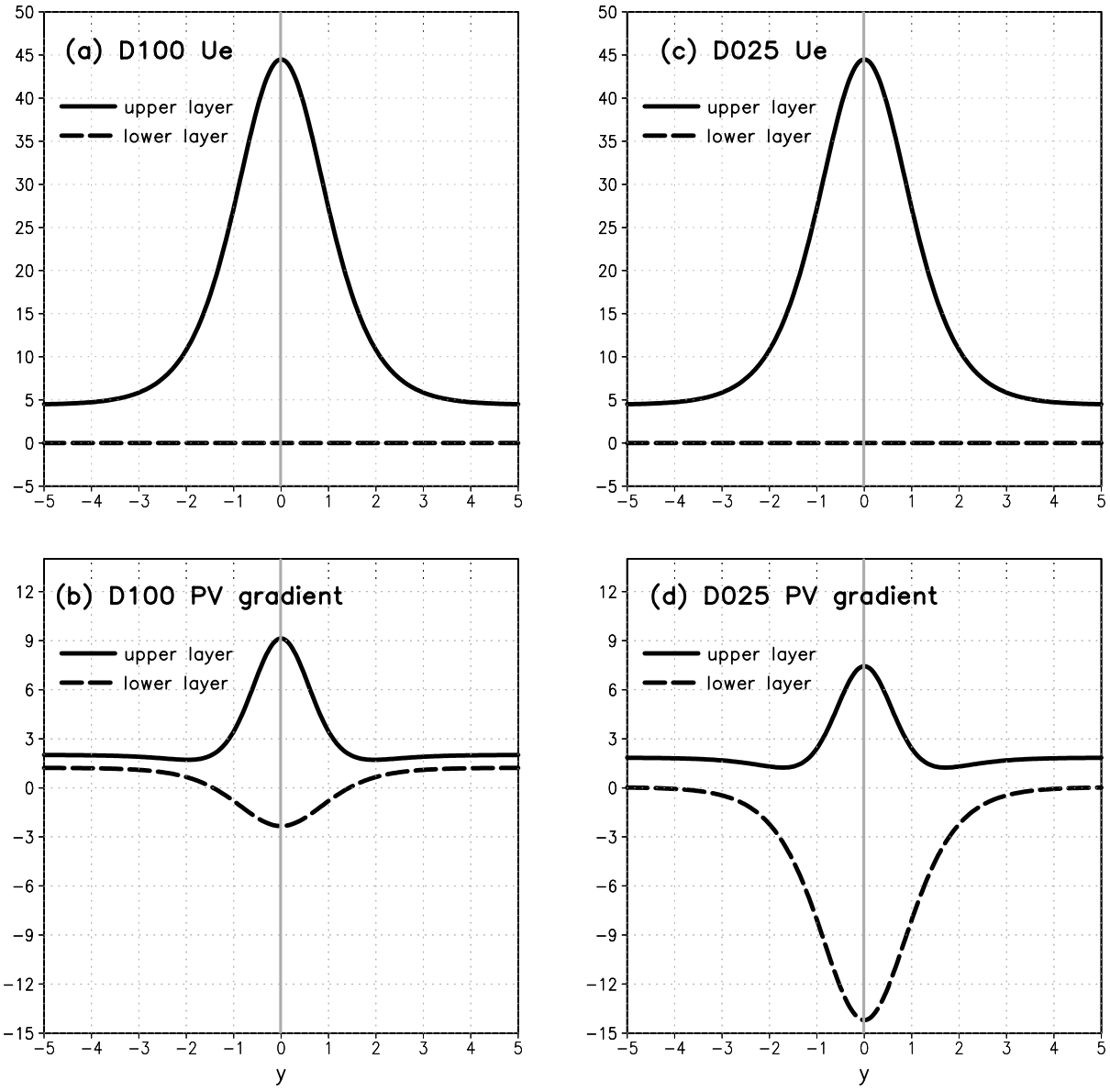

Figure 4.10: The radiative equilibrium state U_e and the associated PV gradient dq_e/dy, a fully nonlinear two-layer model for layer thickness ratio $\delta = 1$ (left column) and $\delta = 0.25$ (right column) respectively. Units for upper panels are ms^{-1}, and units for lower panels are $10^{-11}m^{-1}s^{-1}$. One unit in the horizontal axis corresponds to one radius of deformation $L_d^* \equiv 750$ km.

Correspondingly, the vertically discretized FAWA equations [10] are:

$$\frac{\partial A_1}{\partial t} + \overline{v_1' q_1'} = 0, \tag{4.13}$$

$$\frac{\partial A_2}{\partial t} + \overline{v_2' q_2'} = 0. \tag{4.14}$$

Adding the zonal-mean zonal flow and FAWA equations [(4.8) (4.13) and (4.9) (4.14)] for each layer, one obtains:

$$\frac{\partial}{\partial t}(\overline{u}_1 + A_1) = f_0 \overline{v}_1^*, \tag{4.15}$$

$$\frac{\partial}{\partial t}(\overline{u}_2 + A_2) = f_0 \overline{v}_2^*. \tag{4.16}$$

Note that the residual circulation cancels with each other between the upper and lower layers (no net meridional mass flux):

$$H_1 \overline{v}_1^* + H_2 \overline{v}_2^* = 0. \tag{4.17}$$

With equations (4.15) (4.16) (4.17), the non-acceleration theorem for the two-layer QG model [a counterpart to equation (2.26)] can be derived:

$$\frac{\partial}{\partial t}(H_1 \overline{u}_1 + H_2 \overline{u}_2) = -\frac{\partial}{\partial t}(H_1 A_1 + H_2 A_2). \tag{4.18}$$

This states that a decrease in the barotropic part of the zonal-mean flow is accompanied by an increase in the barotropic part of the finite-amplitude wave activity, and vice versa. Figure 4.11 summarizes the co-variation of the mean flow and wave activity in the two-layer QG model simulations. It is analogous to Figure 3.4 and demonstrates that the relation (4.18) is robust. In particular, the $\delta = 0.25$ case (bottom panels) exhibits a bet-

10. In this case the lower layer wave activity A_2 is analogous to the surface wave activity in the stratified flow, hence A_2 is equivalent to the surface wave activity as defined in (2.21).

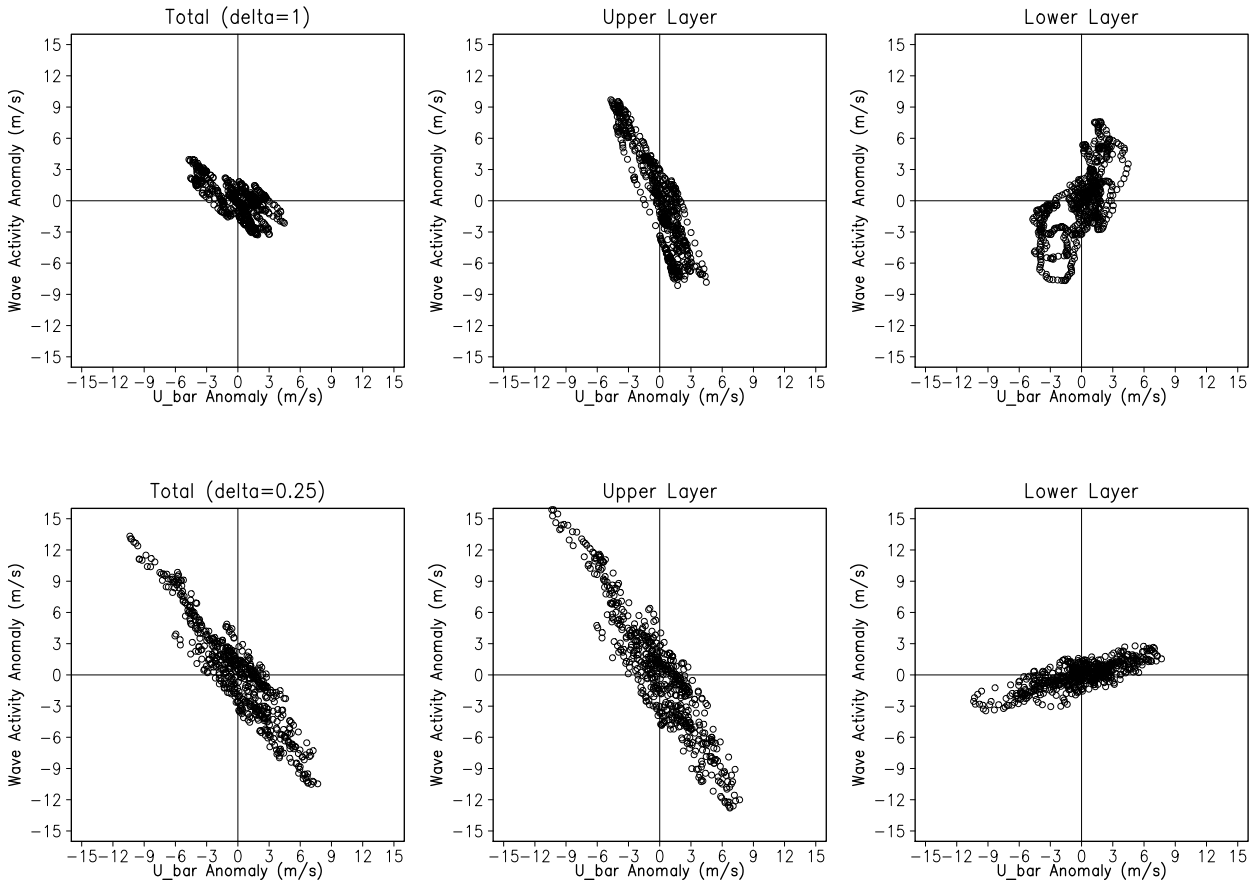

Figure 4.11: (Left) The anomaly of barotropic component (mass weighted) of the zonal-mean zonal wind $\langle \overline{u} \rangle$ versus the anomaly of the barotropic component of finite-amplitude wave activity at the center of the channel in a forced-dissipative experiment with a fully nonlinear two-layer model. (Middle) Same as the left panels but for $\langle \overline{u} \rangle$ versus upper layer wave activity. (Right) Same as the left panels but for $\langle \overline{u} \rangle$ versus lower layer wave activity. The top panels are the results for layer thickness ratio $\delta = 1$, whereas the bottom panels are for $\delta = 0.25$.

ter agreement to those in the real atmosphere (Figure 3.4) than the traditional equal-layer model (top panels), suggesting that $\delta = 0.25$ is more representative of the real atmosphere in the sense that its upper layer resembles the interior atmosphere and its lower layer behaves like the surface. It is therefore deemed that the two-layer QG model is a adequate tool to study the underlying mechanism of the 25-day periodicity with this particular choice of the parameter.

4.3.3 *Periodic behavior arises with a reduced baroclinicity*

To the extent that equations (4.13) and (4.14) hold, if a periodic behavior in FAWA arises it should arise from the eddy PV fluxes, which are connected to the eddy momentum flux divergence and eddy thickness (heat) flux through the Taylor identity [11]:

$$\overline{v_1{}'q_1{}'} = -\frac{\partial}{\partial y}\overline{u_1{}'v_1{}'} + \frac{1}{2\cdot(2-\delta)}\overline{v_1{}'(\psi_2{}' - \psi_1{}')}, \tag{4.19}$$

$$\overline{v_2{}'q_2{}'} = -\frac{\partial}{\partial y}\overline{u_2{}'v_2{}'} - \frac{1}{2\cdot\delta}\overline{v_2{}'(\psi_2{}' - \psi_1{}')}. \tag{4.20}$$

Since the two-layer model only has one layer interface, the meridional eddy heat flux is represented by the thickness flux. The small thickness ratio ($\delta \equiv 0.25$) has an extra strength to put the eddy heat flux in the lower layer, representing the lower troposphere below $\sim$ 850 hPa, which is consistent with the real atmosphere (e.g. Figure 3.9 bottom row). Moreover, by reducing the thickness of the lower layer, the effective damping rate on the lower layer QGPV is increased, which is analogous to an enhanced thermal damping rate to the surface temperature.

I next investigate the sensitivity of the eddy heat flux to the domain-wide baroclinicity in a two-layer QG model. In nature, the change of domain-wide baroclinicity could be caused by a seasonal cycle or a reduced equator-to-pole temperature gradient that tends to occur in warm climates. To investigate the extent to which periodicity in the eddy heat flux spectrum is influenced by the domain-wide baroclinicity, I conduct sensitivity experiments by systematically varying the vertical wind shear ΔU_0 in U_e. As the wind shear ΔU_0 increases, the flow becomes more supercritical to baroclinic instability.

Figure 4.12 shows that, as the baroclinicity is reduced, a pronouced periodicity in the eddy heat flux arises at around 0.04 CPD [12], strongly resembling the periodic behavior in the austral summer in Figure 3.9 (bottom left). As the baroclinicity increases, the

11. This is a vertical discretization of equation (2.11)

12. This is after dimensionalizing by L_d^*/U^*.

eddy heat flux spectrum reddens and the peak disappears, more like the austral winter in Figure 3.9 (bottom right). In contrast, the spectral shape of the eddy momentum flux convergence remains relatively unchanged, except that the overall intensity of the spectra increases with the baroclinicity. This suggests that, in a weakly baroclinic flow, the eddy heat flux spectra and the eddy momentum flux convergence spectra are well seperated, hence the FAWA is more readily driven by the eddy heat flux around the frequency of 0.04 CPD – giving rise to the 25-day oscillation.

Figure 4.13 depicts the EOFs of FAWA. The general features among all simulations are that the leading EOFs all have a monopolar structure, whereas the second EOFs all have a dipolar structure. The two leading EOFs are the FAM1 and FAM2 defined in Appendix 3.B in the context of ERA-Interim reanalysis products. The FAM2 have similar structures to the first EOFs of zonal-mean zonal winds (i.e. annular mode, not shown). These results suggest that FAWA variability can be succinctly captured by FAM1 and FAM2. As baroclinicity is reduced, both FAM1 and FAM2 contain more variance. When FAM1 reaches a certain variance level ($\sim 40\%$), the 25-day periodicity appears. As the overall baroclinicity increases the meridional extent of FAM1 expands. This appears to be analogous to the austral winter condition, in which the BAM has more meridionally elongated structure (Figure 3.12).

As a short summary, after walking through the entire model hierarchy, I have teased out several potential drivers of the observed oscillation from the climate system, such as the role of the oceans and of the topographic features. From this exercise, I discovered that the role of the basic state is indispensable for the 25-day periodicity. Based on this insight, I took the simplest climate model – a two-layer QG model – and constructed an eddy-mean flow interaction framework in a similar fashion to the one that I developed and diagnosed for reanalysis products in Chapters 2 and 3. Finally I conclude that the basic dynamics of the 25-day periodicity is encapsulated in a two-layer QG model – as baroclinicity is reduced, the 25-day periodicity arises. This is consistent with the findings

in Chapter 3 in which I discovered that the 25-day periodicity is robust only in the warm season with an overall weak tropospheric pole-to-equator temperature difference [13].

The next chapter attempts at unpacking the mechanism of the periodicity.

13. That said, it is worth mentioning that the low-level temperature gradient in the mid latitude austral summer is actually greater than in winter.

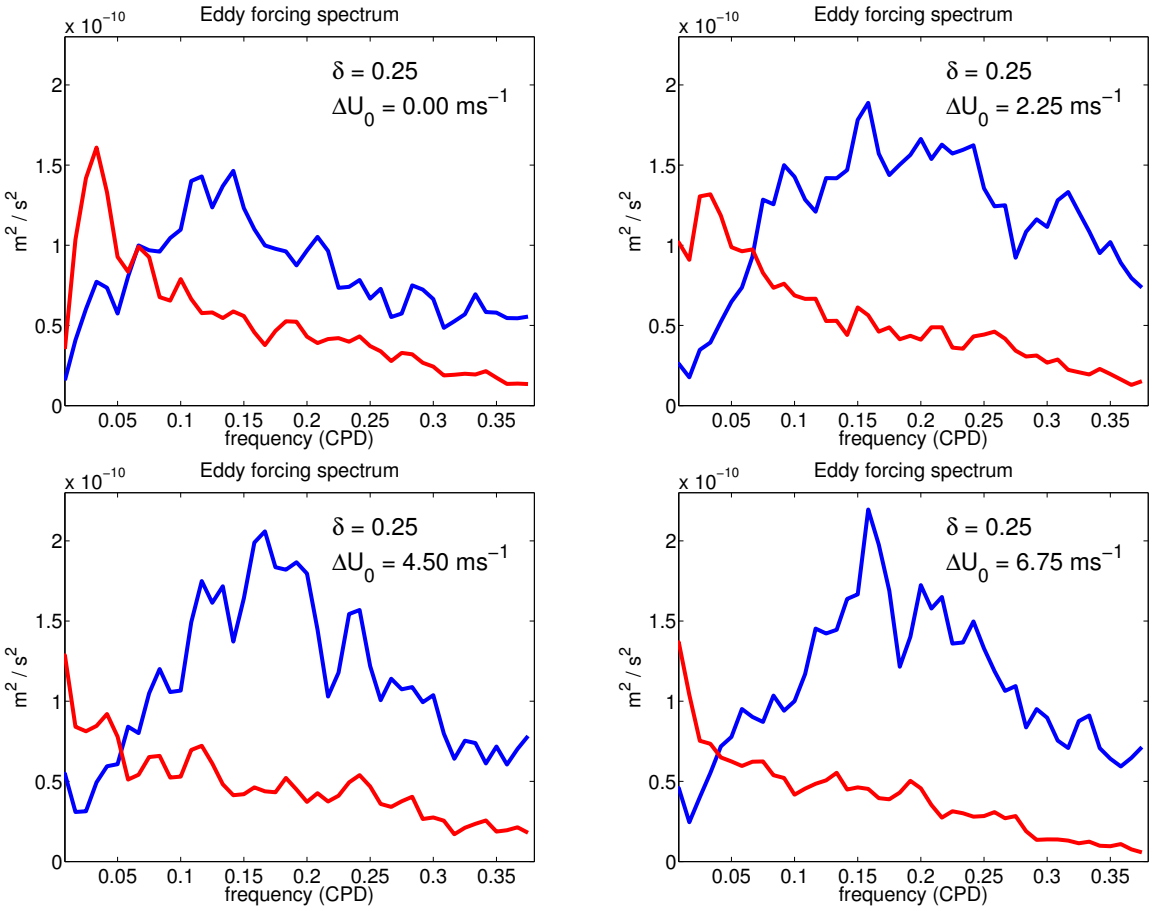

Figure 4.12: Spectra of eddy fluxes at the middle of the channel. Red: the eddy heat flux contribution to the barotropic eddy PV flux. Blue: the eddy momentum flux convergence contribution to the barotropic eddy PV flux. Conventions are the same as the bottom of Figure 5.1. (upper left): $\Delta U_0 = 0\ ms^{-1}$. (upper right): $\Delta U_0 = 2.25\ ms^{-1}$. (lower left): $\Delta U_0 = 4.5\ ms^{-1}$. (lower right) $\Delta U_0 = 6.75\ ms^{-1}$. $\delta = 0.25$ is used for all the experiments. Each simulation is integrated for 6000 days and the last 4000 days are used for the analysis.

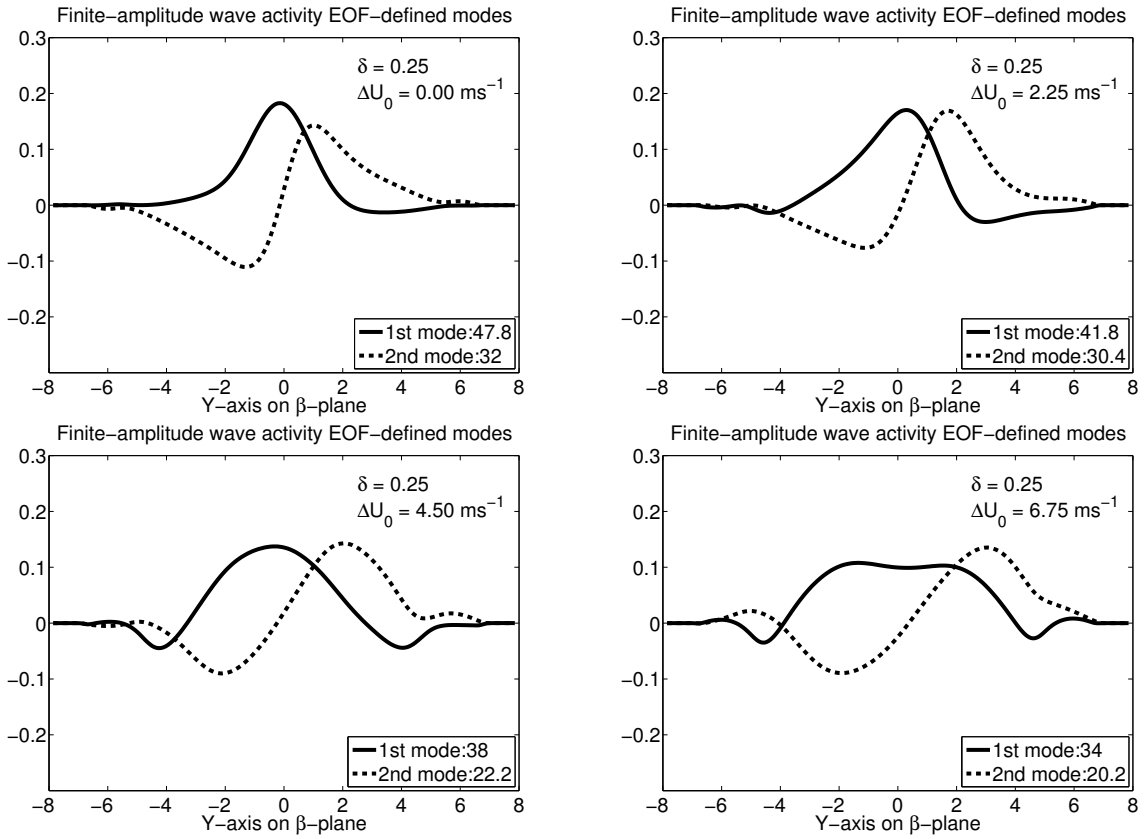

Figure 4.13: Similar to Figure 4.12, but for the leading modes of EOF for the upper layer finite-amplitude wave activity. The solid curves are the first EOF eigenvector, and the dashed curves are the second EOF eigenvector.

CHAPTER 5

A BASELINE THEORY OF PERIODICITY IN STORM TRACK: INTERFERENCE OF QUASI-DISCRETE MODES

So far I have devoted myself to the development of a diagnostic framework and the reproducibility of the observed periodic behavior using the model hierarchy. But what is it that lies at the heart of this oscillation? To explain the 25-day periodicity, I propose the *interference of quasi-discrete modes* as a mechanistic interpretation.

I find that one distinctive property of the Southern Hemisphere extratropics is that the eddy spectra are dominated by a few peaks in the zonal wavenumber-frequency space. In Figure 3.7, 46.5 S was identified as the latitude of maximum eddy amplitude variability during summer. Figure 5.1 shows the power spectra of the 250 hPa geopotential anomaly at 46.5 S as functions of frequency and zonal wavenumber. (See *Salby* [1982] for a related result based on FGGE.) To aid visualization the values are interpolated for non-integer zonal wavenumbers. Overall, the power of geopotential anomaly extends from the low-frequency/low-wavenumber quadrant to the high-frequency/high-wavenumber quadrant, suggestive of eastward (downstream) group propagation [*Lee and Held*, 1993; *Chang and Orlanski*, 1993]. However, this smooth structure of spectra is punctuated by one or more dominant frequency peaks at each zonal wavenumber.

In winter there are three dominant peaks: wavenumbers 1 and 3 at 0.02 CPD and wavenumber 4 at 0.09 CPD (Figure 5.1b). In summer, however, there are multiple peaks for each individual zonal wavenumber from 4 to 6 (Figure 5.1a). This suggests that the geopotential anomalies at 46.5 S consist of a few dominant Fourier modes (hereafter simply 'modes' for brevity). As we will see below, modes with the same zonal wavenumber but distinct frequencies produce amplitude modulation of the zonal-mean eddy heat flux through frequency interference, with a timescale consistent with the BAM. I will also demonstrate that the modal interference is present in the idealized GCM simulations as

well.

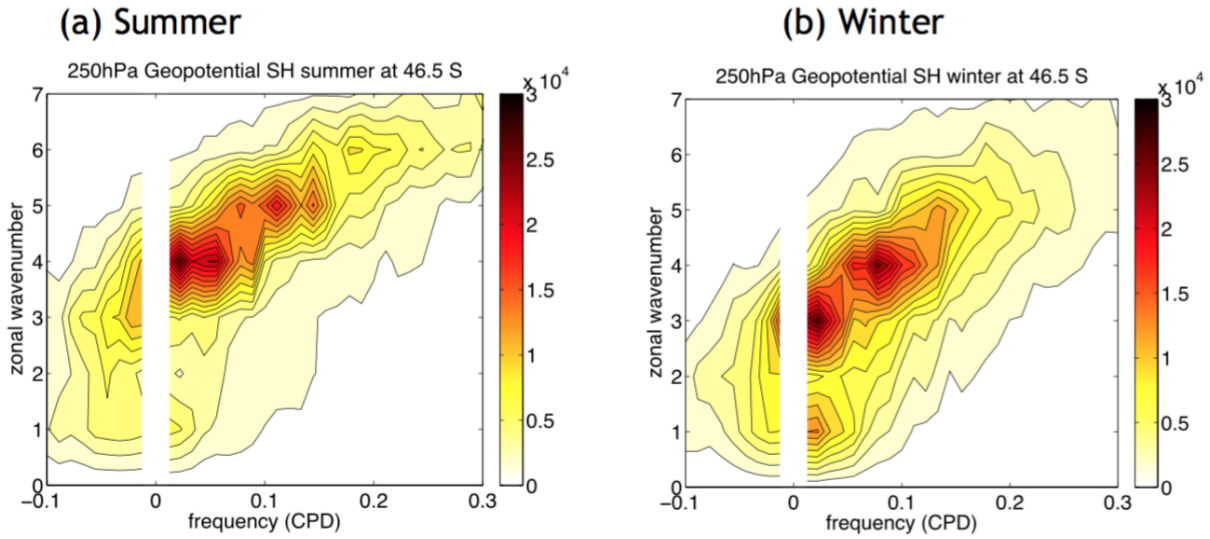

Figure 5.1: Power spectra of the 250 hPa geopotential at 46.5°S as functions of frequency and zonal wavenumber. A positive (negative) frequency means that the eddies are propagating eastward (westward). (a) December-February. (b) June-August. ±0.011 cycle per day (CPD) is the lowest frequency resolved by the data. Based on the ERA-Interim reanalysis 1979-2014. Values are interpolated for non-integer zonal wavenumbers to aid visualization. Contour interval is $1.5 \times 10^3 m^6 s^{-2}$. (appeared in *Wang and Nakamura* [2016])

5.1 Theoretical considerations

Lindzen et al. [1982] suggested that amplitude vacillation of the eddies can arise from interference between coexisting wave modes with the same zonal wavenumber but different phase speeds. *Rivest et al.* [1992] and *Rivest and Farrell* [1992] proposed the notion of 'quasi-modes' in shear flow, a continuous spectrum of eddies whose amplitude distribution is sharply peaked in the phase speed domain and is slowly decaying with time. 'Quasi-modes' with different peak frequencies can sustain interference in a shear flow for finite time. Even simpler example was proposed by *Rotunno and Fantini* [1989], who show that two neutral edge waves in Eady's model [*Eady*, 1949] interfere with each other to generate the overall eddy amplitude modulation.

I demonstrate the idea of mode interference by considering the linearized barotropic vorticity equation on the β plane:

$$\frac{\partial \zeta'}{\partial t} + \overline{u}\frac{\partial \zeta'}{\partial x} + v'\frac{\partial \overline{q}}{\partial y} = 0, \tag{5.1}$$

where ζ' is relative vorticity defined as $\zeta' = \nabla^2\psi'$, the potential vorticity gradient is defined as:

$$\frac{\partial \overline{q}}{\partial y} = \beta - \frac{\partial^2 \overline{u}}{\partial y^2}. \tag{5.2}$$

If the mean flow $\overline{u}$ is constant ($\equiv u_0$), the solution to the above equation is simply the well-known Rossby waves (e.g. harmonic functions in the horizontal directions). By substituting $\psi' = \psi_0 \exp(i(kx + ly - \omega t))$, for a finite-size domain, a finite number of neutral modes propagating westward with respect to the mean flow can be obtained:

$$c = \frac{\omega}{k} = u_0 - \frac{\beta}{k^2 + l^2}. \tag{5.3}$$

Let us assume a superposition of two neutral modes with a same zonal wavenumber but different meridional wavenumbers and frequencies:

$$q' = q_1 \cos(kx - \omega_1 t)\sin(ly) + q_2 \cos(kx - \omega_2 t)\sin(2ly). \tag{5.4}$$

The linear wave activity A_{lin} defined by equation (2.4) is written as:

$$A_{lin} = \frac{\overline{q'^2}}{2\beta} = \frac{1}{\beta}\left[\frac{q_1^2 \sin^2 ly}{4} + \frac{q_2^2 \sin^2 2ly}{4} + \frac{q_1 q_2}{2}\sin(ly)sin(2ly)\cos((\omega_2 - \omega_1)t)\right]. \tag{5.5}$$

The two modes have different zonal *phase speeds* $c_p = \omega/k$. As the 'fast' mode passes by the 'slow' mode, they interfere constructively and destructively in a periodic fashion, creating the amplitude vacillation with a frequency of $\omega_2 - \omega_1$ (the third term on the right hand side of (5.5)).

From the snapshots of q' in Figure 5.2, the linear superposition of the two modes causes oscillation in the meridional tilt of the total eddy PV field. Even though the solution is constructed as superposition of two linear modes, since each mode consists of northward and southward propagating Rossby waves of equal amplitude, the resultant field entails four Rossby waves giving rise to alternating meridional group propagation. The alternating group radiation of Rossby waves indicates that the eddy momentum flux is also changing directions, which, considering equation (2.24), would cause a north-south migration of the zonal-mean zonal wind anomaly. In this example the background zonal flow is assumed to be uniform. When the mean flow contains shear, the interference idea still holds, but the projection of wave activity must include singular continuum modes in addition to the discrete modes [*Held et al.*, 1985].

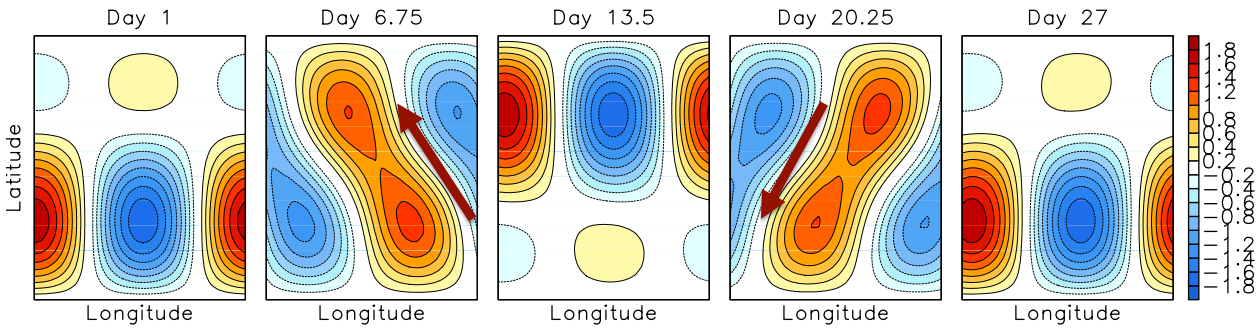

Figure 5.2: Evolution of Eddy PV in a highly truncated linear barotropic QG model that only retains one zonal wavenumber and two meridional wavenumbers. Initial condition(day 1) is superposition of the two modes with unit amplitude, the subsequent figures show the interference of these two modes. The fat arrows indicate the direction of group propagation.

5.2 Idealized vacillation due to mode interference

To provide an anatomy of the periodicity in the meridional eddy heat flux [1], I write the detrended time series of the eddy meridional velocity v' and temperature T' at latitude ϕ and altitude z in terms of the Fourier modes in longitude λ and time t:

$$v'(\lambda,\phi,z,t) = \mathrm{Re}\sum_k\sum_\omega \hat{v}_{k\omega}(\phi,z)e^{i(k\lambda-\omega t)}; \tag{5.6}$$

$$T'(\lambda,\phi,z,t) = \mathrm{Re}\sum_k\sum_\omega \hat{T}_{k\omega}(\phi,z)e^{i(k\lambda-\omega t)}, \tag{5.7}$$

where the zonal wavenumber $k > 0$ and frequency ω are discretized by the periodicity of longitude and the length of data; here we assume that ω is real, that is, modes are all neutral. $\hat{v}_{k\omega}$ and $\hat{T}_{k\omega}$ are the complex Fourier coefficients, and Re denotes the real part. It is readily shown that:

$$\overline{v'T'}(\phi,z,t) = \frac{1}{2}\sum_k\sum_\omega\sum_{\omega'} \mathrm{Re}\left(\hat{v}^*_{k\omega}\hat{T}_{k\omega'}e^{i(\omega-\omega')t}\right), \tag{5.8}$$

where the asterisk denotes complex conjugate. If both v' and T' involve only a single frequency $\omega(k)$ for each k, equation (5.8) becomes:

$$\overline{v'T'} = \frac{1}{2}\sum_k \mathrm{Re}\left(\hat{v}^*_{k\omega(k)}\hat{T}_{k\omega(k)}\right), \tag{5.9}$$

and hence the eddy heat flux does not depend on time. If both v' and T' have two modes for each k with frequencies $\omega_1(k)$ and $\omega_2(k)$,

1. An earlier version of this material in this section appeared in *Wang and Nakamura* [2016]. ©American Meteorological Society. Used with permission.

$$\overline{v'T'} = \frac{1}{2}\sum_k \mathrm{Re}\left(\hat{v}^*_{k\omega_1(k)}\hat{T}_{k\omega_1(k)}\right) + \frac{1}{2}\sum_k \mathrm{Re}\left(\hat{v}^*_{k\omega_2(k)}\hat{T}_{k\omega_2(k)}\right) + \frac{1}{2}\sum_k \mathrm{Re}\left[\left(\hat{v}^*_{k\omega_1(k)}\hat{T}_{k\omega_2(k)} + \hat{v}_{k\omega_2(k)}\hat{T}^*_{k\omega_1(k)}\right)e^{i(\omega_1(k)-\omega_2(k))t}\right]. \tag{5.10}$$

In this case the eddy heat flux consists of steady components associated with individual modes and an oscillatory component arising from their interference, with a frequency $\omega_1(k) - \omega_2(k)$ for each k, represented by the last term in (5.10). Equation (5.10) is analogous to (5.5). As more modes are included, the spectrum of eddy heat flux becomes broader, since the range of $\omega - \omega'$ in (5.8) increases. Note that multiple frequencies are required *for the same wavenumber* to allow amplitude modulation of the zonal-mean eddy heat flux.

Figure 5.3 shows three idealized eddy spectra (for both $|\hat{v}_{k\omega}|$ and $\left|\hat{T}_{k\omega}\right|$) for a fixed k (top) and the corresponding eddy heat flux power spectra (bottom). The eddy spectra have two peaks, each following the standard Gaussian distribution, but with varying widths among the three curves. As long as the peaks are distinct, the corresponding peak in the power spectrum of the eddy heat flux is isolated. As the Gaussian widths increase and the two spectral peaks overlap, a red-noise-like low-frequency variability grows in the heat flux spectrum and eventually merges with the peak. One might suspect that the highly peaked spectrum in the low-level meridional eddy heat flux associated with the BAM in Figure 3.9a (bottom) may arise from a frequency interference of a small number of modes with distinct frequencies.

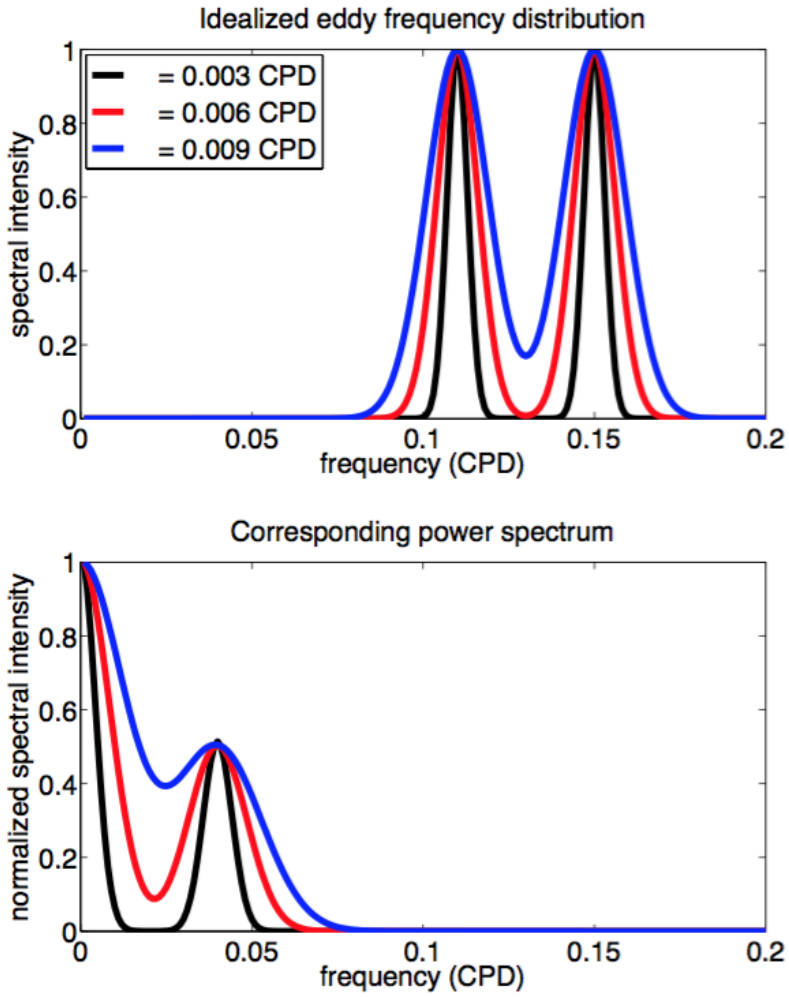

Figure 5.3: Idealized eddy heat flux cospectra (top) and the eddy heat flux power spectra (bottom). See text for details. (appeared in *Wang and Nakamura* [2016]. ©American Meteorological Society. Used with permission.)

5.3 Evidences in observations and idealized GCMs

Figure 5.4 shows the density of eddy heat flux cospectra during the austral summer (December-March) for k = 4, 5, and 6, analyzed from the ECMWF ERA-Interim reanalysis data. The eddy heat flux cospectra is $\mathrm{Re}(\hat{v}^*_{k\omega}\hat{T}_{k\omega})$, which quantifies the time-independent eddy heat flux contributed from each Fourier mode. The top row shows the density of cospectra at 850 hPa as functions of frequency and latitude, and the bottom row shows the same quantity at 46.5°S as functions of frequency and altitude (pressure). The top panels follow the manners of previous spectral analyses [see for example *Randel and Held*, 1991; *Lorenz*, 2014; *Abernathey and Wortham*, 2015]. For a reference, the time-mean, zonal-mean zonal wind is indicated by a blue curve in each panel. In all panels, the eddy heat flux cospectra are markedly banded: for each wavenumber there are a few distinct frequencies at which the poleward (negative) heat flux maximizes, and these maxima span 15-25 degrees in latitude and the entire column of the troposphere. This prompts us to return to the notion of quasi-discrete Fourier modes hinted in Figure 5.1. Figure 5.4 demonstrates that these modes transport heat and indeed make up a large fraction of the time-independent part of the meridional eddy heat flux. Furthermore, since there is more than one dominant mode per zonal wavenumber, amplitude oscillation may arise in the eddy heat flux as a result of their interference. It is worth pointing out that the frequencies of the spectral peaks of the heat flux cospectrum in the observation (top middle panel of Figure 5.4) are the ones used in the idealized spectra in Figure 5.3. Notice that, apart from the modes for k = 6 at low levels, the extent of eddy heat flux cospectra is bounded by the frequency (angular phase speed) of the zonal-mean zonal wind indicated by the blue curves. Thus the modes are trapped inside the critical lines, corroborating the waveguide picture suggested in Section 3.3.3. I have also subdivided the entire data length into several segments and repeated the analysis and confirmed that the results are reproducible for each segment, suggesting that these modes are always present within each season.

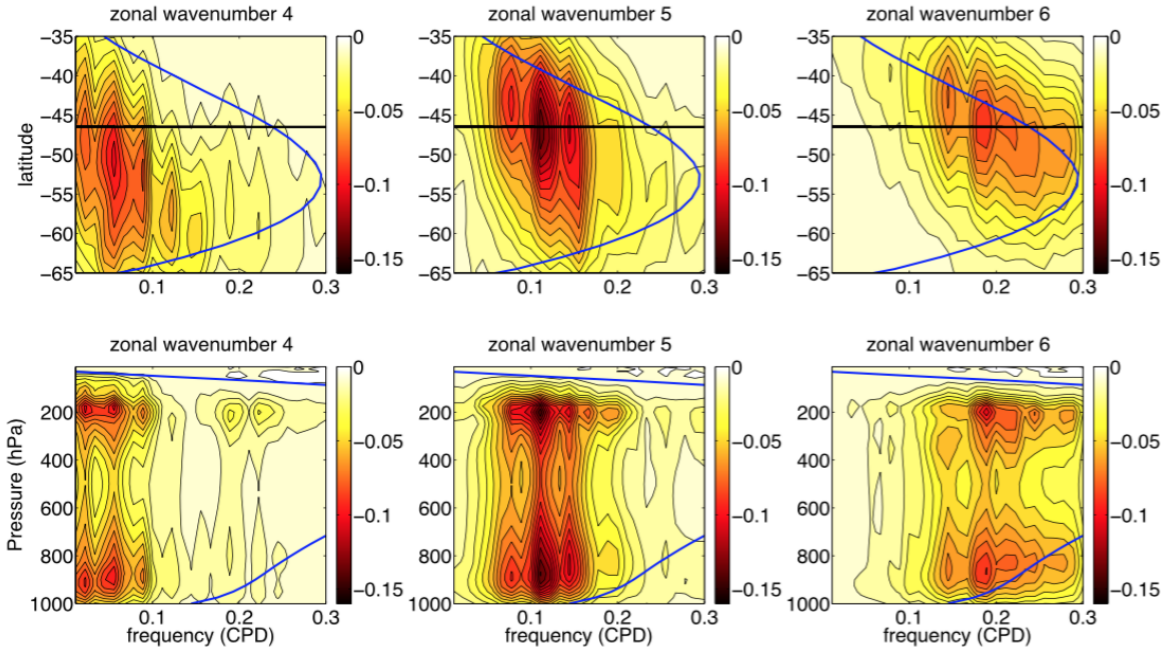

Figure 5.4: Top: eddy heat flux cospectra $\mathrm{Re}(\hat{v}^*_{k\omega}\hat{T}_{k\omega})$ at 850 hPa for December-March as a function of frequency and latitude. Left: zonal wavenumber 4. Center: zonal wavenumber 5. Right: zonal wavenumber 6. Bottom: the corresponding eddy heat flux cospectra at 46.5°S as a function of frequency and pressure. This latitude is indicated by the black line in the top panels. In all panels, the blue curve indicates the time-mean zonal-mean zonal wind in terms of angular frequency. Contour interval: $0.008\,ms^{-1}$. Based on ERA-Interim 1979-2014. (appeared in *Wang and Nakamura* [2016]. ©American Meteorological Society. Used with permission.)

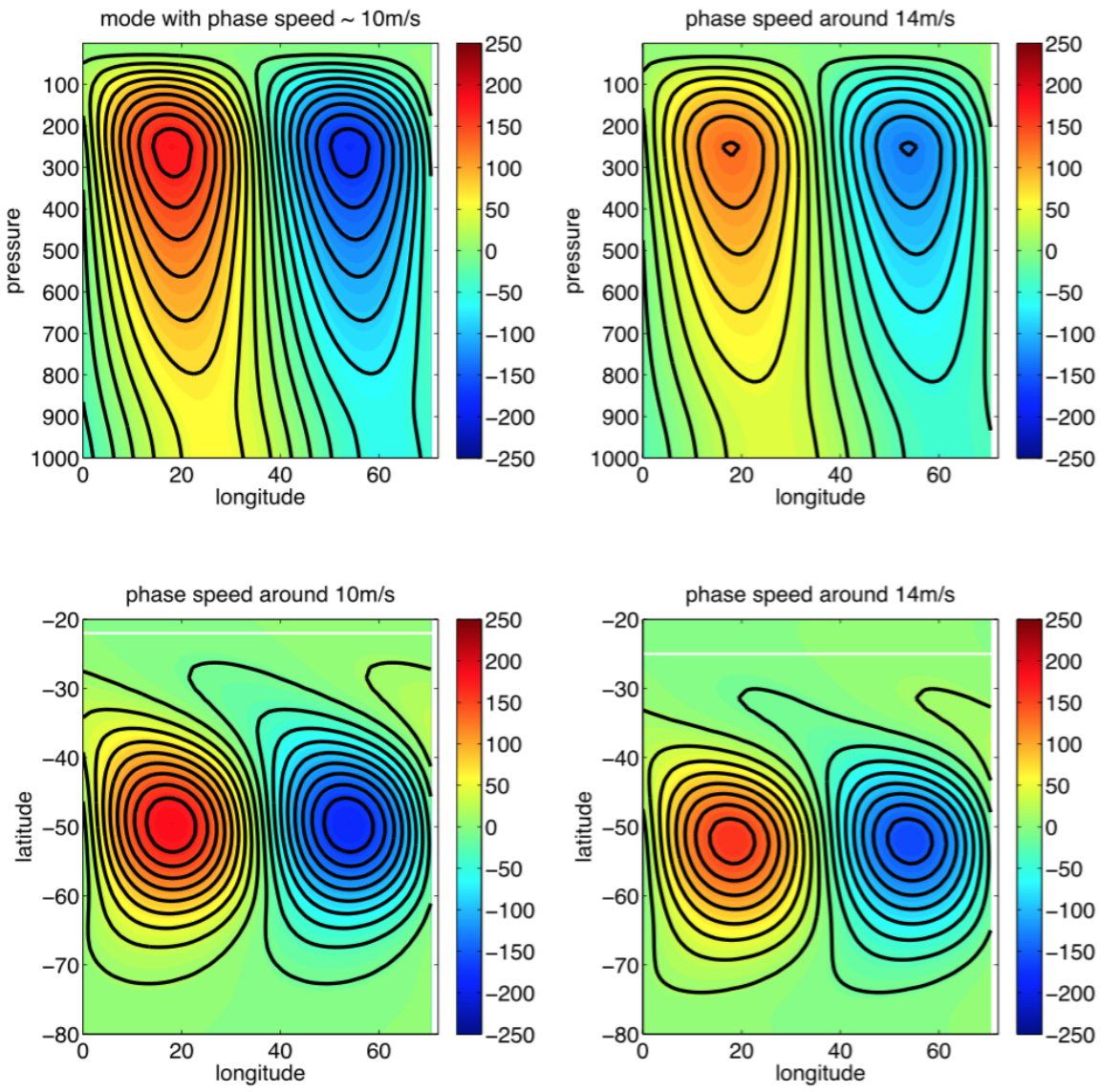

Figure 5.5: Structure of two leading Fourier modes (zonal wavenumber: 5) during the austral summer. Top: geopotential anomaly at 46.5°S as a function of longitude and pressure. Bottom: geopotential anomaly at 250 hPa as a function of longitude and latitude. Left column: zonal phase speed = 10 ms^{-1}. Right column: zonal phase speed = 14 ms^{-1}. Contour intervals: 20 m^2s^{-2}. White lines in the bottom panels indicate critical lines. Based on the ERA-Interim reanalysis (1979-2014). See appendix 5.A for the calculation method for the mode structure. (appeared in *Wang and Nakamura* [2016]. ©American Meteorological Society. Used with permission.)

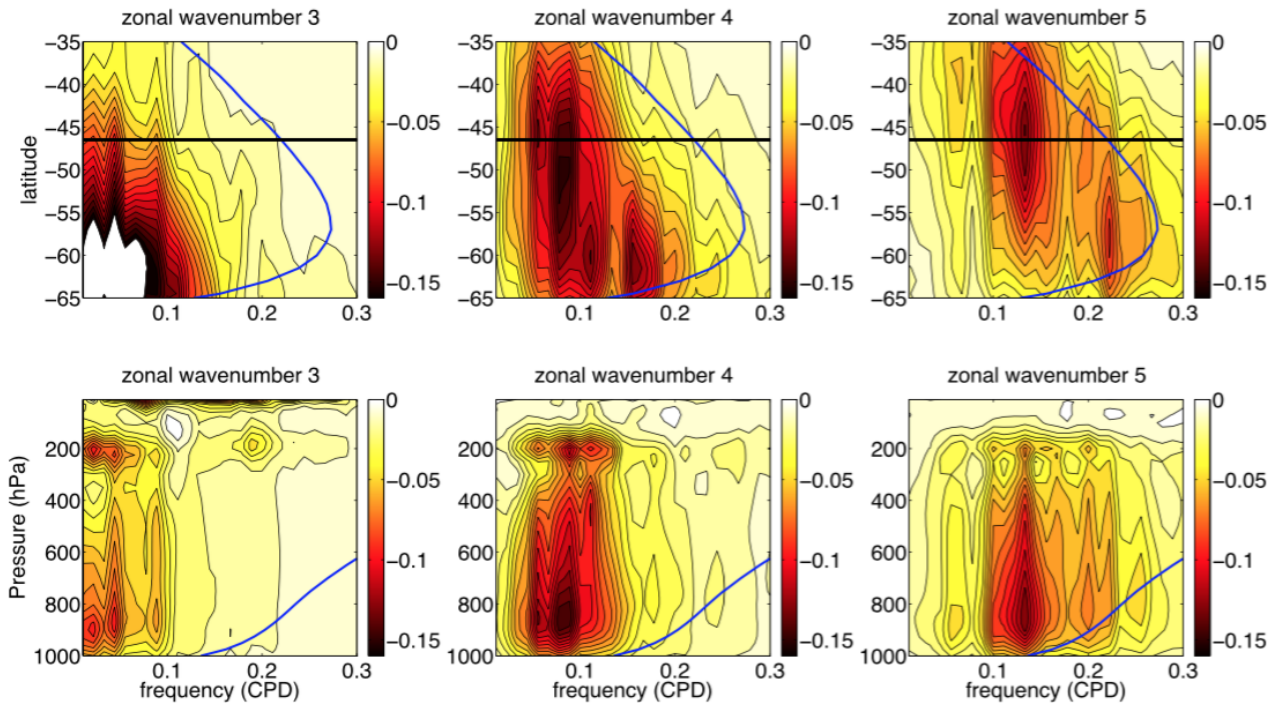

Figure 5.6: Same as Figure 5.4 but for June-September and zonal wavenumbers 3, 4, and 5. (appeared in *Wang and Nakamura* [2016]. ©American Meteorological Society. Used with permission.)

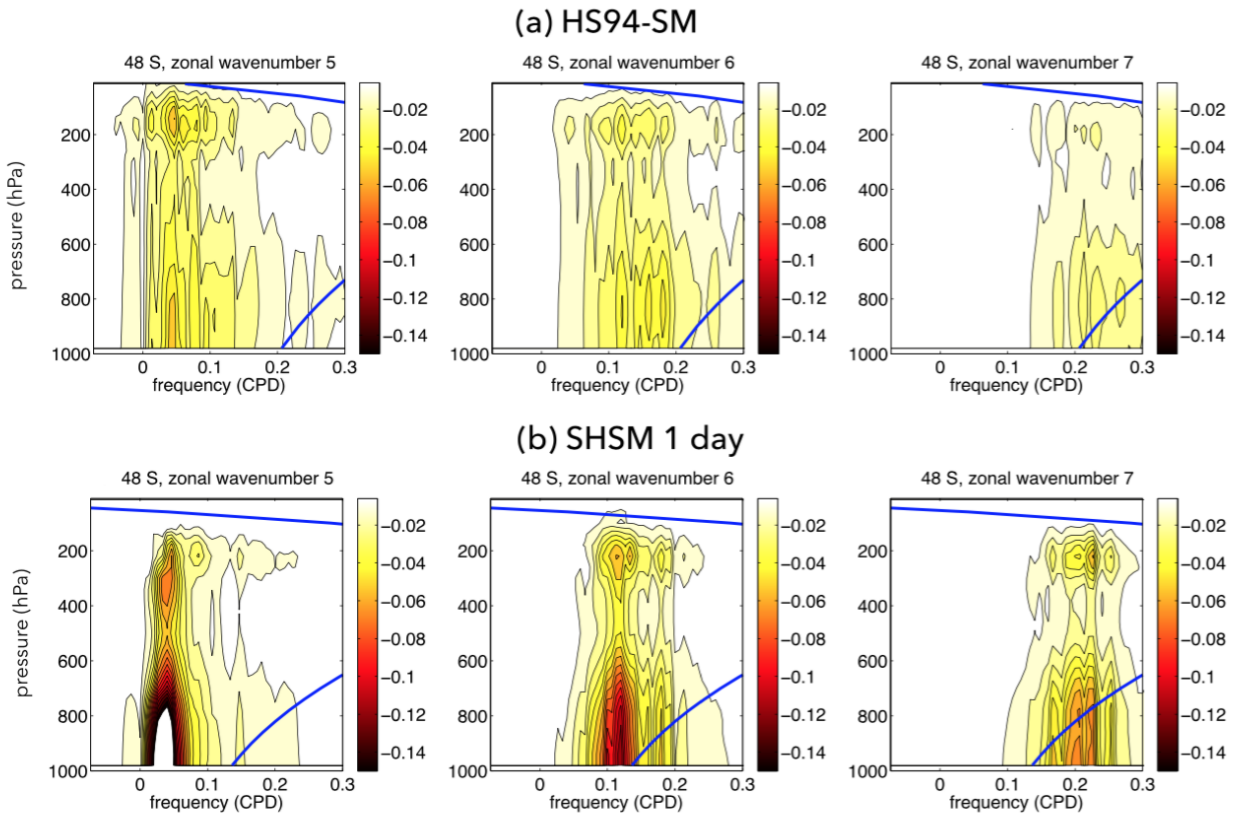

Figure 5.7: Top: eddy heat flux cospectra at 48° S for the HS94-SM experiment as a function of frequency and pressure. Bottom: Same as top except for the SHSM-1day experiment. Panels from left to right: zonal wavenumber 5, 6, and 7. Conventions are the same as the bottom of Figure 5.4. (appeared in *Wang and Nakamura* [2016]. ©American Meteorological Society. Used with permission.)

Figure 5.5 depicts the reconstructed spatial pattern of geopotential anomaly for $k = 5$ at two frequencies (0.11 and 0.15 CPD) that correspond to the observed amplitude maxima in Figure 5.4. They correspond to ~ 10 and $\sim 14\ ms^{-1}$ in terms of the equatorial zonal phase speed (see appendix 5.A for the details of this mode extraction). Figure 5.5a shows the vertical structure at 46.5°S. The two modes have similar vertical structures and amplitudes. They show westward tilts with increasing altitude, similar to a baroclinic wave that sustains poleward heat flux. Figure 5.5b shows the corresponding horizontal structures of the modes at 250 hPa. Both modes exhibit a weak downshear tilt, suggestive of an eddy momentum flux into the jet, but the faster travelling mode has its peak amplitude slightly displaced poleward relative to the slower one. This is consistent with the fact that the critical line (indicated by the white line) of the faster mode is displaced poleward (closer to the jet axis) relative to the slower mode. The poleward shift of the mode structure with increasing frequency is also visible in the top panels of Figure 5.4. As these modes travel at different phase speeds, their repeated constructive and destructive interferences create amplitude vacillation. This causes both the eddy heat flux and the eddy momentum flux to vary, but the effect of the latter on the total eddy forcing is small. The eddy momentum flux arises largely from the meridional tilting of phase lines of eddies, often during the decaying stage of baroclinic lifecycles in which eddies are sheared out by the background shear. This means that it takes superposition of many modes to create eddy momentum flux, since continuous shearing cannot be described by a handful of discrete modes. Thus the eddy momentum flux tends to spread over a broad frequency range, as demonstrated in Figure 3.9 as well as many previous studies [*Lorenz and Hartmann*, 2001; *Thompson and Woodworth*, 2014]. The interference frequency is the difference in the mode frequencies (~0.04 CPD), comparable to the frequency of the BAM. Indeed the frequency separation of the neighboring maxima in Figure 5.4 is quite even and comparable to the BAM frequency for all zonal wavenumbers. This reinforces the strong modulation of the eddy heat flux around the single spectral peak.

Figure 5.6 is similar to Figure 5.4 but for the austral winter (June-September). Here wavenumbers 3-5 are shown, as the eddy spectra shift to longer waves during winter (see Figure 5.1). The largest contribution to the eddy heat flux is from wavenumber 3 at high latitudes and low frequencies. There is a banded structure, but compared to the summer, peaks vary significantly in both magnitude and their spacing. This is consistent with the lack of organized peak in the spectrum of eddy heat flux in the extratropics (Figure 3.9b, bottom).

Using the same format as the bottom of Figure 5.4, I plot in Figure 5.7 the eddy heat flux cospectra of the GCM experiments performed in the previous chapter. The top row shows the eddy heat flux cospectra at 48°S for HS94-SM and the bottom row shows the same quantity at the same latitude for SHSM with a $(1\ \text{day})^{-1}$ surface thermal damping. The HS94-SM experiment, which does not produce a clear single spectral peak in the meridional eddy heat flux, displays numerous weak bands in cospectra. However, they are spread and disorganized; the resultant interference does not produce a single spectral peak. In fact, there are three comparable peaks in the low-frequency range of eddy heat flux spectrum (Figure 5.7a). On the other hand, SHSM-1day, which shows a BAM-like spectral peak in the eddy heat flux (Figure 4.6c) and FAWA (Figure 4.7b), exhibits more compact cospectra. For each wavenumber there is a strong main band that is flanked by a few sidebands, except for $k = 5$ for which sidebands are weak and the spectrum is dominated by a single fat band. Although the precise distribution of cospectra is quite different from observation (Figure 5.4), a main band flanked by a few sidebands appears to be a common pattern, which is presumably efficient at producing a single spectral peak in the eddy heat flux.

Although the Fourier modes are a purely mathematical construct, their resemblance to unstable baroclinic waves [*Charney*, 1947; *Eady*, 1949] in Figure 5.5 prompts us to consider the wave activity budget of each Fourier mode. Since each mode is neutral, gain and loss of wave activity must be exactly and continuously balanced. For small-amplitude

eddies wave activity may be partitioned into contributions from individual modes, since linear modes are mutually orthogonal in the sense of wave activity [*Held et al.*, 1985]. In that case, equation (2.30) applies to each individual mode (without time averaging, since all modes are neutral) provided that damping is also a linear function of wave activity. For modes in Figure 5.5, baroclinic conversion of wave activity (eddy heat flux) is exactly compensated by damping. [At large amplitude the exchange of FAWA between modes becomes significant due to eddy-eddy interactions, so (2.30) applies only to the total field.] Critical lines do not pose mathematical singularity to these modes because of damping: the meridional advection of the planetary PV by the mode is balanced by damping at the critical line.

Given that baroclinic eddies grow and decay constantly in the storm track region [*Lee and Held*, 1993; *Chang and Orlanski*, 1993], it might appear counterintuitive that such an unsteady flow may be expressed as a superposition of neutral modes. The reader is reminded that the Fourier modes are just a way of decomposing finite-length data at a given latitude and height according to the zonal wavenumber and (real) frequency. They are by definition neutral and do not create transient behavior in eddy amplitude or modify the mean flow by themselves. Only the superposition (interference) of multiple modes gives rise to the spatiotemporal variation in eddy amplitude and its interaction with the mean flow. The Fourier modes may or may not be associated with the eigenmodes of the linearized dynamics. I simply point out that decomposing data in terms of discrete Fourier modes provides a convenient interpretation of the BAM through interference if the eddy consists of a small number of discrete modes. To drive the above point home, suppose a leading eigenmode with a zonal wavenumber k and frequency ω is undergoing (nonlinear) amplitude modulation at a given latitude and height:

$$(1+\varepsilon\cos\omega_0 t)\cos(k\lambda-\omega t), \qquad |\omega_0| << |\omega|, \quad 0<\varepsilon<1. \tag{5.11}$$

Since (5.11) can be also written as

$$\cos(k\lambda - \omega t) + 0.5\,\varepsilon\,[\cos(k\lambda - (\omega - \omega_0)t) + \cos(k\lambda - (\omega + \omega_0)t)], \tag{5.12}$$

the Fourier transform of (5.11) will inevitably pick up three discrete frequencies ω and $\omega \pm \omega_0$, whether or not $\cos(k\lambda - (\omega \pm \omega_0)t)$ are eigenmodes.

To be sure, interference of discrete neutral modes has been invoked previously as a theory for structural vacillation of large-scale eddies [*Lindzen et al.*, 1982; *Rotunno and Fantini*, 1989]. However in these studies the discreteness arises naturally from the finite size of the domain and is associated with different structures of eigenmodes (e.g., symmetric and antisymmetric Hough modes in *Lindzen et al.* [1982] and Eady edge waves impinging on the two horizontal boundaries in *Rotunno and Fantini* [1989]). It is not entirely clear how discrete modes in the austral summer arise: the finite width of the baroclinic zone may support a normal mode-like behavior in eddies (particularly the 850 hPa eddy heat flux in the top panels of Figure 5.4 is well contained between the critical lines), but the modes in Figure 5.5 have very similar structures.

It is encouraging that the quasi-discrete Fourier modes can be reproduced at least qualitatively using a dry dynamical core of GCM. If we can explain the emergence of a few quasi-discrete Fourier modes per zonal wavenumber in the austral summer, then the interference idea may provide a succinct understanding of the BAM. Otherwise, a direct attempt at understanding the frequency and amplitude of modulation ω_0, ε without regard to the mode spectra might prove more fruitful. Whether the nonlinear oscillator ideas [*Thompson and Woodworth*, 2014; *Ambaum and Novak*, 2014] eventually succeed at this hinges on whether the dynamical feedback between the meridional eddy heat flux and the low-level baroclinicity is firmly established.

The next subsection explores a possibility that discrete modes arise from non-normal growth of optimal perturbation in the two-layer model.

5.4 Interference of two discrete non-normal modes

In the previous section, amplitude modulation was observed when quasi-discrete modes exist, at least in the statistically steady state. However, the physical mechanism through which such quasi-discrete modes are generated remains a theoretical challenge, although the baroclinic instability theory, as reviewed in Section 2.1.2, explains qualitatively some of the observed eddy properties in the atmosphere. Rapid growth of disturbance is frequently observed in the storm track, much faster than the Eady growth rate based on the normal mode instability theory suggests. Arising from small and random noise, synoptic perturbations can grow very rapidly through non-normal instability, which is often referred to as 'explosive cyclogensis' [*Farrell*, 1988, 1989].

In this section I propose [2] a candidate theory in which quasi-discrete finite-amplitude waves can be fueled through non-normal growth.

I adopt a homogeneous [3] two-layer QG model on a doubly periodic domain and drive it with a stochastic forcing. I use a two-layer QG model on a β-plane with a flat bottom following the formulation in *Flierl* [1978], but as in Section 4.3, I consider the two layers to have a tunable thickness ratio $\delta = 2H_2/(H_1 + H_2)$, where H_1 and H_2 are the layer thicknesses for the upper and lower layers, respectively. The two-layer model is forced by an imposed vertical shear of the background flow $\Delta U_0 = U_1 - U_2$, where U_i is the (constant) background zonal velocity in layer i, with $i = 1$ denoting the upper layer and $i = 2$ denoting the lower layer.

The main difference between this model and the one used in Section 4.3 is that, instead of linearly relaxing the zonal-mean zonal flow toward a baroclinically unstable radiative equilibrium state, I prescribe a constant baroclinicity ΔU_0 (in y) as it is required for the continuity of PV gradient in the meridional. The prescribed steady constant ΔU_0 can

2. This subsection arose from a conversation with Malte Jansen, who encouraged me to think in terms of non-normal modes.

3. The baroclinicity of the model is homogeneous horizontally.

be interpreted as a domain averaged prescribed baroclinicity of the model. It is worth pointing out that for a non-homogeneous two-layer QG (such as that used in Section 4.3), solid 'walls' at the north and south boundaries are usually assumed, instead of doubly periodic domain, so there is no need to make ΔU_0 constant [4].

The governing equations for the PV perturbations are:

$$\begin{aligned} \frac{\partial q_1}{\partial t} + U_1 \frac{\partial q_1}{\partial x} + \frac{\partial \psi_1}{\partial x}\frac{\partial Q_1}{\partial y} + J(\psi_1, q_1) &= ssd + F_1, \\ \frac{\partial q_2}{\partial t} + U_2 \frac{\partial q_2}{\partial x} + \frac{\partial \psi_2}{\partial x}\frac{\partial Q_2}{\partial y} + J(\psi_2, q_2) + \frac{1}{\tau_f}\nabla^2\psi_2 &= ssd + F_2, \end{aligned} \tag{5.13}$$

where Q_i is the background PV and q_i denotes the perturbation PV. The last term on the LHS of the second equation denotes a linear bottom friction, with a decay time scale τ_f. The Jacobian $J(\psi_i, q_i) \equiv \partial\psi_i/\partial x \; \partial q_i/\partial y - \partial\psi_i/\partial y \; \partial q_i/\partial x$ represents nonlinear wave-wave interaction and *ssd* represents small-scale dissipation. F_i denotes the stochastic forcing.

The perturbation streamfunctions ψ_1 and ψ_2 are related to perturbation PV through the inversion relation:

$$\begin{aligned} q_1 &= \nabla^2\psi_1 + F_1(\psi_2 - \psi_1), \\ q_2 &= \nabla^2\psi_2 + F_2(\psi_1 - \psi_2). \end{aligned} \tag{5.14}$$

Similarly, the background PV gradient can be related to the vertical shear and planetary vorticity gradient, β, via:

$$\begin{aligned} \frac{\partial Q_1}{\partial y} &= \beta + F_1\Delta U_0, \\ \frac{\partial Q_2}{\partial y} &= \beta - F_2\Delta U_0, \end{aligned} \tag{5.15}$$

4. Its $\partial q/\partial t$ can be driven by $U(y,t)\partial q/\partial x$ where $U(y,t)$ is instantaneously local mean flow.

where F_1 and F_2 are defined as:

$$F_1 = \frac{1}{2(2-\delta)L_d^2}, \tag{5.16}$$

$$F_2 = \frac{1}{2\delta L_d^2}, \tag{5.17}$$

where L_d is the internal (baroclinic) radius of deformation.

In a homogeneous two-layer QG model, for modal baroclinic instability to occur in the absence of friction, the PV gradient must change sign between the upper layer and lower layer, so as to support counter-propagating Rossby waves (c.f. Section 2.1.2). Given that $\partial Q_1/\partial y$ is always larger than zero for a positive shear ΔU_0, stability is governed by the non-dimensional criticality parameter:

$$\xi = \frac{F_2 \Delta U_0}{\beta}. \tag{5.18}$$

If $\xi > 1$ (equivalent to $\partial Q_2/\partial y < 0$), modal baroclinic instability can occur in the inviscid limit.

In a supercritical state, there is only one pair of unstable and damping modes for given wavenumbers. They share the same phase speed. In a slightly subcritical state, two neutral modes are close to coalescence, but still different in both their structures and phase speeds [5]. Since the phase speeds are not exactly equal, they will not be able to maintain a phase lock. Hence, they will move relative to each other, exhibiting nonmodal oscillation.

Since the flow is vertically sheared the neutral modes are not orthogonal in the sense of energy, and their interference can extract energy from the mean state. Non-normal modes that arise from random stochastic forcing can be very unstable and grow rapidly in a short term ('explosive cyclone') although they will decay away in the long run [*Heifetz*

5. The two neutral normal modes are not orthogonal.

and Methven, 2005; *Farrell and Ioannou*, 2014]. Since the projection of non-normal modes on the discrete normal modes also grows in time, it can excite the discrete modes very effectively. As time goes on, the two discrete modes generate an interference pattern, leading to amplitude vacillation.

To put the homogeneous two-layer QG model in the parameter regime of the Southern Hemisphere storm track, I consider [6]:

- a radius of deformation 700 km
- domain size: $L_x = L_y = 20000$ km, doubly periodic
- a criticality = 0.9 ($U_1 = 0.0$, $U_2 = 7.56\ ms^{-1}$)
- a layer thickness ratio: $\delta = 0.25$

In Figure 5.8, I add a constant harmonic waves with zonal-wavenumber five to the PV fields in both layers through F_1 and F_2. In Figure 5.9, I add a stochastic white noise instead. When the flow is supercritical, these small perturbations will grow exponentially as the linear baroclinic instability theory predicts. However, when the flow is marginally subcritical, these small perturbations undergo periodic undulation with maximum amplitude as large as several orders of magnitude bigger than its initial perturbations. In principle, as $\xi \to 1$ in the inviscid limit, there is no upper bound for how strong a perturbation can grow through the non-normal instability.

When the flow parameters are configured close to the Southern Hemisphere storm track, I found that 20-30 day periodic behavior occurs when the flow is slightly subcritical to baroclinic instability. I show that the domain integrated EKE ($[u'^2 + v'^2]/2$) experiences a periodic behavior on the time scale around 20 to 30 days as demonstrated in the two examples in Figures 5.8 and 5.9. The domain averaged eddy thickness flux (heat flux) also fluctuates with the same periodicity as the EKE. This mechanism in principle can

6. The general results are not sensitive to the exact selection of the parameters.

fuel the modes with discrete phase speeds observed in the austral summer, which leads to the observed amplitude vacillation.

This idealized experiment demonstrates the mechanism by which a finite number of near coalescent discrete neutral modes may be excited. Although in this model the criticality parameter seems to play the key role, the actual manifestation of mode interference also depends on the meridional structure of the background baroclinicity, as we saw in Section 4.3.

In summary, in this chapter I have proposed mode interference as a mechanism to explain the observed amplitude oscillation. As an alternative to the nonlinear oscillator model described in Chapter 1, it is demonstrated that two waves with the same zonal wavenumber but different phase speeds can interfere through constructive and destructive phases, leading to amplitude vacillation. Both observational and modeling evidence support this idea. At this point the precise nature of the quasi-discrete modes found in the reanalysis and GCM results is not known. If they are discrete normal modes of the flow, they have to be neutral and have to have distinct (but not too different) frequencies. A marginally subcritical state is a fostering environment for this, and this may have bearing on the observed seasonality in the periodic behavior of the eddy amplitude in the austral storm track.

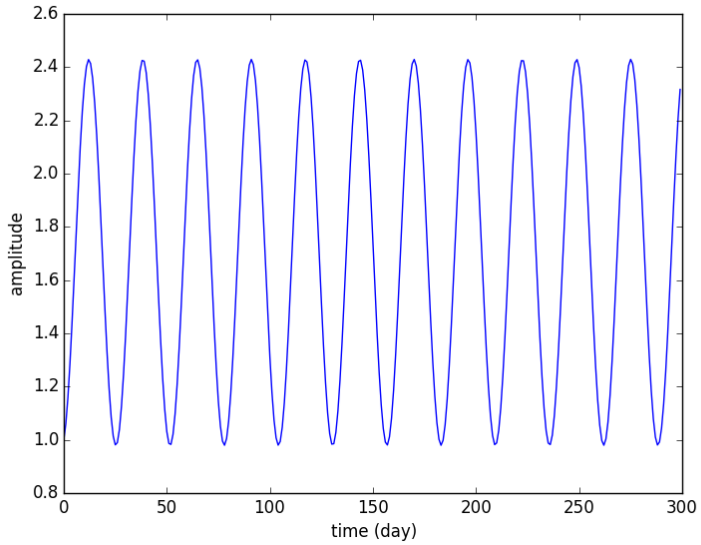

Figure 5.8: Domain-averaged EKE as a function of time. The homogeneous two-layer QG model is marginally subcritical to baroclinic instability, and is forced with zonal wavenumber five perturbation and with no friction.

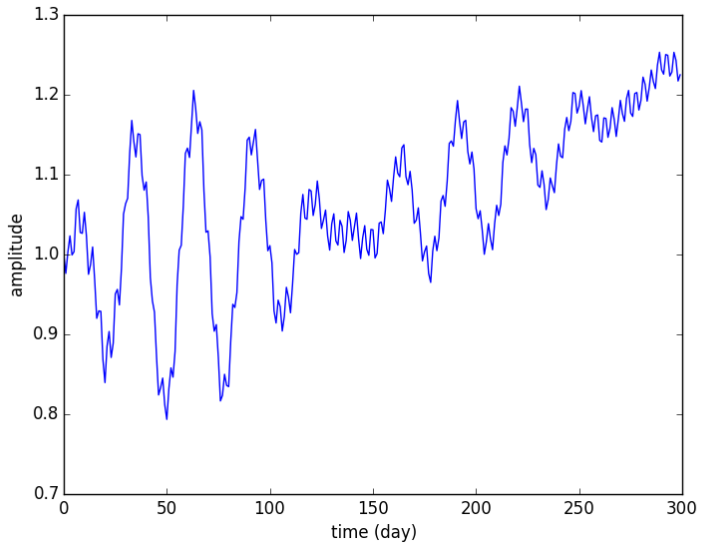

Figure 5.9: Domain-averaged EKE as a function of time. The homogeneous two-layer QG model is marginally subcritical to baroclinic instability, and is forced with stochastic perturbation and damped by linear friction.

Appendix 5.A A composite approach to extract Fourier modes

The Fourier mode structure is extracted as the vertical cross section of geopotential anomaly at 46.5 S and as the horizontal cross section of geopotential anomaly at 250 hPa using the ERA-Interim reanalysis product (1979-2014). For each year, after removing the zonal mean and seasonal mean, I Fourier transform the geopotential anomaly field at each latitude and height into (k, ω)-spectral space. Subsequently, I retain the Fourier modes for $(k, \omega) = (5,\ 0.1111\,\text{CPD})$ and $(5,\ 0.1556\,\text{CPD})$. As shown in Figure 5.4, these two frequencies define the dominant peaks in the zonal wavenumber 5 eddy frequency heat flux cospectra in the Southern Hemisphere summer at 46.5 S. Then, for the two frequencies and for each year, I reconstruct the entire vertical and horizontal mode structures in physical space.

Since the mode structures do not share identical phase information from year to year, they cannot be averaged among multiple years directly. For the horizontal mode structure, I further conduct a composite analysis using 46.5 S as a reference latitude. The zonal phase of the mode for each year is shifted such that the longitudes of the peak amplitude align for all years at the reference latitude. Finally I compute the multiyear composite by averaging. Similarly, I use 250 hPa as a reference pressure level to composite the multiyear vertical mode structure.

CHAPTER 6

SUMMARY AND CONCLUSION

The *baroclinic annular mode* (BAM) defined as the leading EOF of EKE anomaly constitutes a significant component of the low-frequency variability of the extratropical troposphere [*Thompson and Woodworth*, 2014; *Thompson and Barnes*, 2014]. Its 20-30 day periodicity in eddy amplitude and in the associated meridional eddy heat flux is particularly robust and visible even in raw data during the austral summer. This may be exploited to improve the predictability of weather beyond the typical 2-week limit.

To better understand the dynamics of this intra-seasonal variability, spectral analysis was applied to the vertically averaged zonal momentum-FAWA cycle [*Nakamura and Zhu*, 2010; *Wang and Nakamura*, 2015] (summarized in Figure 2.2) for the Southern Hemisphere.

The robust BAM signal in the austral summer (45 percent of the EKE variance explained) is accompanied by concentrated spectral peaks in the vertically averaged FAWA and the low-level meridional eddy heat flux in the frequency-latitude plane (Figures 3.7a and 3.7c), with the latter being the primary driver of the former [equation (2.23) and Figure 3.9a, bottom]. In winter when the BAM accounts for only 30 percent of the variance, the spectra of raw FAWA and eddy heat flux are not well correlated (Figures 3.7d and 3.7f). Still throughout the year a high correlation (r = 0.72) was found between the volume integral of FAWA and the BAM index (Figure 3.8).

On the other hand, little signature of the BAM was found in the spectra of the raw low-level zonal-mean baroclinicity, its tendency or eddy forcing (Figure 1.5). This casts a reasonable doubt on the relevance of the nonlinear oscillator model [*Thompson and Barnes*, 2014; *Ambaum and Novak*, 2014] in which the feedback between the eddy heat flux and baroclinicity plays a key role in generating a periodic behavior. Based on the spectral analysis of the low-level eddy heat flux (Figures 5.1, 5.4), interference of neutral Fourier modes with the same zonal wavenumber but with different frequencies is proposed as

an alternative interpretaion of the BAM. According to this idea, the modification of the mean flow by the eddies is more like a passive response, rather than an essential driver for the oscillation, and to the lowest order the behavior of the eddy can be understood by linear dynamics.

It is then hypothesized that the zonal-mean state has a strong control on the spectral properties of eddies to influence the nature of the BAM: in the austral summer the phase propagation of the modes is predominantly along the zonal waveguide, set up by the upper tropospheric PV gradient, jet stream, and the low-level baroclinicity all concentrated in a narrow latitude band [Figure 3.10; *Lee*, 2014; *Nakamura and Shimpo*, 2004]. The focusing of waves in the direction of longitude would enhance the interference of modes along the latitude circle, making the BAM more visible.

To test this idea, climate model outputs with varying complexity have been examined following the model hierarchy approach [*Held*, 2005; *Shaw et al.*, 2016]. It is found that the basic state is important for generating a periodicity whereas the representation of the oceans is inconsequential. A dry dynamical core of GCM was used with the zonal-mean state nudged toward the observed profile, while allowing eddy to evolve quasi-adiabatically. Keeping the mean state close to the observed profile while maintaining a strong surface thermal damping helped to improve the shape of the eddy flux spectra, although the overall power was too weak. This discrepancy in the power is due in part to the lack of diabatic forcing on eddy and in part to the fact that the zonal-mean forcing diminishes the need for eddy to maintain the observed state. Furthermore, despite the reasonable spectral shape of the eddy heat flux, the precise form of cospectra in the experiment differs significantly from observation. Nevertheless the banded structure in the cospectra appears to be responsible for the BAM-like low frequency periodicity through interference. To search for a minimum model, the model physics was stripped all the way to the two-layer QG model. It was demonstrated that a periodic behavior arises in this model when the baroclinicity of the flow is weak.

As it stands, the origin of the observed discrete Fourier modes remains to be identified, although non-normal growth under a marginally subcritical flow condition offers a testable hypothesis. This will be a subject of future studies. Future work should also address local features of the periodic behavior as they are more directly relevant to the societal and economic interests of the citizens.

REFERENCES

Abernathey, R., and C. Wortham (2015), Phase speed cross spectra of eddy heat fluxes in the pacific., *Journal of Physical Oceanography*.

Ait-Chaalal, F., and T. Schneider (2014), Why eddy momentum fluxes are concentrated in the upper troposphere, *Journal of the Atmospheric Sciences*, *72*(4), 1585–1604, doi: 10.1175/JAS-D-14-0243.1.

Ambaum, M. H. P., and L. Novak (2014), A nonlinear oscillator describing storm track variability, *Quarterly Journal of the Royal Meteorological Society*, *140*(685), 2680–2684, doi:10.1002/qj.2352.

Andrews, D. G., and M. E. McIntyre (1976), Planetary waves in horizontal and vertical shear: The generalized Eliassen-Palm relation and the mean zonal acceleration, *Journal of the Atmospheric Sciences*, *33*(11), 2031–2048, doi:10.1175/1520-0469(1976)033⟨2031:PWIHAV⟩2.0.CO;2.

Atlas, R., R. N. Hoffman, J. Ardizzone, S. M. Leidner, J. C. Jusem, D. K. Smith, and D. Gombos (2010), A cross-calibrated, multiplatform ocean surface wind velocity product for meteorological and oceanographic applications, *Bulletin of the American Meteorological Society*, *92*(2), 157–174, doi:10.1175/2010BAMS2946.1.

Baldwin, M. P., D. B. Stephenson, D. W. J. Thompson, T. J. Dunkerton, A. J. Charlton, and A. O'Neill (2003), Stratospheric memory and skill of Extended-Range weather forecasts, *Science*, *301*(5633), 636–640, doi:10.1126/science.1087143, PMID: 12893941.

Blanco-Fuentes, J., and P. Zurita-Gotor (2011), The driving of baroclinic anomalies at different timescales, *Geophysical Research Letters*, *38*(23), L23,805, doi:10.1029/2011GL049785.

Chang, E. K. M. (2005), The role of wave packets in Wave–Mean flow interactions during southern hemisphere summer, *Journal of the Atmospheric Sciences*, *62*(7), 2467–2483, doi:10.1175/JAS3491.1.

Chang, E. K. M. (2006), An idealized nonlinear model of the northern hemisphere winter storm tracks, *Journal of the Atmospheric Sciences*, *63*(7), 1818–1839, doi:10.1175/JAS3726.1.

Chang, E. K. M., and I. Orlanski (1993), On the dynamics of a storm track, *Journal of the Atmospheric Sciences*, *50*(7), 999–1015, doi:10.1175/1520-0469(1993)050⟨0999:OTDOAS⟩2.0.CO;2.

Charney, J. G. (1947), The dynamics of long waves in a baroclinic westerly current, *Journal of Meteorology*, *4*(5), 136–162, doi:10.1175/1520-0469(1947)004⟨0136:TDOLWI⟩2.0.CO;2.

Charney, J. G. (1948), *On the Scale of Atmospheric Motions*, Geofys. Publ. Oslo, Google-Books-ID: p1qIGQAACAAJ.

Charney, J. G., and P. G. Drazin (1961), Propagation of planetary-scale disturbances from the lower into the upper atmosphere, *Journal of Geophysical Research*, *66*(1), 83–109, doi:10.1029/JZ066i001p00083.

Charney, J. G., and M. E. Stern (1962), On the stability of internal baroclinic jets in a rotating atmosphere, *Journal of the Atmospheric Sciences*, *19*(2), 159–172, doi:10.1175/1520-0469(1962)019⟨0159:OTSOIB⟩2.0.CO;2.

Chen, T., M. Yen, and D. P. Nune (1987), Dynamic aspects of the Southern-Hemisphere Medium-Scale waves during the southern summer season, *Journal of the Meteorological Society of Japan. Ser. II*, *65*(3), 401–421.

Dee, D. P., S. M. Uppala, A. J. Simmons, P. Berrisford, P. Poli, S. Kobayashi, U. Andrae, M. A. Balmaseda, G. Balsamo, P. Bauer, P. Bechtold, A. C. M. Beljaars, L. van de Berg, J. Bidlot, N. Bormann, C. Delsol, R. Dragani, M. Fuentes, A. J. Geer, L. Haimberger, S. B. Healy, H. Hersbach, E. V. Hólm, L. Isaksen, P. Kållberg, M. Köhler, M. Matricardi, A. P. McNally, B. M. Monge-Sanz, J. Morcrette, B. Park, C. Peubey, P. de Rosnay, C. Tavolato, J. Thépaut, and F. Vitart (2011), The ERA-Interim reanalysis: configuration and performance of the data assimilation system, *Quarterly Journal of the Royal Meteorological Society*, *137*(656), 553–597, doi:10.1002/qj.828.

Eady, E. T. (1949), Long waves and cyclone waves, *Tellus*, *1*(3), 33–52, doi:10.1111/j.2153-3490.1949.tb01265.x.

Eliassen, A., and E. Palm (1961), *On the transfer of energy in stationary mountain waves*, I kommisjon hos Aschehoug, Oslo.

Ertel, H. (1942), Ein neuer hydrodynamischer wirbelsatz (a new hydrodynamic eddy theorem), *Meteorological Zeitung*, *59*, 271–281.

Esler, J. G. (2008), The turbulent equilibration of an unstable baroclinic jet, *Journal of Fluid Mechanics*, *599*, 241–268, doi:10.1017/S0022112008000153.

Farrell, B. (1988), Optimal excitation of neutral rossby waves, *Journal of the Atmospheric Sciences*, *45*(2), 163–172, doi:10.1175/1520-0469(1988)045⟨0163:OEONRW⟩2.0.CO;2.

Farrell, B. F. (1989), Optimal excitation of baroclinic waves, *Journal of the Atmospheric Sciences*, *46*(9), 1193–1206, doi:10.1175/1520-0469(1989)046⟨1193:OEOBW⟩2.0.CO;2.

Farrell, B. F., and P. J. Ioannou (2014), Statistical state dynamics: a new perspective on turbulence in shear flow, *arXiv:1412.8290 [physics]*, arXiv: 1412.8290.

Feldstein, S., and S. Lee (1998), Is the atmospheric zonal index driven by an eddy feedback?, *Journal of the Atmospheric Sciences*, *55*(19), 3077–3086, doi:10.1175/1520-0469(1998)055⟨3077:ITAZID⟩2.0.CO;2.

Feldstein, S. B. (2000), Is interannual zonal mean flow variability simply climate noise?, *Journal of Climate*, *13*(13), 2356–2362, doi:10.1175/1520-0442(2000)013⟨2356:IIZMFV⟩2.0.CO;2.

Flierl, G. R. (1978), Models of vertical structure and the calibration of two-layer models, *Dynamics of Atmospheres and Oceans*, *2*(4), 341–381, doi:10.1016/0377-0265(78)90002-7.

Frierson, D. M. W. (2006), Robust increases in midlatitude static stability in simulations of global warming, *Geophysical Research Letters*, *33*(24), L24,816, doi:10.1029/2006GL027504.

Fultz, D., R. R. Long, G. V. Owens, W. Bohan, R. Kaylor, and J. Weil (1959), Studies of thermal convection in a rotating cylinder with some implications for Large-Scale atmospheric motions, in *Studies of Thermal Convection in a Rotating Cylinder with Some Implications for Large-Scale Atmospheric Motions*, no. 4 in Meteorological Monographs, pp. 1–104, American Meteorological Society, DOI: 10.1007/978-1-940033-37-2_1.

Gerber, E. P., and D. W. J. Thompson (2016), What makes an annular mode "annular"?, *Journal of the Atmospheric Sciences*, doi:10.1175/JAS-D-16-0191.1.

Gerber, E. P., and G. K. Vallis (2005), A stochastic model for the spatial structure of annular patterns of variability and the north atlantic oscillation, *Journal of Climate*, *18*(12), 2102–2118, doi:10.1175/JCLI3337.1.

Gerber, E. P., L. M. Polvani, and D. Ancukiewicz (2008), Annular mode time scales in the intergovernmental panel on climate change fourth assessment report models, *Geophysical Research Letters*, *35*(22), L22,707, doi:10.1029/2008GL035712.

Hartmann, D. L. (2000), The key role of Lower-Level meridional shear in baroclinic wave life cycles, *Journal of the Atmospheric Sciences*, *57*(3), 389–401, doi:10.1175/1520-0469(2000)057⟨0389:TKROLL⟩2.0.CO;2.

Hartmann, D. L., and F. Lo (1998), Wave-Driven zonal flow vacillation in the southern hemisphere, *Journal of the Atmospheric Sciences*, *55*(8), 1303–1315, doi:10.1175/1520-0469(1998)055⟨1303:WDZFVI⟩2.0.CO;2.

Heifetz, E., and J. Methven (2005), Relating optimal growth to counterpropagating rossby waves in shear instability, *Physics of Fluids (1994-present)*, *17*(6), 064,107, doi:10.1063/1.1937064.

Held, I. M. (1975), Momentum transport by Quasi-Geostrophic eddies, *Journal of the Atmospheric Sciences*, *32*(7), 1494–1497, doi:10.1175/1520-0469(1975)032⟨1494:MTBQGE⟩2.0.CO;2.

Held, I. M. (2005), The gap between simulation and understanding in climate modeling, *Bulletin of the American Meteorological Society*, *86*(11), 1609–1614, doi:10.1175/BAMS-86-11-1609.

Held, I. M., and T. Schneider (1999), The surface branch of the zonally averaged mass transport circulation in the troposphere, *Journal of the Atmospheric Sciences*, *56*(11), 1688–1697, doi:10.1175/1520-0469(1999)056⟨1688:TSBOTZ⟩2.0.CO;2.

Held, I. M., and M. J. Suarez (1994), A proposal for the intercomparison of the dynamical cores of atmospheric general circulation models, *Bulletin of the American Meteorological Society*, *75*(10), 1825–1830, doi:10.1175/1520-0477(1994)075⟨1825:APFTIO⟩2.0.CO;2.

Held, I. M., R. L. Panetta, and R. T. Pierrehumbert (1985), Stationary external rossby waves in vertical shear, *Journal of the Atmospheric Sciences*, *42*(9), 865–883, doi:10.1175/1520-0469(1985)042⟨0865:SERWIV⟩2.0.CO;2.

Herman, A. (2015), Trends and variability of the atmosphere–ocean turbulent heat flux in the extratropical southern hemisphere, *Scientific Reports*, *5*, 14,900, doi:10.1038/srep14900.

Hide, R. (1953), Some experiments on thermal convection in a rotating liquid, *Quarterly Journal of the Royal Meteorological Society*, *79*(339), 161–161, doi:10.1002/qj.49707933916.

Hoskins, B. J., and K. I. Hodges (2005), A new perspective on southern hemisphere storm tracks, *Journal of Climate*, *18*(20), 4108–4129, doi:10.1175/JCLI3570.1.

Hoskins, B. J., M. E. McIntyre, and A. W. Robertson (1985), On the use and significance of isentropic potential vorticity maps, *Quarterly Journal of the Royal Meteorological Society*, *111*(470), 877–946, doi:10.1002/qj.49711147002.

Huang, C. S. Y., and N. Nakamura (2016), Local Finite-Amplitude wave activity as a diagnostic of anomalous weather events, *Journal of the Atmospheric Sciences*, *73*(1), 211–229, doi:10.1175/JAS-D-15-0194.1.

James, I. N. (1987), Suppression of baroclinic instability in horizontally sheared flows, *Journal of the Atmospheric Sciences*, *44*(24), 3710–3720, doi:10.1175/1520-0469(1987)044⟨3710:SOBIIH⟩2.0.CO;2.

James, I. N., and L. J. Gray (1986), Concerning the effect of surface drag on the circulation of a baroclinic planetary atmosphere, *Quarterly Journal of the Royal Meteorological Society*, *112*(474), 1231–1250, doi:10.1002/qj.49711247417.

Kay, J. E., C. Deser, A. Phillips, A. Mai, C. Hannay, G. Strand, J. M. Arblaster, S. C. Bates, G. Danabasoglu, J. Edwards, M. Holland, P. Kushner, J. Lamarque, D. Lawrence, K. Lindsay, A. Middleton, E. Munoz, R. Neale, K. Oleson, L. Polvani, and M. Vertenstein (2015), The community earth system model (CESM) large ensemble project: A community resource for studying climate change in the presence of internal climate variability, *Bulletin of the American Meteorological Society*, *96*(8), 1333–1349, doi:10.1175/BAMS-D-13-00255.1.

Lachmy, O., and N. Harnik (2014), The transition to a subtropical jet regime and its maintenance, *Journal of the Atmospheric Sciences*, *71*(4), 1389–1409, doi:10.1175/JAS-D-13-0125.1.

Lee, R. W. (2014), *Storm track biases and changes in a warming climate from an extratropical cyclone perspective using CMIP5*, University of Reading.

Lee, S., and S. Feldstein (1996), Mechanism of zonal index evolution in a Two-Layer model, *Journal of the Atmospheric Sciences*, *53*(15), 2232–2246, doi:10.1175/1520-0469(1996)053⟨2232:MOZIEI⟩2.0.CO;2.

Lee, S., and I. M. Held (1991), Subcritical instability and hysteresis in a Two-Layer model, *Journal of the Atmospheric Sciences*, *48*(8), 1071–1077, doi:10.1175/1520-0469(1991)048⟨1071:SIAHIA⟩2.0.CO;2.

Lee, S., and I. M. Held (1993), Baroclinic wave packets in models and observations, *Journal of the Atmospheric Sciences*, *50*(10), 1413–1428, doi:10.1175/1520-0469(1993)050⟨1413:BWPIMA⟩2.0.CO;2.

Lee, S., and H.-k. Kim (2003), The dynamical relationship between subtropical and Eddy-Driven jets, *Journal of the Atmospheric Sciences*, *60*(12), 1490–1503, doi:10.1175/1520-0469(2003)060⟨1490:TDRBSA⟩2.0.CO;2.

Li, Y., and D. W. J. Thompson (2016), Observed signatures of the barotropic and baroclinic annular modes in cloud vertical structure and cloud radiative effects, *Journal of Climate*, *29*(13), 4723–4740, doi:10.1175/JCLI-D-15-0692.1.

Limpasuvan, V., and D. L. Hartmann (2000), Wave-Maintained annular modes of climate variability, *Journal of Climate*, *13*(24), 4414–4429, doi:10.1175/1520-0442(2000)013⟨4414:WMAMOC⟩2.0.CO;2.

Lindzen, R. S., B. Farrell, and D. Jacqmin (1982), Vacillations due to wave interference: Applications to the atmosphere and to annulus experiments, *Journal of the Atmospheric Sciences*, *39*(1), 14–23, doi:10.1175/1520-0469(1982)039⟨0014:VDTWIA⟩2.0.CO;2.

Lorenz, D. J. (2014), Understanding midlatitude jet variability and change using rossby wave chromatography: Poleward-Shifted jets in response to external forcing, *Journal of the Atmospheric Sciences*, *71*(7), 2370–2389, doi:10.1175/JAS-D-13-0200.1.

Lorenz, D. J., and D. L. Hartmann (2001), Eddy-Zonal flow feedback in the southern hemisphere, *Journal of the Atmospheric Sciences*, *58*(21), 3312–3327, doi:10.1175/1520-0469(2001)058⟨3312:EZFFIT⟩2.0.CO;2.

Lorenz, E. N. (1955), Available potential energy and the maintenance of the general circulation, *Tellus*, *7*(2), 157–167, doi:10.1111/j.2153-3490.1955.tb01148.x.

Lorenz, E. N. (1963a), The mechanics of vacillation, *Journal of the Atmospheric Sciences*, *20*(5), 448–465, doi:10.1175/1520-0469(1963)020⟨0448:TMOV⟩2.0.CO;2.

Lorenz, E. N. (1963b), Deterministic nonperiodic flow, *Journal of the Atmospheric Sciences*, *20*(2), 130–141, doi:10.1175/1520-0469(1963)020⟨0130:DNF⟩2.0.CO;2.

Ma, X., P. Chang, R. Saravanan, R. Montuoro, J. Hsieh, D. Wu, X. Lin, L. Wu, and Z. Jing (2015), Distant influence of kuroshio eddies on north pacific weather patterns?, *Scientific Reports*, *5*, doi:10.1038/srep17785, PMID: 26635077 PMCID: PMC4669523.

Marshall, J., and K. Speer (2012), Closure of the meridional overturning circulation through southern ocean upwelling, *Nature Geoscience*, *5*(3), 171–180, doi:10.1038/ngeo1391.

McGraw, M., and E. A. Barnes (2016), Seasonal sensitivity of the Eddy-Driven jet to tropospheric heating in an idealized AGCM, *submitted to Journal of Climate*.

Medeiros, B., D. L. Williamson, and J. G. Olson (2016), Reference aquaplanet climate in the community atmosphere model, version 5, *Journal of Advances in Modeling Earth Systems*, *8*(1), 406–424, doi:10.1002/2015MS000593.

Nakamura, H., and A. Shimpo (2004), Seasonal variations in the southern hemisphere storm tracks and jet streams as revealed in a reanalysis dataset, *Journal of Climate*, *17*(9), 1828–1844, doi:10.1175/1520-0442(2004)017⟨1828:SVITSH⟩2.0.CO;2.

Nakamura, N. (1993), Momentum flux, flow symmetry, and the nonlinear barotropic governor, *Journal of the Atmospheric Sciences*, *50*(14), 2159–2179, doi:10.1175/1520-0469(1993)050⟨2159:MFFSAT⟩2.0.CO;2.

Nakamura, N., and A. Solomon (2010), Finite-Amplitude wave activity and mean flow adjustments in the atmospheric general circulation. part i: Quasigeostrophic theory and analysis, *Journal of the Atmospheric Sciences*, *67*(12), 3967–3983, doi:10.1175/2010JAS3503.1.

Nakamura, N., and A. Solomon (2011), Finite-Amplitude wave activity and mean flow adjustments in the atmospheric general circulation. part II: analysis in the isentropic coordinate, *Journal of the Atmospheric Sciences*, *68*(11), 2783–2799, doi:10.1175/2011JAS3685.1.

Nakamura, N., and L. Wang (2013), On the thickness ratio in the quasigeostrophic Two-Layer model of baroclinic instability, *Journal of the Atmospheric Sciences*, *70*(5), 1505–1511, doi:10.1175/JAS-D-12-0344.1.

Nakamura, N., and D. Zhu (2010), Finite-Amplitude wave activity and diffusive flux of potential vorticity in Eddy-Mean flow interaction, *Journal of the Atmospheric Sciences*, *67*(9), 2701–2716, doi:10.1175/2010JAS3432.1.

Namias, J. (1950), The index cycle and its role in the general circulation, *Journal of Meteorology*, *7*(2), 130–139, doi:10.1175/1520-0469(1950)007⟨0130:TICAIR⟩2.0.CO;2.

Nie, Y., Y. Zhang, G. Chen, X. Yang, and D. A. Burrows (2014), Quantifying barotropic and baroclinic eddy feedbacks in the persistence of the southern annular mode, *Geophysical Research Letters*, *41*(23), 8636–8644, doi:10.1002/2014GL062210.

Oppenheim, A. V., and R. W. Schafer (2009), *Discrete-Time Signal Processing*, 3 edition ed., Pearson, Upper Saddle River.

Pedlosky, J. (1964), The stability of currents in the atmosphere and the ocean: Part i, *Journal of the Atmospheric Sciences*, *21*(2), 201–219, doi:10.1175/1520-0469(1964)021⟨0201:TSOCIT⟩2.0.CO;2.

Pedlosky, J. (1970), Finite-Amplitude baroclinic waves, *Journal of the Atmospheric Sciences*, *27*(1), 15–30, doi:10.1175/1520-0469(1970)027⟨0015:FABW⟩2.0.CO;2.

Pedlosky, J. (1971), Finite-Amplitude baroclinic waves with small dissipation, *Journal of the Atmospheric Sciences*, *28*(4), 587–597, doi:10.1175/1520-0469(1971)028⟨0587:FABWWS⟩2.0.CO;2.

Pedlosky, J. (1979), *Geophysical Fluid Dynamics*, Springer Verlag.

Pedlosky, J. (1982), A simple model for nonlinear critical layers in an unstable baroclinic wave, *Journal of the Atmospheric Sciences*, *39*(10), 2119–2127, doi:10.1175/1520-0469(1982)039⟨2119:ASMFNC⟩2.0.CO;2.

Pfeffer, R. L. (1987), Comparison of conventional and transformed in the troposphere, *Quarterly Journal of the Royal Meteorological Society*, *113*(475), 237–254, doi:10.1002/qj.49711347514.

Phillips, N. A. (1951), A simple Three-Dimensional model for the study of Large-Scale extratropical flow patterns, *Journal of Meteorology*, *8*(6), 381–394, doi:10.1175/1520-0469(1951)008⟨0381:ASTDMF⟩2.0.CO;2.

Phillips, N. A. (1954), Energy transformations and meridional circulations associated with simple baroclinic waves in a two-level, quasi-geostrophic model1, *Tellus*, *6*(3), 273–286, doi:10.1111/j.2153-3490.1954.tb01123.x.

Phillips, N. A. (1956), The general circulation of the atmosphere: A numerical experiment, *Quarterly Journal of the Royal Meteorological Society*, *82*(352), 123–164, doi:10.1002/qj.49708235202.

Pierrehumbert, R. T. (2010), *Principles of Planetary Climate*, Cambridge University Press, Google-Books-ID: bO_U8f5pVR8C.

Plumb, R. A. (1983), A new look at the energy cycle, *Journal of the Atmospheric Sciences*, *40*(7), 1669–1688, doi:10.1175/1520-0469(1983)040⟨1669:ANLATE⟩2.0.CO;2.

Randel, W. J., and I. M. Held (1991), Phase speed spectra of transient eddy fluxes and critical layer absorption, *Journal of the Atmospheric Sciences*, *48*(5), 688–697, doi:10.1175/1520-0469(1991)048⟨0688:PSSOTE⟩2.0.CO;2.

Randel, W. J., and J. L. Stanford (1985), An observational study of Medium-Scale wave dynamics in the southern hemisphere summer. part i: Wave structure and energetics, *Journal of the Atmospheric Sciences*, *42*(11), 1172–1188, doi:10.1175/1520-0469(1985)042⟨1172:AOSOMS⟩2.0.CO;2.

Ravenstein (2010), A journal of the first voyage of vasco da gama, 1497–1499, http://www.cambridge.org/us/academic/subjects/history/south-asian-history/journal-first-voyage-vasco-da-gama-14971499?format=PB&isbn=9781108012966.

Ring, M. J., and R. A. Plumb (2007), Forced annular mode patterns in a simple atmospheric general circulation model, *Journal of the Atmospheric Sciences*, *64*(10), 3611–3626, doi:10.1175/JAS4031.1.

Rivest, C., and B. F. Farrell (1992), Upper-Tropospheric Synoptic-Scale waves. part II: maintenance and excitation of quasi modes, *Journal of the Atmospheric Sciences*, *49*(22), 2120–2138, doi:10.1175/1520-0469(1992)049⟨2120:UTSSWP⟩2.0.CO;2.

Rivest, C., C. A. Davis, and B. F. Farrell (1992), Upper-Tropospheric Synoptic-Scale waves. part i: Maintenance as eady normal modes, *Journal of the Atmospheric Sciences*, *49*(22), 2108–2119, doi:10.1175/1520-0469(1992)049⟨2108:UTSSWP⟩2.0.CO;2.

Robinson, W. A. (2000), A baroclinic mechanism for the eddy feedback on the zonal index, *Journal of the Atmospheric Sciences*, *57*(3), 415–422, doi:10.1175/1520-0469(2000)057⟨0415:ABMFTE⟩2.0.CO;2.

Rossby, C. (1939), Relation between variations in the intensity of zonal circulation of the atmosphere and the displacements of the semi-permanent centers of action, *Journal of Marine Research*, *2*(1), 38–55.

Rossby, C. (1940), Planetary flow patterns in the atmosphere, *Quarterly Journal of the Royal Meteorological Society*, (66 (Suppl.)), 68–87.

Rotunno, R., and M. Fantini (1989), Petterssen's "Type B"Cyclogenesis in terms of discrete, neutral eady modes, *Journal of the Atmospheric Sciences*, *46*(23), 3599–3604, doi:10.1175/1520-0469(1989)046⟨3599:PBITOD⟩2.0.CO;2.

Salby, M. L. (1982), A ubiquitous wavenumber-5 anomaly in the southern hemisphere during FGGE, *Monthly Weather Review*, *110*(11), 1712–1721, doi:10.1175/1520-0493(1982)110⟨1712:AUWAIT⟩2.0.CO;2.

Salmon, R. (1998), *Lectures on Geophysical Fluid Dynamics*, OUP USA, Google-Books-ID: yozmCwAAQBAJ.

Schneider, T., P. A. O'Gorman, and X. Levine (2010), Water vapor and the dynamics of climate changes, *Reviews of Geophysics*, *48*(3), doi:10.1029/2009RG000302, arXiv:0908.4410.

Shaw, T. A., M. Baldwin, E. A. Barnes, R. Caballero, C. I. Garfinkel, Y. Hwang, C. Li, P. A. O'Gorman, G. Rivière, I. R. Simpson, and A. Voigt (2016), Storm track processes and the opposing influences of climate change, *Nature Geoscience*, *9*(9), 656–664, doi:10.1038/ngeo2783.

Simpson, I. R., T. G. Shepherd, P. Hitchcock, and J. F. Scinocca (2013), Southern annular mode dynamics in observations and models. part II: eddy feedbacks, *Journal of Climate*, *26*(14), 5220–5241, doi:10.1175/JCLI-D-12-00495.1.

Small, R. J., J. Bacmeister, D. Bailey, A. Baker, S. Bishop, F. Bryan, J. Caron, J. Dennis, P. Gent, H.-m. Hsu, M. Jochum, D. Lawrence, E. Muñoz, P. diNezio, T. Scheitlin, R. Tomas, J. Tribbia, Y.-h. Tseng, and M. Vertenstein (2014), A new synoptic scale resolving global climate simulation using the community earth system model, *Journal of Advances in Modeling Earth Systems*, *6*(4), 1065–1094, doi:10.1002/2014MS000363.

Swanson, K. L., and R. T. Pierrehumbert (1997), Lower-Tropospheric heat transport in the pacific storm track, *Journal of the Atmospheric Sciences*, *54*(11), 1533–1543, doi:10.1175/1520-0469(1997)054⟨1533:LTHTIT⟩2.0.CO;2.

Taylor, K. E., R. J. Stouffer, and G. A. Meehl (2011), An overview of CMIP5 and the experiment design, *Bulletin of the American Meteorological Society*, *93*(4), 485–498, doi:10.1175/BAMS-D-11-00094.1.

Thompson, D. W. J., and E. A. Barnes (2014), Periodic variability in the Large-Scale southern hemisphere atmospheric circulation, *Science*, *343*(6171), 641–645, doi:10.1126/science.1247660, PMID: 24503850.

Thompson, D. W. J., and Y. Li (2015), Baroclinic and barotropic annular variability in the northern hemisphere, *Journal of the Atmospheric Sciences*, *72*(3), 1117–1136, doi:10.1175/JAS-D-14-0104.1.

Thompson, D. W. J., and J. M. Wallace (2000), Annular modes in the extratropical circulation. part i: Month-to-Month variability, *Journal of Climate*, *13*(5), 1000–1016, doi:10.1175/1520-0442(2000)013⟨1000:AMITEC⟩2.0.CO;2.

Thompson, D. W. J., and J. D. Woodworth (2014), Barotropic and baroclinic annular variability in the southern hemisphere, *Journal of the Atmospheric Sciences*, p. 131108125536009, doi:10.1175/JAS-D-13-0185.1.

Thompson, D. W. J., J. M. Wallace, and G. C. Hegerl (2000), Annular modes in the extratropical circulation. part II: trends, *Journal of Climate*, *13*(5), 1018–1036, doi:10.1175/1520-0442(2000)013⟨1018:AMITEC⟩2.0.CO;2.

Wallace, J. M. (2000), North atlantic oscillatiod annular mode: Two paradigms-one phenomenon, *Quarterly Journal of the Royal Meteorological Society*, *126*(564), 791–805, doi:10.1002/qj.49712656402.

Wang, L., and S. Lee (2016), The role of eddy diffusivity on poleward jet shift, *Journal of the Atmospheric Sciences*, doi:10.1175/JAS-D-16-0082.1.

Wang, L., and N. Nakamura (2015), Covariation of finite-amplitude wave activity and the zonal mean flow in the midlatitude troposphere. part 1: Theory and application to the southern hemisphere summer, *Geophysical Research Letters*, p. 2015GL065830, doi:10.1002/2015GL065830.

Wang, L., and N. Nakamura (2016), Covariation of finite-amplitude wave activity and the zonal mean flow in the mid-latitude troposphere. part 2: eddy forcing spectra and the periodic behavior in the southern hemisphere summer, *Journal of the Atmospheric Sciences*, doi:10.1175/JAS-D-16-0091.1.

Wang, L., M. Jansen, and R. Abernathey (2016), Eddy phase speeds in a two-layer model of quasigeostrophic baroclinic turbulence with applications to ocean observations, *Journal of Physical Oceanography*, doi:10.1175/JPO-D-15-0192.1.

Webster, P. J., and J. L. Keller (1974), Strong long-period tropospheric and stratospheric rhythm in the southern hemisphere, *Nature*, *248*(5445), 212–213, doi:10.1038/248212a0.

Webster, P. J., and J. L. Keller (1975), Atmospheric variations: Vacillations and index cycles, *Journal of the Atmospheric Sciences*, *32*(7), 1283–1301, doi:10.1175/1520-0469(1975)032⟨1283:AVVAIC⟩2.0.CO;2.

Wentz, F. J., L. Ricciardulli, C. Gentemann, T. Meissner, K. Hiburn, and J. Scott (2013), Remote sensing systems coriolis WindSat daily and 3-Day environmental suite on 0.25 deg grid, version 7.0.1, *Remote Sensing Systems, Santa Rosa, CA.*, doi:Availableonlineatwww.remss.com/missions/windsat.[Accessed01082016].

Wentz, F. J., T. Meissner, C. L. Gentemann, and M. Brewer (2014), Remote sensing systems AQUA AMSR-E daily and 3-Day environmental suite on 0.25 deg grid, version 7.0, *Remote Sensing Systems, Santa Rosa, CA.*, doi:Availableonlineatwww.remss.com/missions/amsre.[Accessed01082016].

Yamada, R., and O. Pauluis (2015), Momentum balance and Eliassen–Palm flux on moist isentropic surfaces, *Journal of the Atmospheric Sciences*, *73*(3), 1293–1314, doi:10.1175/JAS-D-15-0229.1.

Zurita-Gotor, P., J. Blanco-Fuentes, and E. P. Gerber (2013), The impact of baroclinic eddy feedback on the persistence of jet variability in the Two-Layer model, *Journal of the Atmospheric Sciences*, *71*(1), 410–429, doi:10.1175/JAS-D-13-0102.1.